



**EVALUATION AND CORRELATION OF
DYNAMIC FLOW, FAILURE, AND
MICROSTRUCTURAL PROPERTIES OF
HEAT-TREATED 4130 STEEL**

DISSERTATION

Luke Atticus Wuertemberger
AFIT-ENY-DS-16-S-068

**DEPARTMENT OF THE AIR FORCE
AIR UNIVERSITY**

AIR FORCE INSTITUTE OF TECHNOLOGY

Wright-Patterson Air Force Base, Ohio

DISTRIBUTION STATEMENT A
APPROVED FOR PUBLIC RELEASE; DISTRIBUTION UNLIMITED.

The views expressed in this document are those of the author and do not reflect the official policy or position of the United States Air Force, the United States Department of Defense or the United States Government. This material is declared a work of the U.S. Government and is not subject to copyright protection in the United States.

AFIT-ENY-DS-16-S-068

EVALUATION AND CORRELATION OF DYNAMIC FLOW, FAILURE, AND
MICROSTRUCTURAL PROPERTIES OF HEAT-TREATED 4130 STEEL

DISSERTATION

Presented to the Faculty
Graduate School of Engineering and Management
Air Force Institute of Technology
Air University
Air Education and Training Command
in Partial Fulfillment of the Requirements for the
Degree of Doctor of Philosophy in Materials Science

Luke Atticus Wuertemberger, B.S., M.S.

15 September 2016

DISTRIBUTION STATEMENT A
APPROVED FOR PUBLIC RELEASE; DISTRIBUTION UNLIMITED.

AFIT-ENY-DS-16-S-068

EVALUATION AND CORRELATION OF DYNAMIC FLOW, FAILURE, AND
MICROSTRUCTURAL PROPERTIES OF HEAT-TREATED 4130 STEEL
DISSERTATION

Luke Atticus Wuertemberger, B.S., M.S.

Committee Membership:

Dr. Anthony N. Palazotto, PhD
Chairman

Dr. Marina Ruggles-Wrenn, PhD
Member

Lt Col Timothy Radsick, PhD
Member

Dr. William P. Baker, PhD
Member

Abstract

For many years, the Air Force Institute of Technology has been attempting to characterize dynamic high speed wear events for Holloman Air Force Base, home to the Holloman High Speed Test Track. The facility carries out rocket sled experiments at flight speeds, where a sled with a payload attached is propelled down a ten-mile track by a train of sleds with rockets providing the acceleration. The sleds are connected to the monorail by heat-treated 4130 steel slippers, which slide along the 1080 steel rail during the runs. These slippers are exposed to extreme conditions during the course of the runs, (heat generation, friction, bouncing) which causes material to be removed as a result of rapid wear. Primarily the focus at AFIT has been building and improving a finite element model to simulate this event. This model uses the Johnson-Cook flow and failure model for stress and damage calculations. These equations require experimentally determined material parameters which have not yet been established for heat-treated 4130 steel. An experimental program has been carried out in conjunction with the University of Dayton Research Institute to do so, and additionally, the microstructure of the failed specimen has been investigated to observe any association of deformation micromechanics to the phenomenological development of the Johnson-Cook expression. An Analysis of Variance (ANOVA) statistical analysis was carried out to identify whether temperature or strain rate were significant factors in causing changes to micromechanical features, and if so, whether the micromechanical properties were related to the Johnson-Cook parameters.

Acknowledgements

First and foremost I would like to thank Dr. Palazotto for his indefatigable encouragement, patience, and guidance through all the years working on this project. Also, many thanks to the Air Force Office of Scientific Research for making this research possible.

This work could not have been possible without the steadfast support and cheerleading of my parents, Lynn and Bev Wuertemberger, my sister Emily for taking my midnight phone calls, and the help, advice, and listening ear of many family, friends, and colleagues. Thanks so much everyone.

Luke Atticus Wuertemberger

Table of Contents

	Page
Abstract	iv
Acknowledgements	v
List of Figures	viii
List of Tables	xvi
List of Abbreviations	xix
List of Symbols	xxi
I. Introduction	1
1.1 Overview	1
1.2 Project History	3
1.3 Goals of the project	10
II. Theory	12
2.1 Stress-Strain Curves	12
Structure and fracture	18
2.2 Dynamic and Thermal Effects	19
2.3 Constitutive Laws and Damage Criteria	21
The Johnson-Cook Constitutive Equation	22
Johnson-Cook Failure Criterion	24
2.4 Current Work	28
2.5 Theory Conclusion	31
III. Experimental Program	32
3.1 Planned Experimental Review	32
Material Treatment and Composition	32
Sample Manufacturing	32
3.2 Tension Test and Split-Hopkinson Bar Overview	36
Low Strain Rate Tension Test Equipment:	
Servo-Hydraulic Test Stand	36
High Strain Rate Tension Test Equipment:	
Split-Hopkinson Bar	38
Split-Hopkinson Bar Stress and Strain	40
3.3 Experimental Results	44
Data Reduction	44
True Stress-Strain Curves	46

	Page
IV. Johnson-Cook Model Fitting	52
4.1 Coefficient Determination	52
Johnson-Cook Strength Coefficient Determination	52
Damage Coefficients	59
4.2 Finite Element Modeling	67
4.3 Discussion	75
4.4 Analytical Numerical Modeling	81
V. Material Analysis	85
Misorientation Angle	86
Grain Size	87
Geometrically Necessary Dislocations	87
Elastic Modulus	88
5.1 Microstructural Sample Preparation and Measurement	90
EBSD Collected Data	98
VI. Statistical Analysis	119
6.1 Statistical Analysis	119
6.2 Discussion	144
VII. Structure-Mesoproperty Correlation	147
7.1 Correlation for the Johnson-Cook Flow Equation	149
7.2 Correlation for the Johnson-Cook Damage Equation	151
VIII. Conclusion	156
8.1 Conclusions	157
8.2 Recommendations	159
IX. Appendix	161
9.1 Appendix A: Materials-based Derivation of Elastic Modulus	161
Derivation of the Materials/physics-based relationship for the Elastic Modulus	161
9.2 Appendix B: UDRI Experiment Engineering Stress-Strain Results	163
9.3 Appendix C: ABAQUS Process	169
9.4 Appendix D: ANOVA Example	175
Bibliography	184

List of Figures

Figure		Page
1	Picture of a June 2014 HHSTT sled featuring treated 4130 steel slippers on a 1080 steel track rail, obtained from correspondence with HAFB	1
2	DADS Data from October 2000 Mission 80X-A1 [15]	5
3	Typical engineering stress-strain curve showing the elastic and plastic regions of deformation	12
4	Examples of plastic behavior for (a) perfectly plastic, (b) strain hardening, (c) rate dependent, and (d) time dependent materials [27]	14
5	Temperature ranges in which the allotropic forms of iron exist in equilibrium conditions. [32]	17
6	Planes of crystal lattices [34]	18
7	Modified Johnson and Cook model [52]	31
8	Diagram of notched triaxiality determination sample, shown with the 0.8mm radius (Dimensions are in English units).	33
9	Sub-size ASTM E8 threaded dogbone specimen diagram (Dimensions are in English units) [55].	34
10	Sub-size ASTM E8 threaded dogbone specimens. Rough machining visible in jitter marks on the threads of the specimen and the turning marks on the gage length. Photo credit to Ron Hoffman.	35
11	MTS Station #5 located at Kettering Labs of UDRI used for quasistatic and reference strain rate tests at room temperature.	37
12	Schematic of Split-Hopkinson Bar experiment. The striker bar impacts the incident bar, sending a stress pulse through the specimen and the transmitter bar. Strain gages record the incident, transmitted, and reflected pulse signals.	38

Figure		Page
13	Split Hopkinson Bar test apparatus located at UDRI used for higher temperature and strain rate experiments	39
14	Induction coil used for heating samples at UDRI	40
15	Averaged experimental data for the 0.01/s (quasistatic) and 0.5/s (reference) strain rates.	47
16	Averaged experimental data for the 500/s strain rates	48
17	Averaged experimental data for the 1000/s strain rates	49
18	Averaged experimental data for the 1800/s strain rates	50
19	0.2% offset fit for treated 4130 using averaged 0.5/s tension data. The calculated Young's Modulus and yield stress are 160,000 MPa and 673 MPa respectively	53
20	Curve fit for Johnson Cook strain rate coefficients B and n of treated 4130 steel. The plastic portion of the quasistatic curve that exhibits strain hardening is isolated and fit linearly. B is 10 raised to the power of the intercept, found here to be 190 MPa, and n is the slope of the line, 0.1538.	54
21	0.5/s average reference stress-strain curve plotted against the solved $\sigma = (A + B\epsilon_p^n)$ curve. The two curves come together between 0.03 and 0.04 of the total strain. The reference strain 0.04 was chosen as it produced the best fitting results.	55
22	Curve fit for the strain rate coefficient Johnson Cook C for treated 4130 steel. The stress at a reference strain (in this study, 0.04) is normalized against the 0.5/s stress and plotted at the natural log of each room temperature strain rate (0.01/s, 0.5/s, 500/s, 1000/s, and 1800/s). The points are linearly fit, and the slope is the value of C, 0.017.....	56

23	Curve fitting for the Johnson Cook thermal coefficient m of treated 4130 steel. The stress at the same reference strain is found for each strain rate (500/s, 1000/s, 1800/s) and at each temperature (223°C, 466°C, 707°C) and normalized against their respective room temperature counterparts. Then the normalized strains are subtracted from one and plotted against the natural log of the homologous temperature and fit linearly for each of the strain rate resulting in three separate linear fits. Each slope is an m value, and in this study the final chosen value of m is 1.07 as it gave the best fit results in simulations.	58
24	Finite element model used to verify the triaxiality using Equation 53. Notch sizes from top to bottom are 0.38mm, 0.79mm, and 2.38mm. For axisymmetric simulations usually cylindrical coordinate system is used, but ABAQUS is converting it to a Cartesian coordinate system.	61
25	Curve fit for the Johnson-Cook damage ductile metal failure void coefficients D_1 , D_2 , and D_3 for treated 4130 steel. The failure strains of the triaxiality specimens are plotted against their calculated triaxiality Equation 53. These points are fit using the Levenberg-Marquardt algorithm, and found to be -0.1895, 0.7324, and 0.6633.....	63
26	The failure strains of treated 4130 steel are found at each room temperature strain rate (0.01/s, 0.5/s, 500/s, 1000/s, 1800/s) and normalized against the triaxiality data at a calibrated reference triaxiality (1.33). These are plotted against the natural log of each of the strain rates and fit linearly. There are three different fits for each of the three triaxialities that are being calibrated. The slope of the line is D_4 , and the calibrated value is 0.0291.	65

Figure		Page
27	The failure strains of treated 4130 steel are found at each strain rate (500/s, 1000/s, 1800/s) for each temperature (23°C, 223°C, 466°C, 707°C) and normalized against the triaxiality data at the chosen reference triaxiality. These are plotted against the correlating homologous temperature and fit linearly. As in the thermal m fitting, each strain rate is plotted separately to allow for calibration. The slope of the line is D_5 , and the calibrated value is 0.7162	66
28	Stress-Strain curve showing ABAQUS's process for applying progressive damage [73]	70
29	ABAQUS output for the vonMises stress, equivalent plastic strain, and damage criterion for a 1000/s, 223°C simulation	71
30	ABAQUS Explicit finite element model of an approximated sub-size E8 dogbone specimen in tension subjected to the same temperatures and strain rates the Split-Hopkinson Bar specimens experienced.	71
31	Dimensioned ABAQUS finite element model - units in mm	72
32	Stress-Strain curve for 500/s impacts at various temperatures. Dashes lines are experimental data, and solid lines are analytically obtained through finite element analysis.	73
33	Stress-Strain curve for 1000/s impacts at various temperatures. Dashes lines are experimental data, and solid lines are analytically obtained through finite element analysis.	74
34	Stress-Strain curve for 1800/s impacts at various temperatures. Dashes lines are experimental data, and solid lines are analytically obtained through finite element analysis.	75
35	Variation of 4130 specific heat capacity C with temperature. Behavior of α and C begins differing right around 1300°F, or roughly 700°C [76]. Where the specific heat capacity suddenly peaks, the thermal diffusivity dramatically dips.	78

Figure		Page
36	The failure strains of treated 4130 steel are found at each strain rate (500/s, 1000/s, 1800/s) for each temperature (23°C, 223°C, 466°C) and normalized against the triaxiality data at the chosen reference triaxiality. These are plotted against the correlating homologous temperature and fit linearly. As in the thermal m fitting, each strain rate is plotted separately to allow for calibration. The slope of the line is D5, and the calibrated value is -0.8503	79
37	Analytical solution for 500/s curves compared against experimental data	82
38	Analytical solution for 1000/s curves compared against experimental data	82
39	Analytical solution for 1000/s curves compared against experimental data	83
40	Sites on sample where measurements were taken for pre-necking and failure regions.	86
41	Final product of sample preparation: Sample has been sectioned, mounted, ground, and polished to a 0.05 μ m surface finish	93
42	Diagram of the geometry of EBSD alignment. Electrons strike a sample angles at 70°, electrons are diffracted in two cones areas in band lines, which are intercepted and recoded on a phosphor screen [80].	95
43	Geometry of Bragg's Law [80].....	96
44	Recorded Kikuchi bands, with intersections indexed [81]	97
45	Visualization of a crystal lattice unit cell as indicated by the indexing of the Kikuchi bands [81]	97
46	Unbroken Grain Map.....	103
47	Grain Size for Sample 29E in the pre-necked region -Temperature: 223°C, Strain rate: 500/s	104
48	Grain Size for Sample 29E in the fracture region -Temperature: 223°C, Strain rate: 500/s	105

Figure		Page
49	Average normalized grain size for all strain rates and temperature conditions in the pre-necked, where each point is the average of two difference EBSD scans	106
50	Average normalized grain size for all strain rates and temperature conditions in the fracture region, where each point is the average of four difference EBSD scans	107
51	Untested Sample Boundary Angles - red lines indicate angles between 2-5°, green lines indicate angles between 5-15°, blue lines represent angles >15°	108
52	29E Boundary Density map of the pre-necked region	109
53	29F Boundary Density map of the fracture region	109
54	Inverse Pole Function Plot Legend	110
55	Unbroken Specimen Inverse Pole Function Plot	111
56	Sample 29E Inverse Pole Function Plot of the pre-necked region	112
57	Sample 29F Inverse Pole Function Plot of the fracture region	112
58	Average normalized misorientation in the pre-necked zone for all strain rates and temperature conditions, where each point is the average of four difference EBSD scans.....	113
59	Average normalized misorientation in the fracture zone for all strain rates and temperature conditions, where each point is the average of four difference EBSD scans	114
60	Average normalized dislocation density in the pre-necked zone for all strain rates and temperature conditions, where each point is the average of two difference EBSD scans.....	115
61	Average normalized dislocation density in the fracture zone for all strain rates and temperature conditions, where each point is the average of four difference EBSD scans.....	116

Figure		Page
62	Average normalized stiffness in the pre-necked zone for all strain rates and temperature conditions, where each point is the average of four difference EBSD scans	117
63	Average normalized stiffness in the fracture zone for all strain rates and temperature conditions, where each point is the average of four difference EBSD scans	117
64	Johnson Transformation of the misorientation angle in the pre-necked region	123
65	Johnson Transformation of the dislocation density in the pre-necked region	124
66	Johnson Transformation of the dislocation density in the failed region	126
67	Johnson Transformation of the grain size in the failed region	127
68	Main Effects plot for the grain size of the fracture region	136
69	Main Effects plot for the grain size of the fracture region	136
70	Main Effects plot for the misorientation of the pre-necked region	137
71	Main Effects plot for the misorientation of the pre-necked region	138
72	Interaction plot for the misorientation of the fracture region	139
73	Main Effects plot for the dislocation density of the pre-necked region	140
74	Main Effects plot for the dislocation density of the pre-necking region	140
75	Main Effects plot for the dislocation density of the fracture region	141
76	Interaction Effects plot for the dislocation density of the fracture region	142

Figure		Page
77	Engineering stress-strain curves for room temperature high strain rate runs	165
78	Engineering stress-strain curves for 1/6 melt temperature (223°C) high strain rate runs	166
79	Engineering stress-strain curves for 1/3 melt temperature (466°C) temperature high strain rate runs	167
80	Engineering stress-strain curves for 1/2 melt temperature (707°C) temperature high strain rate runs	168
81	Average normalized stiffness in the elastic zone for all strain rates and temperature conditions, where each point is the average of four difference EBSD scans	170

List of Tables

Table	Page
1	Scales of material modeling [28] [29] 15
2	Percent composition of alloying elements of 4130 steel [54]. 33
3	Test Program carried out at the University of Dayton Research Institute including the target strain rates and temperatures, and the number of specimens tested for each strain rate - temperature combination 34
4	Comparison of notch triaxialities predicted by finite element modeling and calculated using equation 16 61
5	Mechanical, elastic, and thermal material properties of 4130 steel used for ABAQUS finite element simulation 68
6	Summary of Johnson-Cook Strength and Damage Coefficients calculated for treated 4130 steel. 68
7	Comparison of Johnson-Cook strength and damage coefficients for various metals. 76
8	Failure Strains of 4130 steel as measured experimentally and as predicted using the Johnson-Cook failure equation, with calculated percent differences. 77
9	Failure Strains of 4130 steel as measured experimentally and as predicted using the Johnson-Cook failure equation refit with D5 equal to -0.8503, with calculated percent errors..... 80
10	Grinding and polishing sequence used to prepare heat-treated 4130 samples for EBSD analysis 92
11	EBSD Measurements of the pre-necked zones of dynamically-impacted heat treated 4130 steel 99
11	EBSD Measurements of the pre-necked zones of dynamically-impacted heat treated 4130 steel 100
12	EBSD Measurements of the fracture zones of dynamically-impacted heat treated 4130 steel 100

Table		Page
12	EBSD Measurements of the fracture zones of dynamically-impacted heat treated 4130 steel	101
12	EBSD Measurements of the fracture zones of dynamically-impacted heat treated 4130 steel	102
13	EBSD Measurements of the pre-necked zones of dynamically-impacted heat treated 4130 steel	124
13	EBSD Measurements of the pre-necked zones of dynamically-impacted heat treated 4130 steel	125
14	EBSD Measurements of the pre-necked zones of dynamically-impacted heat treated 4130 steel	127
14	EBSD Measurements of the pre-necked zones of dynamically-impacted heat treated 4130 steel	128
14	EBSD Measurements of the pre-necked zones of dynamically-impacted heat treated 4130 steel	129
14	EBSD Measurements of the pre-necked zones of dynamically-impacted heat treated 4130 steel	130
15	ANOVA calculations for a two-way, fixed effects model. An example calculation is shown in Appendix 9.2	132
16	Grain Size ANOVA for the pre-necked region of dynamically-impacted 4130 steel	135
17	Grain Size ANOVA for the fracture region of dynamically-impacted 4130 steel	135
18	Misorientation ANOVA for the pre-necked region of dynamically-impacted 4130 steel	137
19	Misorientation ANOVA for the fracture region of dynamically-impacted 4130 steel	138
20	Dislocation Density ANOVA for the pre-necked region of dynamically-impacted 4130 steel	139
21	Dislocation Density ANOVA for the fracture region of dynamically-impacted 4130 steel	141

Table		Page
22	Stiffness (elastic modulus) ANOVA for the pre-necked region of dynamically-impacted 4130 steel	142
23	Stiffness (elastic modulus) ANOVA for the fracture region of dynamically-impacted 4130 steel	143
24	Summary: Elastic Section ANOVA Results	143
25	Summary: Fracture Section ANOVA Results	144
26	Measure of association for the pre-necked region	150
27	Measure of association for the failure region	152
28	Example Grain Size Data for ANOVA 2-Way Fixed Effects Model	176
29	Grain size data column and row summations	176
30	Calculated Results for Example Problem	181
31	Minitab Results for Example Problem	182
32	Minitab Results for Example Problem	182

List of Abbreviations

Abbreviation	Page
HAFB	Holloman Air Force Base 1
HHSTT	Holloman High Speed Test Track 1
AFIT	Air Force Institute of Technology 2
CTH	Finite volume simulation hydrocode developed by Sandia National Laboratories 3
ABAQUS	Finite element analysis modeling program developed by Dassault Systmes 4
DADS	Dynamic Analysis and Design System 5
UDRI	University of Dayton Research Institute 11
MATLAB	Computational mathematics program 11
ANOVA	Analysis of Variance 11
BCC	Body-centered cubic atomic structure 17
FCC	Face-centered cubic atomic structure 17
ABAQUS	Commercial finite element program 26
ASTM	American Society for Testing and Materials 33
MTS	Mechanical Test Stand, also the company that makes the stands 36
SHB	Split-Hopkinson Bar 38
IISI	International Institute of Steel and Iron 51
EBSD	Electron Backscatter Diffraction 85
OIM	Orientation imaging software 85
EDAX	Company that makes OIM software 85
LAGB	Low Angle Grain Boundaries 86
HAGB	High Angle Grain Boundaries 86

Abbreviation		Page
MCF	Materials Characterization Facility	90
AFRL	Air Force Research Laboratory	90
SEM	Scanning Electron Microscope	90
EDS	Energy Dispersion Spectroscopy	90
EBSD	Electron Backscatter Diffraction	90

List of Symbols

Symbol		Page
σ_e	Elastic stress	13
E	Elastic modulus	13
ϵ_e	Elastic strain	13
n	Atomic attraction energy constant	15
α	Atomic attraction energy constant	15
m	Atomic repulsion energy constant	15
a	Crystal lattice structure closest packing parameter	15
$\dot{\gamma}$	Shear strain rate	19
ρ	Dislocation density	19
v	Dislocation velocity	19
M	Material crystal orientation factor	20
f_v	Applied force for a Newtonian viscous fluid	21
B	Viscous damping coefficient	21
$\hat{\sigma}_y$	vonMises/equivalent flow stress	23
A	Johnson and Cook constitutive equation yield strength parameter	23
B	Johnson and Cook constitutive equation plastic strain parameter	23
n	Johnson and Cook constitutive equation strain hardening parameter	23
C	Johnson and Cook constitutive equation plastic strain parameter	23
$\dot{\epsilon}_0$	Normalizing strain rate	23
m	Johnson and Cook constitutive equation thermal parameter	23

Symbol		Page
T	Temperature	23
T_{ref}	Reference temperature	23
T_{melt}	Melting temperature of 4130 steel	23
σ_{flow}	Post-yield stress	23
σ_{yield}	Yield stress	23
D	Johnson Cook Damage criterion	25
$\Delta\epsilon^p$	Increment of accumulating equivalent plastic strain	25
ϵ_f	Equivalent strain to fracture at the current strain, strain rate, and temperature conditions	25
D_1	Johnson and Cook damage parameter for void formation	25
D_2	Johnson and Cook damage parameter for void formation	25
D_3	Johnson and Cook damage parameter for void formation	25
D_4	Johnson and Cook damage parameter for strain rate effects	25
D_5	Johnson and Cook damage parameter for thermal effects	25
Q	Triaxiality factor	25
σ_m	Mean or hydrostatic stress	25
$\bar{\sigma}_{eq}$	von Mises equivalent stress	25
σ_{11}	Principal stress tensor in the 11 direction	26
σ_{22}	Principal stress tensor in the 22 direction	26
σ_{33}	Principal stress tensor in the 33 direction	26
σ_{ij}	Stress tensor	26

Symbol		Page
$\bar{\epsilon}_n$	Void nucleation strain	27
α	Material dependent hole growth rate	27
σ_y	Yield strength	29
σ_0	Material constant for starting dislocation motion	29
k_y	Material strengthening coefficient	30
d	average grain diameter	30
$\hat{\epsilon}_p$	Orowan's flow strain	30
α	Orowan material constant	30
b	Burger's vector for dislocation movement	30
ρ_m	Dislocation density	30
\bar{v}	Dislocation velocity vector	30
ϵ_s	SHB sample strain	40
C_o	Elastic wave speed	40
L	Gage length of a sample	40
ϵ_R	Reflected strain wave	40
σ_s	Stress in SHB sample	40
A_H	Cross-sectional area of the Hopkinson bars	40
A_s	Cross-sectional area of the gage section of the sample	41
σ_t	True stress	53
a_0	Radius of the initial cross-sectional area of the notched triaxiality test specimen	59
R_0	Radius of the triaxiality test specimen notch	59
ρ	Density	68
ν	Poisson's ratio	68

Symbol		Page
E	Elastic modulus	68
c_p	Specific heat	68
β	Inelastic heat fraction	68
$d\epsilon$	Change in strain	69
dt	Time step	69
L	Current length of the gage section	69
L_0	Original gage length	69
α_{ij}	Nye's dislocation tensor	88
ε^e	Elastic strain tensor	88
g	Lattice orientation matrix	88
ρ	Nye's dislocation density	88
k	Type of dislocation	88
b	Burger's Vector	88
z	Line direction	88
S_{ijkl}	Elastic compliance constraints from Hooke's Law	89
C_{ijkl}	Stiffness tensor	89
X	Single crystal tensor	89
C_{ijkl}^V	Stiffness tensor approximated using the Voight averaging scheme	89
S_{ijkl}^R	Elastic compliance constraints matrix approximated using the Reuss averaging scheme	89
n	Bragg Law order of constructive interference equal to a whole number	96
λ	wavelength of electrons	96
d	lattice spacing between atom layers	96

Symbol	Page
θ	Bragg Law angle of incidence of the electrons 96
Y_{ijk}	Expected value 130
μ	Average 130
A_i	Fixed treatment effect (temperature) 130
B_j	Fixed treatment effect (Strain Rate) 130
AB_{ij}	Interaction treatment effect 130
ϵ_{ijk}	Random error 130
i	index value for the levels of the temperature treatment 130
a	total number of temperature treatment levels 130
j	Index value for the levels of the strain rate treatment 130
b	total number of levels of strain rate treatment 130
n	The total number of measurement replicates 131
k	Index for the total number of measurement replicates 131
ω^2	Measure of Association for an ANOVA fixed-effects model 149
SS_{effect}	Sum of squares for the treatment effect of interest 149
df_{effect}	Degrees of freedom for the treatment effect of interest 149
MS_{error}	Mean sum of the error term for the ANOVA analysis of interest 149
SS_{Total}	Total sum of squares for the ANOVA analysis of interest 149
σ^*	ABAQUS notation for triaxiality 174

EVALUATION AND CORRELATION OF DYNAMIC FLOW, FAILURE, AND MICROSTRUCTURAL PROPERTIES OF HEAT-TREATED 4130 STEEL

I. Introduction

1.1 Overview

Holloman Air Force Base (HAFB) is home to the 10-mile long Holloman High Speed Test Track (HHSTT) rocket sled testing grounds. During test runs, rocket stages attached to the back of the main sled propel it forward at tremendous speeds.



Figure 1. Picture of a June 2014 HHSTT sled featuring treated 4130 steel slippers on a 1080 steel track rail, obtained from correspondence with HAFB

The slipper, the component that connects the rocket sled to the test track rails, is subjected to extreme conditions during test runs. High strain rates from the rocket

propulsion, high temperatures, micro impact events, friction, and bouncing caused by aerodynamic effects all contribute to the wear of the slipper contact surface via melt and mechanical wear. After test runs, the slippers are discarded. It is of interest to accurately model how much of the slipper material is lost during test runs and potentially extend the life of the component.

Over the years, the Air Force Institute of Technology (AFIT) has spearheaded modeling the wear of the slipper utilizing information gained from metallurgical examination and using various finite element and hydrocode modeling programs [1] [2] [3] [4]. Much progress has been made in developing a robust finite element model that accounts for temperature, strain rate, contact surface bounce, friction, and micro impacts. The model uses the Johnson-Cook constitutive and damage equations to characterize flow stress and failure. These equations are empirically-based and driven by experimentally-determined material parameters. AFIT is now attempting to model the wear of a HHSTT test run where the slipper material is a heat treated 4130 steel, which has not yet been characterized for the constitutive and damage model. Thus, new characterization is required to obtain the material constants.

Beyond being able to model the flow stress of the material, doing experimental work allows an opportunity to systematically observe the effects of temperature and strain rate on the microstructure of heat treated 4130 steel. High strain rate deformation is a process that is not well understood, and more observation is needed to strengthen our knowledge of the physics involved and potentially make improvements to modeling efforts.

In the next section, the history of the modeling work on this project will be briefly reviewed. Following this, the specific goals of this research work will be defined.

1.2 Project History

Wear research for the HHSTT started initially with Gerstle in 1968, David Laird picked up the project for AFIT in 2002 [5][6]. The HHSTT was having issues acquiring its goal velocity of 10,000 ft/s (3048 m/s) due to a gouging problem that was plaguing the rails.

At speeds greater than 4921.26 ft/s (1500 m/s), large divots would sporadically occur, problematic not only due to the damage, but also because it dramatically slowed the sled. Without addressing the problem, the maximum speed of the facility was limited. Laird looked into previous gouging research and began raising points of interest for investigation, including material temperature, shock affects, and frictional heating, and built a foundational understanding of the physics of gouging for AFIT researches to use in their research.

In 2004, Szmerekovsky looked into the problem of bouncing due to a gap between the slipper and the rail and thought that an asperity impact might be a factor in gouge initiation [7]. It was thought that changing materials might mitigate the problem; however, completely replacing ten miles of track was deemed uneconomical. In lieu of this, the idea was raised that the material properties could be slightly adjusted by applying coatings on the rails. This brought about additional questions about the nature of the problem and questioned whether the process could be reasonably considered adiabatic, if deformation was non-linear, and whether the pressures seen during experimentation approached shock levels. Aerodynamic heating became a factor, and a hydrocode developed by Sandia CTH was introduced to the project for modeling purposes using a model developed by Barker [8][7].

Development of this model continued with Kennan's thesis work in 2005 and Cinnamons dissertation work in 2006 [3][9][10]. To support the model, Kennan and Cinnamon considered the materials present in the hypersonic track experiments: Vas-

comax300 slippers and 1080 steel rails. They carried out quasistatic tension, Split-Hopkinson bar, and flyer plate testing to determine specific material parameters for the Johnson and Cook and Zerelli Armstrong constitutive equations. Their results were validated with Taylor tests with the same method that Johnson and Cook used in their research [11]. It was of importance that the Zerelli-Armstrong relationship gave a much better result at the higher strain rates as compared to the Johnson-Cook equation. Thus, the work showed the importance of actually associating a macro-scaled model such as the Johnson-Cook flow equation with the microscale. The Zerelli-Armstrong relationship has a built-in set of parameters that are micromechanic. Therefore, an investigation of the Johnson-Cook expression associated with micromechanic scaled properties becomes important to make sure the expressions give reasonable results for high strain rates.

During the same period, research into the coatings used on the rails was carried out by Cruthirds and Blomer in 2005. Cruthirds found that epoxy and polymer laminates unfortunately do not produce an appreciable amount of stress mitigation on the rail, so coatings could not completely solve the problem [12]. However, the coating did provide some benefit. Blomer did a study finding that epoxy coatings provided the best cost/effectiveness trade-off (31% effective compared to 25% effective for the oxide coating) [13].

Cinnamon worked with Kennan to improve the CTH model, and was able to update the Johnson and Cook model with experimentally determined parameters for Vascomax300, calibrating them in CTH for higher strain rates using flyer plate experimental data [9][10]. He also compared the Zerelli-Armstrong model and the Johnson and Cook parameters, and found the Zerelli-Armstrong model did a better job at predicting the stress-strain response at higher strain rates. However, AFIT's preferred finite element modeling program, ABAQUS, did not have the Zerelli-Armstrong model

built-in. So, the Johnson and Cook model has been used moving forward [9].

In addition to the modeling work, Cinnamon was able to perform a metallurgical analysis of rail gouges, and established that a thermal pulse had gone through the material. He was later able to reproduce the gouging phenomenon in the lab using 1D penetration theory and work from Pendleton with the Buckingham Pi theory to extend his results to the sled system [14]. Through this work, he discovered that the slipper encountering a misalignment of 0.02cm could trigger gouging and cause the melting behavior seen in the rail. This was a telling conclusion, as 0.02cm was only 32% of the allowable rail misalignment.

Cinnamon’s conclusions marked the end of the gouging phenomenon investigation, and the start of shifting AFIT’s research to other damaging effects of high-speed sliding; namely, wear. In 2007, Cameron started looking into how the model for gouging could be used to predict the overall removal of material from the slipper after a run at the test track [15][16]. He was able to compare his results to experimental data collected from Holloman’s Dynamic Analysis and Design System (DADS) during a run in October 2000 (Mission80X-A1). DADS provided extensive information, including heating and velocity profiles that were used as inputs into the model. The vertical velocity and force profiles are shown below in Figure 2.

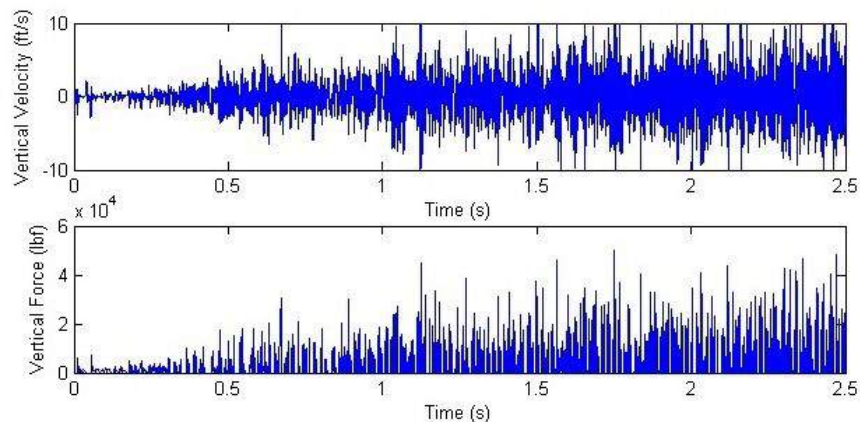


Figure 2. DADS Data from October 2000 Mission 80X-A1 [15]

Modeling was found to be extremely challenging; it was determined that an asperity needed to be present in the simulation to produce any measurable wear, and there were also limitations because of the short run time on the simulation, only a few seconds.

Cameron also attempted to form an analytical model by extending a low speed wear equation developed by Lim and Ashby, but results produced by both methods did not match [17].

Work continued on the CTH model, but Chmiel in 2008 forged into finite elements with his thesis, where he investigated the feasibility of using ABAQUS to make these predictions [18]. He made two models: one macro model based on Archards Wear Law, and one micro sub-model based on Cameron's CTH model [19]. The macro model was a bit cumbersome. It involved a Python script that worked in combination with ABAQUS in an iterative process. ABAQUS would predict the pressures at a time step, and the script would calculate the wear predicted by Archards law at that step. This model ran into numerical issues often, so it was not favored. The micro sub-model on the other hand seemed to have fewer issues. It used microscopic asperities 0.04mm tall and 0.4mm long in a kind of wave pattern to calculate a local value of wear, to be extrapolated to the global wear event. The Johnson and Cook constitutive model was used, and to determine when the material was failing, a ductile failure damage initiator developed by Hooputra et. al. was used [20].

In 2008, there was another experiment at the HHSTT that provided valuable DADS data, plus a 3rd stage slipper for further investigation. Hale in 2010 [2] continued work on Chmiels ABAQUS model, changing it from a wave profile to a single asperity collision. Through metallurgical analysis, Hale found that slipper was experiencing plasticity effects, and that temperatures generated during the experiment were resulting in phase changes in the steel. It was determined that wear is a 3D

event, and to use a 2D model one must add a factor to account for the additional dimension. Thus, Hale developed a method to integrate the wear caused by one asperity over an area and apply to the 2D results. In the end, Hale's model was able to predict 36% of the total observed wear in the 2008 test run.

Meanwhile, Meador continued work with the CTH model [4]. He divided the wear into two different components pure mechanical wear, and wear caused by melting. He found that by changing the initial temperature, the wear results were drastically affected. Additionally, the heat transfer coefficient being used was unrealistic and over-predicting wear. The factor was changed from 0.5 to 0.125. He did some work on determining the thermal profile of the slipper using the 1D heat conduction equation, but found that since the CTH model is on such a small scale and based on the metallurgical work done by Hale, it was reasonable to keep the temperatures constant for a depth of $400\mu\text{m}$. He also confirmed that a $1\mu\text{m}$ by $1\mu\text{m}$ mesh in CTH was sufficient to capture the wear behavior. Since this work was on-going at the same time as Hale's dissertation, Meador was able to implement the 2D-3D conversion factor Hale developed into CTH, and added an additional scale factor to account for bouncing occurring during the test run. The failure model was also changed from the ductile initiator to a specific critical strength criteria. In the end, Meador's melt model predicted 20% of the total wear from the 2008 run, and the mechanical model predicted 80-100%. He calculated total material removed from the slipper, finding that 2.83-6.03% of the slipper would wear away depending on what failure criteria was in use. The experimental value measured from the worn slipper was 3.47%, so this seemed quite good. It was noted that Johnson and Cook had a failure criterion that was materials-based and might have more accurate results.

Huber continued to refine the CTH mechanical model and experimented with additional von Mises failure criteria, but was still only able to account for 49.31-

80.87% of the experimental wear from the 2008 mission [21]. In 2012, Wuertemberger was able to implement the Johnson and Cook damage criteria in CTH, and was able to make direct comparison to the ABAQUS results, which were found to compare very well [22]. However, when compared to a new 3D model that was being developed by Buentello, it was determined that CTH over-predicted the total wear. Efforts were made to create a 3D CTH model, but challenges with the amount of data created from the simulation and the drastic increase in simulation time were encountered which resulted in the ABAQUS model being chosen for further advancement.

Gracie Paek-Spiel and Kathleen Le both did work regarding the thermal environment of the slipper. Paek-Spiel attempted to build a mathematical model to characterize the thermal distribution into the slipper that would account for the dynamic nature of the bouncing phenomenon and the high speeds that are being encountered. She produced a 1D model using an infinite half space as a boundary condition and used the steady-state solution to relate the velocity to the thermal penetration depth [23]. Le then had the challenge of implementing this model. From Paek-Spiel's work, she was able to define a partition function for the fraction of heat that entering into the slipper verses the heat entering into the rail [24].

In 2013 Buentello finished up his work on implementing a 3D ABAQUS model [1]. His progress was a great leap forward as it eliminated the need for 2D to 3D conversion factor. He was able to include a friction model (a feature lacking in CTH), used the Johnson and Cook constitutive model and damage criterion, and the Mie-Grunieson equation of state. The model was used with a number of different sized asperities and even reproduced wear patterns that matched those seen on the worn slipper surface. It is becoming more apparent that heat plays a very large role in the wear process. Initial temperature input is significant, and it is noted the specific heat parameter is not one that can be assumed constant, rather, it is a function of

temperature and will change as the slipper heats during the sliding event. In the end, Buentello produced an ABAQUS model that is capable of reasonably predicting the wear of a high strain rate sliding event, proving that ABAQUS has overcome most of its limitations when dealing with high strain rate problems.

Christopher Alban worked on models to more accurately represent the temperature distribution that occurs during a test run and estimate melt wear. Building on work done by Kathleen Le, Alban attempted to improve the heat modeling with updated material parameters and make a new 2D finite element melt wear model that could be applied to more surfaces in ABAQUS than just the top and bottom, better simulating the heating from aerodynamic effects [25]. He found that the melt wear was highly dependent on the inputs loading, contact time, heat flux properties, and material properties. In fact, updating Le's model changed the results so that no melt wear occurred. It highlighted the complicated nature of the heat problem, and helped point out further issues for investigation.

While Buentello focused on high speed wear, Cavallaro focused on low speeds. [26] He took over the model and attempted to compare it to low speed experiments carried out by Lim and Ashby. It is notably more difficult to model low speed strains, because of the length of time it takes to run the simulation is markedly longer and thus more prone to instabilities developing. His work did result in reasonable predictions of low speed wear, and after this success he began playing with material parameters (specific heat capacity, Johnson and Cook constants). First he tried varying the specific heat capacity with updated table values, then keeping specific heat constant as Buentello did before but trying low speed Johnson and Cook parameters, and then applying both changes. Predicted damage changed dramatically, by 60% less in the case of the tables, and 85% less when the Johnson and Cook low speed parameters were used. Trying both together resulted in a 75% wear decrease. This once again verifies that

the specific heat constant is vital to wear prediction, and brings up a new question of how valid are Johnson and Cook parameters for different strain ranges?

In summary, for the past several years the students at AFIT have put extensive work into the modeling of high strain rate wear and have successfully gone above and beyond the original goal of solving the gouging problem that first fueled this research. As more work goes into the problem even more questions rise up, but great progress has been made in understanding the mechanisms involved in high speed wear. This research project will attempt to drive that understanding even deeper with additional high strain rate experiments carried out at UDRI, and new imaging techniques not used in any of AFITs previous work. The major thrust here is that a better approach of the micromechanic properties of a given metal (4130 steel) in a phenomenological model such as the Johnson-Cook relationship may improve the value and validation of all the previously described work.

1.3 Goals of the project

The object of this research is to characterize a heat treated 4130 steel for the Johnson-Cook strength and damage coefficients to further support modeling efforts for HAFB. Secondly, to investigate microstructural characteristics and determine if temperature or strain rate are main drivers of microstructural changes. Microstructure-macroproperty relationships can give insights into improvements of the modeling being completed. Deriving specific mathematical relationships is outside of the scope of this work. However, the answer to whether it is possible to connect the Johnson-Cook parameters to functions associated with micromechanic functions and potential correlations is addressed.

The chapters that follow attempt to explore this idea. In the next chapter, the theory behind deformation mechanics is described, as is the general approaches for

modeling deformation numerically. Special considerations are addressed for dynamic impacts and thermal conditions, and constitutive equations and damage criteria are explained. The concept of deformation modeling and its connection to materials is introduced. Chapter III goes over the experimental program carried out at University of Dayton Research Institute (UDRI) to acquire the Johnson-Cook coefficients for heat-treated 4130 steel, and shows the results of the experiments. Chapter IV demonstrates the fitting for both the Johnson-Cook flow and damage equations, solves for the coefficients and validates the results. A finite element program is constructed and compared against the experimental results, and then the same is done for an analytical solution carried out in MATLAB. In Chapter V, the microstructure of failed specimens is examined and characterized in the elastic and failure regions of the samples, then statistically analyzed using Analysis of Variance (ANOVA). Relationships are formed between the micromechanic results and the Johnson-Cook flow and failure equations. Finally, the major conclusions of this study are summarized in Chapter VI. An appendix follows containing additional information related to this project.

II. Theory

This chapter is an introduction to how material response is characterized using stress-strain curves. First, stress-strain curves are introduced and then used to show how different equations can represent different portions of the curve. Complications related to strain rate and temperature are added, and then constitutive models and damage criterion are introduced as a way to address these complications.

2.1 Stress-Strain Curves

This research characterizes how stress and strain of heat-treated 4130 responds in dynamic impact situations. Stress and strain are used together to describe the response of materials to applied forces. This is a response that one could typically obtain experimentally from a metal by running tension tests, measuring the applied force and changing diameter of the tested specimen. Figure 3 shows the typical stress-strain response of a metal. Generally, materials have two distinct regions of behavior

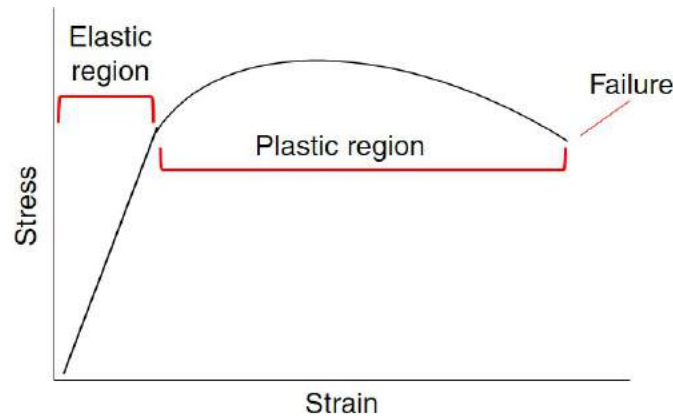


Figure 3. Typical engineering stress-strain curve showing the elastic and plastic regions of deformation

- an elastic region and a plastic region. The beginning, linear portion of the graph is the elastic portion of the response, and the second portion, which is non-linear,

is the plastic portion of the graph. The two regions are divided by a yield stress, typically determined by a yield function (for example, the 0.2% offset method, or the von Mises yield function).

Mathematical equations developed to describe real-life deformation behavior are essential for modeling purposes. Expressions that predict the stress during deformation are known as constitutive laws, and will be further described in the following section. One can describe deformation using relationships and material properties derived directly from the experimental data. Hooke's law, which is a constitutive law that uses a material property to describe linear elastic deformation, is a simple example of this.

Hooke's law depends on the material property of Young's Modulus (or the elastic modulus). It is the proportionality constant between stress and strain for the elastic portion of the stress-strain curve. It is obtained for every material based on results from a low strain rate tensile test. Hooke's law is based on the observation that for many materials, the experimental stress-strain behavior in the elastic region is linear. Simplified for a one-dimensional case, the stress can be represented one-dimensionally as:

$$\sigma_e = E\epsilon_e \tag{1}$$

where σ_e is the elastic stress, E is the elastic modulus, and ϵ_e is the elastic strain

Elastic behavior may not only behave linearly, however, so Hooke's law may not always be the right choice for modeling. Linear viscoelastic behavior, where the elasticity is rate-dependent, can also be modeled using analytical equations such as the Maxwell and Kelvin models. To know what model to use, one must have some general idea of how the material behaves experimentally beforehand.

The example of Hooke's law as a constitutive law only applied to the elastic region of a stress-strain curve. Similar principles apply for the plastic region. Not only do we

have to deal with nonlinear behavior from viscous contributions (time-dependence), but also confounding behaviors from strain rate and material damage. Figure 4 gives an idea of how the plastic regions of the stress-strain diagrams can differ based on the introduction of some of these dynamic effects.

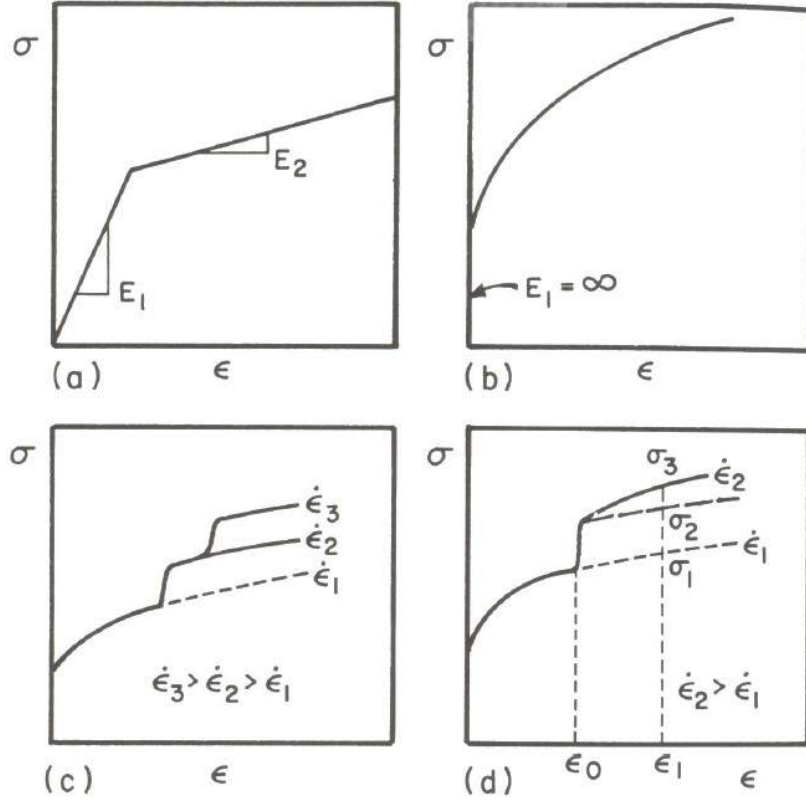


Figure 4. Examples of plastic behavior for (a) perfectly plastic, (b) strain hardening, (c) rate dependent, and (d) time dependent materials [27]

The Figure 4(a) depicts a perfectly plastic behavior situation with a linear plastic portion, and assumes that it behaves similarly to how a linear-elastic curve might act. Figure 4(b) shows an additional hardening effect with increasing strain. Figure 4(c) shows how an increasing strain rate will increase the plastic stress, and Figure 4(d) shows how the timing of an applied strain rate may also affect the flow stress [27].

All of these characteristics are important in this research, and will be discussed in more detail in later sections.

Thus far, the equations developed have been developed using relationships derived from observations of experimental results. There is a growing field of study attempting to create these models based on the internal structures of materials. There are different scales that can be used to approach this, shown the Table 1:

These relationships can be built if one considers the various scales of the internal structural changes occurring during deformation. As a material is being deformed, the internal structure of the material is undergoing changes. Metals are constructed out of crystal grains formed by repeating arranged layers of atoms. For any deformation to occur, these atoms must shift. Knowing the structure of the material and having an idea of what the applied stress is doing internally can allow for an alternate description of deformation. For example, Young’s Modulus for an isotropic hexagonally-packed material can be described as [30]:

$$E = \frac{\sqrt{2}n(m - n)\alpha}{a^{n+3}} \quad (2)$$

where n and α are atomic attraction energy constants, m is an atomic repulsion energy constant, and “ a ” is the closest packing parameter for a hexagonally packed material.

So one-dimensionally, the linear deformation of a hexagonally-packed material

Table 1. Scales of material modeling [28] [29]

Unit	Length Scale	Timescale	Mechanics
Complex structure	10^3m	10^6s	Structural mechanics
Simple structure	10^1m	10^3s	Fracture mechanics
Component	10^{-1}m	10^0s	Continuum mechanics
Grain microstructure	10^{-3}m	10^{-3}s	Crystal plasticity
Dislocation microstructure	10^{-5}m	10^{-6}s	Micromechanics
Single dislocation	10^{-7}m	10^{-9}s	Dislocation dynamics
Atomic	10^{-9}m	10^{-12}s	Molecular dynamics
Electron orbitals	10^{-11}m	10^{-15}s	Quantum mechanics

could be expressed [30]:

$$\sigma_e = \frac{\sqrt{2}n(m-n)\alpha}{a^{n+3}\epsilon_e} \quad (3)$$

For the full derivation, see Appendix A.

This expression does still have some caveats, however. It is built off of the principles of an energy balance of an applied force on an hexagonally-packed structure with two atoms being forced closer together than their equilibrium state would normally allow. There are additional factors that might add to that energy balance and alter the equation, such as temperature, strain rate, time-dependence, and stresses caused by other flaws in the atomic arrangement (dislocations). This is reflected in the variation of experimental results of materials, and their dependence on material and loading situations [27]. The disadvantage of many of these expressions, however, is their practicality and feasibility of usage. There are not published values on n and m , and it is unclear whether this relationship is only valid at an atomic scale or whether the main constants scale up to the macroscale (scalability). While this is a much more physically accurate way of describing the deformation, without knowledge of the atomic repulsion and attraction constants, one could not actually use it to predict deformation. However, the relationship is still useful for understanding the fundamentals of what is occurring.

The aforementioned example is based on elastic principles, where deformation is recoverable. The principles in the plastic region would differ since the deformation is permanent. In this case, atoms slide over each other completely instead of just pressing together, leading to internalized shear. Polycrystalline materials do this in a somewhat organized fashion, as they have preferred slip planes, or slip systems, that they will glide along while deformation is occurring once a critical stress has been reached. The minimum value for this is the Peierls-Nabarro stress, but obstacles and stress fields from said obstacles can increase this number [31].

Steel is composed primarily of iron, alloyed with carbon and a particular cocktail of other elements to round things off. Thus, much of the behavior of steel is governed by the behavior of iron. Iron is an element that is allotropic, which is a chemical property that allows some elements to exist in different forms in the same state (solid), so it will have a different structure depending on what the conditions are. At room temperature, iron has a body-centered cubic atomic structure (BCC), known as the ferritic phase. At higher temperatures, ($\geq 912^\circ\text{C}$) iron re-arranges itself into a different phase called austenite with a face-centered cubic atomic structure (FCC). The structures of these are pictured in Figure 5.

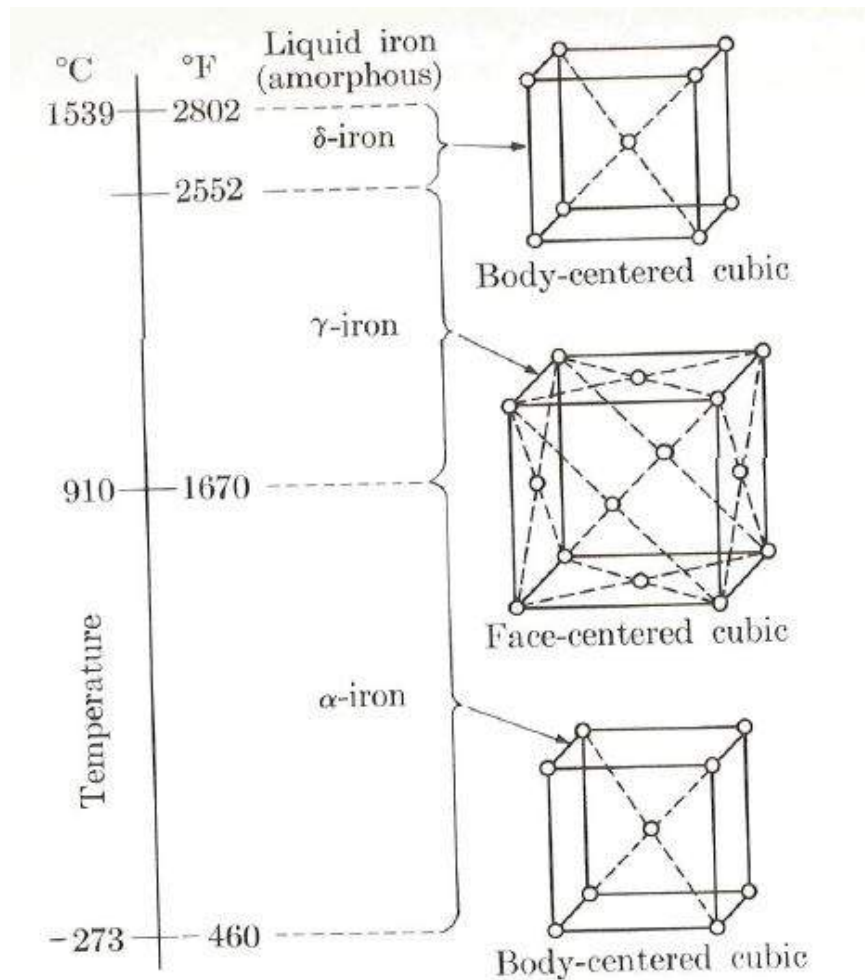


Figure 5. Temperature ranges in which the allotropic forms of iron exist in equilibrium conditions. [32]

Structure and fracture.

Knowing about the internal structure can also help determine how the material will fracture. For failures that occur at room temperature or above, the failure will be in a ductile mode as opposed to a brittle mode [33]. In a ductile mode, voids will gradually form in a metal causing it to stretch prior to fracture. In a brittle failure mode, the metal reaches a critical stress and fractures suddenly without stretching.

Knowing what phase the steel is in will indicate what crystallographic plane the failure will occur. These planes are described in Miller index notation. This notation system is designed to describe where the planes of a crystal plane would intersect a set of axes. For example, a series of planes and their notation are shown in Figure 6.

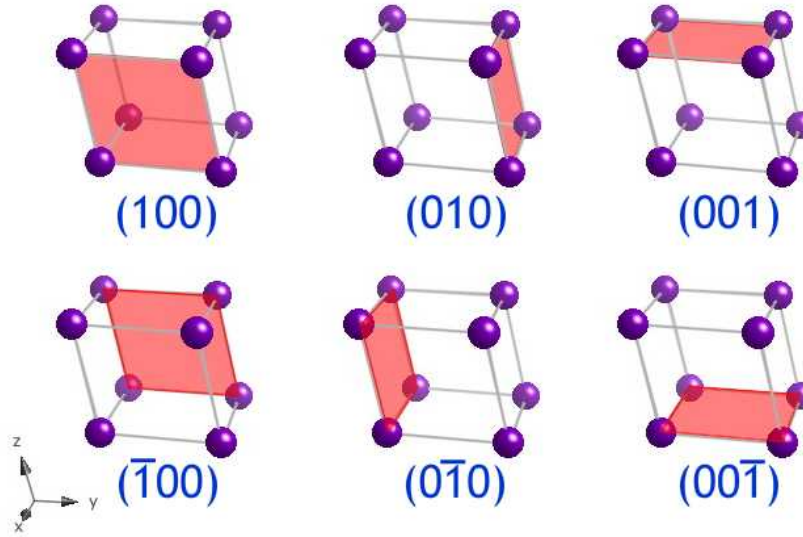


Figure 6. Planes of crystal lattices [34]

For austenite, an FCC structure, slip will occur on the $\{111\}$ family of planes in the $\langle 110 \rangle$ directions (diagonals on unit cell). This gives a total of 12 preferred slip systems. The perfect dislocation Burger's vector is $a\sqrt{2}/2$ [35]. For ferrite, which has a BCC structure, the slip planes are the $\{110\}$ $\{112\}$ and $\{123\}$ plane families in the $\langle 111 \rangle$ directions, which gives a total of 48 possible slip systems. Typically though it

has a preference for the (110) plane in the [111] direction. The Burger's vector for a perfect dislocation is $\sqrt{3}/2$ [35].

Knowing the structure of a material can give insight to the expected slip systems and dislocation vectors. Even so, it can be difficult to capture everything going on within the confines of a practical equation. A deep understanding of the micromechanics is required to obtain an equation on this level. The next section will jump further into the additional considerations and behaviors one must be aware of for dynamic and thermal situations.

2.2 Dynamic and Thermal Effects

Regular plastic deformation is challenging to model no matter the scale, but dynamic and thermal effects add further degrees of difficulty to the process.

Generally, it is empirically known that an increasing strain rate causes an increase of yield and flow stress, though the effects become less marked with increasing temperature [36]. As the temperature increases, the flow stress decreases.

What causes the variations in behavior can be best explained micromechanically. As previously mentioned, the deformation of a material is a results of dislocations shifting in a material. Thus, the amount of deformation that occurs is dependent on the rate that dislocations can shift in a material. The following equations are an explanation of what is known so far about how different mechanisms affects the dislocations velocity, and therefore, how that affects the flow stress behavior. When an array of dislocations starts to move, there is internal shear strain created [27].

$$\dot{\gamma} = \rho b v \tag{4}$$

where $\dot{\gamma}$ is the shear strain rate, ρ is the dislocation density, b is the Burger's vector, and v is the dislocation velocity [37].

The shear strain rate can be related to the overall plastic strain rate by adding in a material orientation factor M [38]:

$$\dot{\epsilon} = \frac{1}{M} \rho b v \quad (5)$$

Thus we can see that the strain rate experienced in the material is affected by the velocity of dislocations. But what controls the velocity of the dislocations? Many relationships for the dislocation velocity have been developed, some more successfully than others. Generally it depends on the types of dislocations present (edge, screw), the structure of the material, and internal temperatures. More specifically, it is the result of a sum of contributions from different types of dislocation motions, some of which dominate in different strain rate regimes. There are three categories of motion mechanisms: thermally activated motion, drag mechanisms, and relativistic effects.

Thermally activated dislocation motion refers to motion created by increased vibration of atoms brought about by an increase in temperature. Thermal activation can help dislocations move through short-range barriers (obstacles a dislocation might meet along the way, such as dislocation forests, solute atoms, small angle boundaries, other dislocations, etc), but might not be enough to get through long-range obstacles. Because of this, obstacles can be classified as those short-range ones that can be conquered by thermal motion (thermal) and long-range obstacles that cannot (athermal). The effectiveness thermal motion is greater when there is more vibration. Thus, at higher strain rates where there is less time, for thermal generation, thermal activation is less effective in propelling dislocations along.

Drag mechanisms are internal forces opposing applied stresses, known as the viscous behavior of a solid, which can be approximated as a Newtonian viscous fluid:

$$f_v = Bv \quad (6)$$

where f_v is the applied force on a Newtonian viscous fluid, B is the viscous damping coefficient, and v is this case the dislocation velocity as a result of drag effects. There are many different mechanisms for drag effects, including phonon viscosity, phonon scattering, thermoelastic effects, electron viscosity, anharmonic radiation, and glide plane viscosity. When dislocation drag is dominating, the the flow stress will be approximately proportional to the strain rate.

The final mechanism is dislocation motion caused by relativistic effects, where at high strain rates, the dislocation motion asymptotically approaches the shear wave velocity. It is believed that dislocation motion cannot exceed the shear stress wave velocity, but such a case has been postulated [39].

It has been shown that the rate of deformation is dependent on the velocities of the dislocations moving inside a material, of which there are three different modes of dislocation motion mechanisms that may dominate at different strain rates: thermal, drag (or viscous), and rarely relativistic effects. Applying a high strain rate may change which mode will be dominating the motion, and thus change the flow stress behavior.

As far as thermal contributions go, the application of temperature may increase the speed that thermal obstacles can be overcome, and depending on its effect on grain growth lower the critical stress needed to move dislocations.

Now that there is a background about what is going on internally, we can look at how constitutive equations and damage criteria attempt to model this behavior.

2.3 Constitutive Laws and Damage Criteria

As previously defined, constitutive laws are equations used to predict the stress-strain behavior of materials. These laws have largely been based on experimental results gained from mechanical tests and theories based on these tests. Different

constitutive laws are used to describe different portions of these curves. For instance, separate laws are typically used to describe the elastic portion of the curve as opposed to the plastic portion of the curve. They can either be based off rheological models, or based more phenomenologically on the material itself, where material parameters are determined and fit into constitutive laws. A final third option, are materials-based relationship, where relationships based on microstructure are brought into the mix. These models tend to use meso-mechanic properties - which are properties that are based on the crystal structure and microstructure of the material [28].

We have addressed constitutive laws that predict the flow stress, but have not touched on damage criteria, which flag when a material has failed and can no longer support loads. The formulation of damage criterion is similar to that of constitutive equations. They can be phenomenological, materials based, or use a failure law (von-Mises yield). Both are needed to fully simulate a situation where a material is destroyed. The next section looks more deeply at the equations AFIT has been using for modeling: the phenomenological Johnson-Cook model.

The Johnson-Cook Constitutive Equation.

The Johnson-Cook Constitutive Model was published in 1983 by Gordon Johnson and William Cook as a joint research venture by Honeywell and the U.S. Air Force. At the time, computational modeling was gaining traction, but there were limitations in its capabilities due to a lack of constitutive damage models, particularly for high velocity impact and detonation scenarios. The goal was to be able to create a model that would work for a broad spectrum of materials, but also would not require extensive lab tests that would be expensive and time-consuming. They were able to develop this model that targeted materials subjected to large strains, high strain rates and high temperatures that has been widely accepted in industry today. While they even

admit in their paper that more complicated models will probably give more accurate results, for many, the model is adequate for their needs. The trade-off between the accuracy of results and ease of use, and its wide-spread implementation in modeling makes it an attractive option [11].

AFIT has been using the experimentally-based Johnson-Cook viscoplastic constitutive equation for its research for most of those reasons. It has the form:

$$\hat{\sigma}_y = (A + B\epsilon_p^n)(1 + C \ln \frac{\dot{\epsilon}_p}{\dot{\epsilon}_0})(1 - T^{*m}) \quad (7)$$

where $\hat{\sigma}_y$ is the vonMises or equivalent flow stress, A is the yield stress, B is the plastic strain coefficient, ϵ_p is the plastic strain, n is the strain hardening coefficient, C is the plastic strain rate coefficient, $\dot{\epsilon}_p$ is the plastic strain rate, $\dot{\epsilon}_0$ is a normalizing strain rate (usually 1, but for this study 0.5 which will be explained in Section 3.2), and m is the thermal coefficient. T^* is the homologous temperature, defined as:

$$T^* = \frac{T - T_{ref}}{T_{melt} - T_{ref}} \quad (8)$$

where T is the sample temperature, T_{ref} is a reference temperature (23°C for this study), and T_{melt} is the melting temperature of the sample material, for 4130 steel 1432°C.

A strength (or flow) equation dictates stress-strain behavior beyond the elastic limit. The first set of parenthesis are static stress contributions which include the yield stress and strain hardening behavior [11]. It is based on Ludwicks equation:

$$\sigma_{flow} = \sigma_{yield} + B\epsilon_p^n \quad (9)$$

where σ_{flow} is the post-yield stress, σ_{yield} is the yield stress, and B and n are strain hardening coefficients [40][27]. It was developed based on experimental observation

[41].

The second set of parenthesis describes the strain rate behavior. It is based on a simple logarithmic model proposed by Ludwik and used by Lindholm [42].

$$\sigma = \sigma_{yield}(1 + C \log \dot{\epsilon}_p) \quad (10)$$

The third set of brackets describes temperature effects, where increasing temperatures causes the flow stress to decrease. The homologous temperature is used to normalize the material temperature against a reference temperature. Thermal contributions are quite important for AFIT's research since the rocket sled wear event being modeled experiences extreme temperature fluctuations. Furthermore, it allows the model to include the effects of heat generated internally by the deformation process.

Authors have noted it is more likely that the three behaviors (static stress, strain rate, and temperature) are more interrelated than the way the model currently is formulated, but it has been shown to give reasonably accurate prediction for low-mid strain rate material impacts [27][43][44].

Johnson-Cook Failure Criterion.

The flow equation dictates the stress-strain behavior of a material beyond the elastic limit, but does nothing to predict when the material will fail. For this reason, a damage criterion is needed to flag at what point the fracture will occur. Two years after publishing their strength equation, Johnson and Cook published a complimenting fracture model still geared toward high velocity, high strain rate impacts and creating a complete model. Johnson and Cook were keen on making sure the static material properties were augmented by dynamic material properties and thermal material properties. Particularly, the thermal portion had been neglected in prior

models, so the combination of all three components (static failure, strain rate effects, and temperature) was a step forward for dynamic modeling.

The Johnson-Cook damage criterion is shown below:

$$D = \sum \frac{\Delta \epsilon^p}{\epsilon_f} \quad (11)$$

where D is the accumulating damage, $\Delta \epsilon^p$ is an increment of accumulating equivalent plastic strain, and ϵ_f is the equivalent strain to fracture at the current strain, strain rate, and temperature conditions. Once damage accumulates to the point where the value of D is equal to 1, failure of the material has occurred. The criterion is based on calculating a critical failure strain, shown in Equation 12 [45].

$$\epsilon_f = [D_1 + D_2 e^{-D_3 Q}] [1 + D_4 \ln \frac{\dot{\epsilon}_p}{\dot{\epsilon}_0}] [1 + D_5 T^*] \quad (12)$$

where ϵ_f is the equivalent strain at failure, D_1 , D_2 , D_3 , D_4 , and D_5 are all experimentally determined coefficients, and Q is the triaxiality factor.

The triaxiality factor is the ratio of mean stress to equivalent stress, which fluctuates throughout deformation. It serves as a measure of ductility.

$$Q = \frac{\sigma_m}{\bar{\sigma}_{eq}} \quad (13)$$

where σ_m is the mean stress and $\bar{\sigma}_{eq}$ is the von Mises equivalent stress. The mean stress is defined as the average of the three principal stresses:

$$\sigma_m = \frac{\sigma_{11} + \sigma_{22} + \sigma_{33}}{3} \quad (14)$$

where σ_{11} and σ_{22} and σ_{33} The equivalent stress, or vonMises stress, is defined as:

$$\bar{\sigma}_{eq} = \sqrt{\frac{3\sigma'_{ij}\sigma'_{ij}}{2}} \quad (15)$$

where σ_{ij} is a stress tensor, denoting all directions of shear stresses and normal stresses.

σ_m is only taking stress caused by volume changes, but neglects and stresses caused by distortion effects [46]. It is being directly compared against the von Mises stress which is derived from the strain brought about from distortion [46]. Therefore the triaxiality coefficient is directly comparing the stresses caused by volume changes to those brought about from distortion changes.

One can make an observation based on the formulation of Q : that when a problem is uniaxial, all stress tensors but σ_{11} cancel, leaving a constant Q value. Thus, one-dimensionally, the equivalent strain at fracture is equal to the failure strain. However for all other cases, the two are not necessarily equal.

It should be noted that in the original Johnson-Cook development, D_3Q is actually a positive term in Equation 12. Also, Johnson and Cook note that this equation is only valid for triaxiality values up to 1.5 ($Q \leq 1.5$). Beyond that, a different equation must be used [45].

As a dynamic event is proceeding throughout the plastic deformation, damage will begin to accumulate. The D value is an attempt at tracking the slowly accumulating damage, while constantly updating a critical strain value where failure will occur. Once the accumulated damage strain and calculated equivalent strain at fracture value match, the simulation program is alerted that the material has failed, and it is removed from the simulation in some fashion. In simulations, the failed element in a finite element model is phased out by setting the stress tensors equal to zero [45]. In ABAQUS (the commercial finite element program used in this study), it is gradually

phased out through a damage evolution, but the approach varies between programs.

The formulation of the failure strain Equation 12 is similar to the strength equation, Equation 7. $D_1 - D_3$ are stress state coefficients related to ductile metal fracture mechanics, D_4 is correlated with rate sensitivity, and D_5 accounts for temperature effects. The first bracketed set in the equation, $[D_1 + D_2e^{-D_3Q}]$, is based off a model from Hancock and Mackenzie:

$$\bar{e}^f = \bar{e}_n + \alpha e^{\frac{-3\sigma_m}{2\sigma}} \quad (16)$$

Where \bar{e}_n is the void nucleation strain and α is a material dependent hole growth rate [47]. As ductile metals undergo failure, voids begin to form until they reach a critical size and rupture, causing failure of the material. Hancock and MacKenzie's equation predicts when critical void formation occurs in ductile metals. D_1 , D_2 , and $-D_3Q$ roughly correlate to \bar{e}_n , α , and $e^{\frac{-3\sigma_m}{2\sigma}}$. In the Johnson-Cook damage equation, the first bracket indicates "the strain to fracture decreases as the hydrostatic tension σ_m increases." One can see from this series of equations a need to recognize the meso-mechanical attributes of the materials response. Again, this verifies the comment previously pointed to in the material deformation discussion.

Deformation mechanics and how they are modeled and the specific model being used by AFIT has been overviewed. However, there is general agreement that the Johnson-Cook model is somewhat limited in its application and that materials-based constitutive/damage equations have the growth potential to better predict stress-strain behavior. In the next section, how others have incorporated meso-mechanics to make improvements in constitutive modeling will be covered.

2.4 Current Work

Previously, how material characteristics could be used to explain macromaterial behavior with the derivation of the elastic modulus was shown. While that specific formulation was not terribly practical, others have had better success in pulling in mesomechanics into modeling to make improvements. The following are a few examples of cases where researchers have applied to modeling materials at high strain rates and high temperatures.

Attempts have been made to incorporate dislocation behavior to explain the macroproperties observed in empirical behavior as they have been for the elastic properties. Some, like yielding behavior and the yield point, are well understood, while others with more complicated interactions are still being worked on. If there was better understanding of what conditions create certain types of dislocations, grain growth, or boundary movement, it might be possible to make progress on such correlations with the behavior seen in our own research model.

Knowledge of micromechanical behavior is extremely beneficial for formulating and even improving modeling behavior. As heavily documented in literature, the starting structure of the material plays a huge role in what kind of behavior will be seen. As touched on earlier, whether a material has a body center cubic or face center cubic arrangement determines what the main failure mode will be in dynamic loading [48]. There is now a field devoted to grain boundary engineering, where material properties can be improved by manipulating the grain size and orientation of a material. For example, to improve corrosion resistant and ductility [49].

There are numerous examples of microstructure being related to behavior seen at different strains, strain rates and temperatures. When hypervelocity experiments were done on a magnesium alloy, a hexagonal close packed structure, it was found that twinning and dislocation slipping were the main modes of plastic deformation.

Because of this, equiaxed recrystallized grains were formed, resulting in a dramatic increase in yield strength. If one were to attempt to model the flow stress of this material, for more accurate results it should take into account the development of small grains during deformation [48].

Gubicza et al. did a study on several metals with a face center cubic atomic arrangement subjected to large strains. They found that the individual crystallites became smaller while the dislocation density increased. The yield strength increased until a saturation point was reached at a high strain [50]. The yield strength increased because of the accumulation of dislocations in grain and subgrain boundaries, which also resulted in a decrease in ductility. Ductility could be restored when the dislocation density decreased and the domain size increased, which leads to the grain boundary size decreasing and an increase in misorientation. This tells us that when modeling these materials, the temperature will play a large part on what the yield strength will be, as rising temperatures will decrease the grain boundary size and therefore increase the ductility and amount of plastic strain a material can experience.

Qin et al. did a study on dislocation behavior in the framework of strain rates. Adding rate dependence into the mix produces complications such as glide interactions and forest dislocations, thermal activation, and strong barriers to dislocation due to the high rate of deformation [51]. They noted the popular Hall-Petch equation does not take strain rate into account, which is a well-established equation showing how a mesomechanic parameter, grain size, can be linked to the yield stress. The Hall-Petch relation is shown below in Equation 17.

$$\sigma_y = \sigma_0 + \frac{k_y}{\sqrt{d}} \quad (17)$$

where σ_y is the yield strength, σ_0 is the starting stress needed to get dislocations

moving, k_y is a material strengthening coefficient, and d is the average grain diameter.

It is used to show how the grain size affects the yield strength of a material. Smaller grains result in a higher yield strength because fewer dislocations are present, and it takes more force to move small dislocations from grain to grain than larger dislocations.

Qin tried to take a deeper look at the kinematics and dynamics behavior of the dislocations, and included Orowan’s relationship relating strain rate and dislocation motion:

$$\hat{\epsilon}_p = \alpha b \rho_m \bar{v} \quad (18)$$

Where $\hat{\epsilon}_p$ is the flow strain, α is a material constant, b is the the Burger’s vector, ρ_m is the dislocation density, and \bar{v} is the dislocation velocity vector.

Their conclusions were interesting, and found that the stress dependence of dislocation velocity controls the plastic flow stress. In their own words, “Strain rate criteria rather than stress criteria should be satisfied when a material yields at a given stress rate.” This suggest that perhaps the damage criterion that are stress-dependent such as the vonMises criterion may not be adequate. Rather, methods that can predict the dislocation velocity present within a material would give better results.

For example, by noting that at a certain strain rate threshold (over $10^3/\text{sec}$), dislocations move from being thermally activated to a viscous regime, Couque and Boulanger were able to modify the Johnson and Cook model to dramatically improve its prediction power at higher strain rates, as illustrated in the Figure 7 [52].

These are just a few examples of where knowledge of the microstructure can point to dependencies that need to be accounted for in viscoplastic constitutive modeling. Moving forward with this study, it will be of interest to look into what can be discovered about the microstructure that may point to improvements in our approach

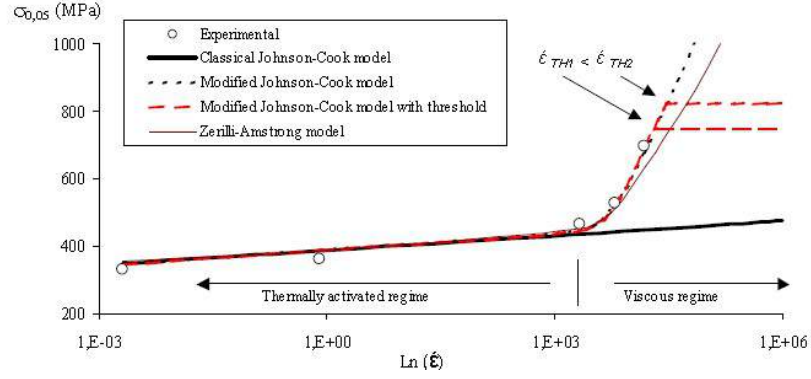


Figure 7. Modified Johnson and Cook model [52]

to the modeling used.

2.5 Theory Conclusion

The Johnson-Cook relationships have several parameters based on experimentally observed behaviors, but may not be matching with what is occurring in the microstructure. This idea can be further explored by analyzing material's microstructure that has been subjected to different strain rate and temperature conditions. By doing just this and analyzing the results for statistical significance, we should be able to make correlations between the material parameter and microstructural observations. The next chapter outlines the experimental program undertaken to determine the Johnson-Cook constants for heat-treated 4130 steel, and tangentially, the conditions the material is subjected to for material analysis.

III. Experimental Program

3.1 Planned Experimental Review

In June of 2014, an experimental program was undertaken at UDRI to evaluate the dynamic response of heat-treated 4130 steel at various temperatures and strain rates [53]. The primary goal was to obtain the necessary data to calculate the Johnson-Cook flow and failure material parameters, with a secondary goal of investigating the the failed specimen microstructure afterwards. The following section is an overview of the experimental program details, starting with details about the heat-treatment and composition of 4130 steel, dimensions and fabrication of the specimens, experimental conditions for the program, and finally the resulting stress-strain curves collected. Once this has been completed, the next chapter will cover how this data is used to generate the Johnson-Cook coefficients.

Material Treatment and Composition.

The material of interest is 4130 steel that has undergone a heat treatment. Annealed 4130 steel is first manipulated to drawing specifications, heated above its critical austenitizing temperature changing the structure to FCC, 1675°F (910°C), quenched returning the structure to BCC, and then tempered at 1050°F (566°C) until it reaches a strength of 120-140 ksi (827-965 MPa).

The specific composition of 4130 steel is shown in Table 2.

Sample Manufacturing.

Experiments were carried out at UDRI with samples supplied by Holloman AFB. Samples were machined from the same treated AISI 4130 steel used for rocket sled slippers. Two types of samples were manufactured: notched specimens for triaxiality

Table 2. Percent composition of alloying elements of 4130 steel [54].

Element	Percent Composition
Carbon	0.23-0.33
Chromium	0.80-1.10
Iron	97.3-98.2
Manganese	0.40-0.60
Molybdenum	0.15-0.25
Phosphorous	≤ 0.035
Silicon	0.15-0.30
Sulfur	≤ 0.040

determination, seen in Figure 8, and smooth, ASTM sub-size E8 dogbone samples for tensile testing seen in Figure 9. Prior to experimentation, measurements of the diameters and lengths of the all samples were recorded.

The notched triaxiality test samples are 2 inches (50.8mm) in length with a diameter of 0.325 inches (8.255 mm) and are machined with one of 3 different notch sizes: 0.4mm, 0.8mm, and 2.36 mm. Five samples of each notch radius were fabricated. However, tolerances were unable to be met on the notch sizes and they were manually turned into the samples. This left a rough surface finish and uneven radii. To account for this, the radius of each sample was measured using digital comparator. Each sample was measured 3 times, rotating the sample by approximately 120 degrees for each measurement. The radii for 0.4mm radius varied between 0.448 and

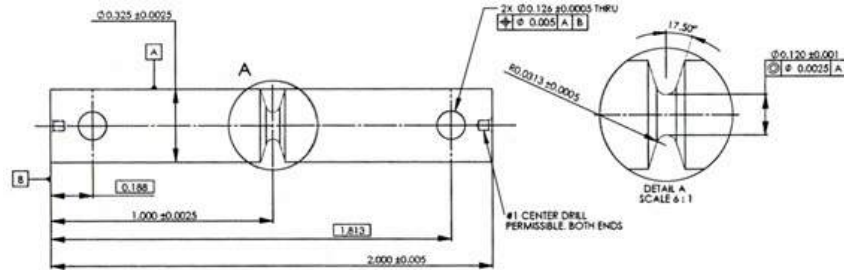


Figure 8. Diagram of notched triaxiality determination sample, shown with the 0.8mm radius (Dimensions are in English units).

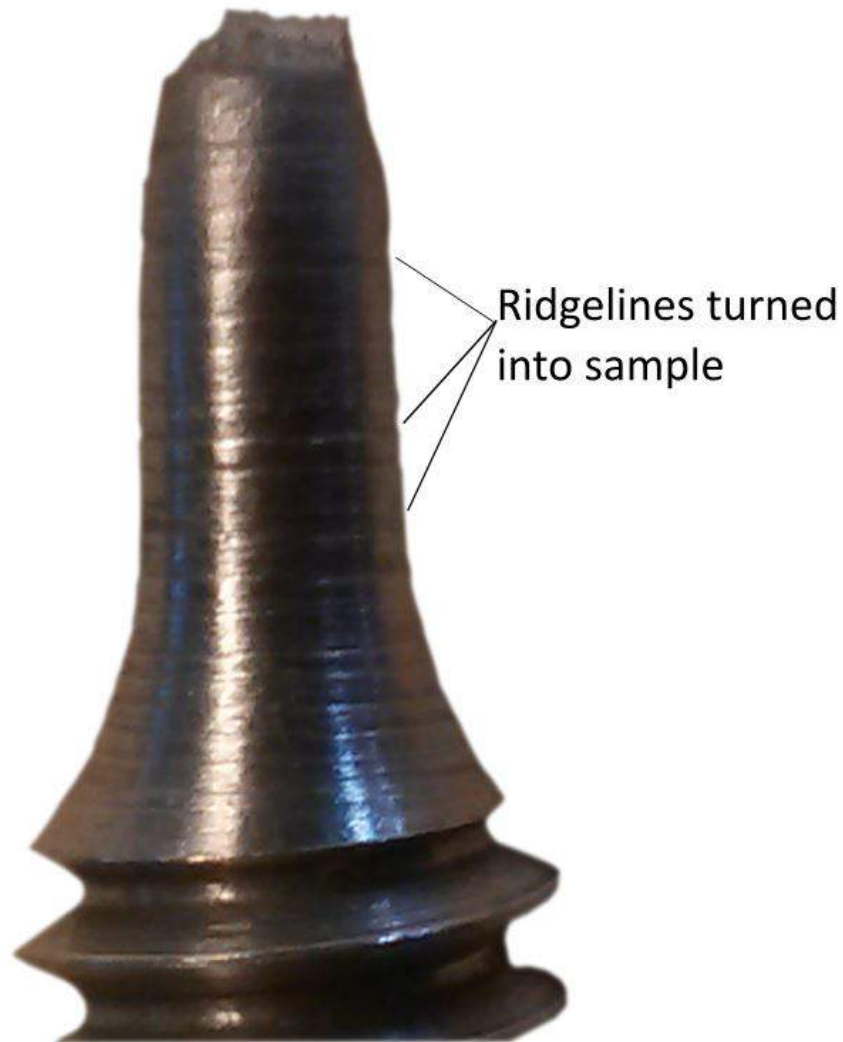


Figure 10. Sub-size ASTM E8 threaded dogbone specimens. Rough machining visible in jitter marks on the threads of the specimen and the turning marks on the gage length. Photo credit to Ron Hoffman.

It shows each of the different test condition, the equipment used for the experiment, and the number of samples run for each condition. For each condition, three samples were tested. For the 0.01 and 0.5/s strain rates, the experiments were run at room temperature on a servo-hydraulic test stand. For the 500, 1000, and 1800/s strain rates, the experiments were run at four different temperatures (24°C, 223°C, 466°C, 707°C), on Split-Hopkinson Bar test stand. In the next section, the details of the test stands and equipment is reviewed in more depth.

3.2 Tension Test and Split-Hopkinson Bar Overview

Low Strain Rate Tension Test Equipment: Servo-Hydraulic Test Stand.

An MTS servo-hydraulic station (#5), equipped with a 44.4 kN actuator, is operated at room temperature for tension tests at lower strain rates. Load is measured using a load cell calibrated through 22.2 kN full-scale, and actuator displacement was measured using a linear variable differential transformer. The full-scale for the stroke was 1 inch (25.4mm), and a slack adapter was used to allow the actuator time to ramp up to speed before applying the test load. An MTS servo-hydraulic station (#5), with a load frame capacity of 89.0kN equipped with a 44.4 kN actuator is operated at room temperature for tension tests at lower strain rates. Load is measured using a load cell calibrated through 22.2 kN full-scale, and actuator displacement was measured using a linear variable differential transformer. The full-scale for the stroke was 1 inch (25.4mm), and a slack adapter was used to allow the actuator time to ramp up to speed before applying the test load. A mechanical extensometer (Epsilon Model 3443-0025-100-HT2) calibrated to 5.1mm (0.2 inches) full-scale with a measuring range of +100%/-5% was used to measure strain [56].

The servo-hydraulic test stand was run at two different strain rates: 0.01/s (quasi-static) and 0.5/s (reference). Normally the reference strain rate is 1/s, however

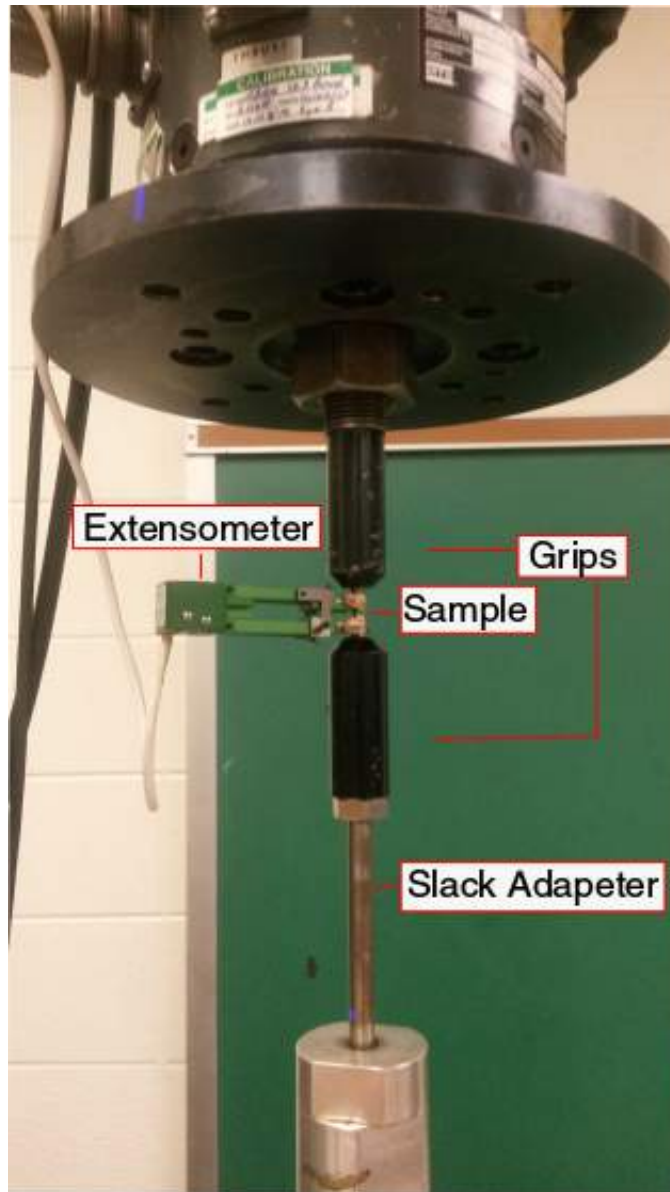


Figure 11. MTS Station #5 located at Kettering Labs of UDRI used for quasistatic and reference strain rate tests at room temperature.

limitations on the testing equipment available at UDRI resulted in a lower testing rate.

High Strain Rate Tension Test Equipment: Split-Hopkinson Bar.

The Split-Hopkinson Bar (SHB), or Kolsky Bar apparatus in a tension configuration is used to generate appropriately high strain rates for the experiments. A schematic of the set-up is shown in Figure 12.

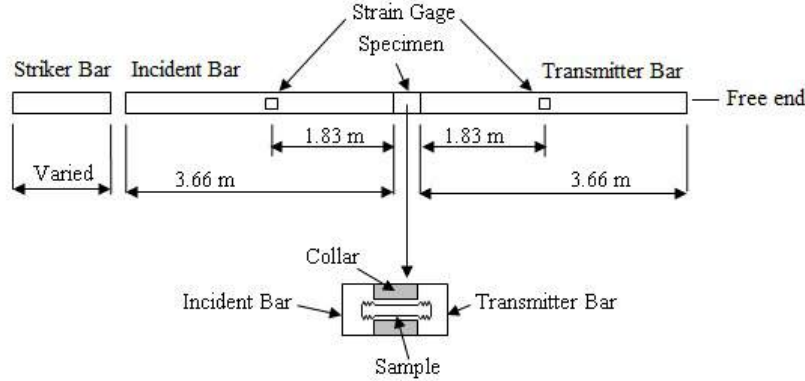


Figure 12. Schematic of Split-Hopkinson Bar experiment. The striker bar impacts the incident bar, sending a stress pulse through the specimen and the transmitter bar. Strain gages record the incident, transmitted, and reflected pulse signals.

The assembly consists of a striker bar, incident bar, material sample, transmitter bar, and two strain gages placed on the incident and transmitter bars to collect data. The bars and projectiles are all made of 0.5 inch (12.7mm) diameter Inconel 718. The strain gages are Constantan foil, type Micro-Measurements type CEA-06-250UW-10C with a gage length of 6.35mm and a strain limit of $\pm 5\%$. They are wired as half-bridge and mounted diametrically to one another, with one on the incident bar and the other on the transmitter bar. The gage factor is $2.130 \pm 0.5\%$. Specimen-to-gage distance is 6 feet (1.83m) for each gage, and is chosen based on the time needed to measure strain in a specimen, which is determined by the striker bar length. The distance chosen allows strain measurements in the specimen of $\geq 60\%$.

Samples are heated via a Lindbergh Cycle Dyne induction unit, Model A-50 (9.2KVA). The induction coil surrounds the collar with the sample inside. The collar has a hole drilled out to allow the insertion of a thermocouple to monitor the sam-



Figure 13. Split Hopkinson Bar test apparatus located at UDRI used for higher temperature and strain rate experiments

ple temperature. Heating was achieved in ~ 20 minutes for the 223°C samples, ~ 30 minutes for the 466°C samples, and ~ 20 minutes for the 707°C samples. For the 223°C and 466°C samples, the heating rate was held at a constant until the target temperature was reached, with no holding time. For the 707°C samples, heating rate was increased while ramping up initially, and then slowed significantly for the final minutes while approaching 707°C .

Split-Hopkinson Bar set-ups are extremely useful for dynamic, high strain rate experiments and can create strain rates ranging from $100/\text{s}$ - $10000/\text{s}$ through the gage length of the material sample [57]. In this experiment, the projectile bar is propelled into an incident bar by a gas gun at velocities ranging from $7\text{-}19\text{m/s}$ generating strain rates from $500/\text{s}$ to $1800/\text{s}$. Depending on the particular set-up of SHB used, stress waves generated in the sample can either be compressive or tensile. This study uses a tensile set-up devised by Nicolas in 1981 whereby a collar is placed around the

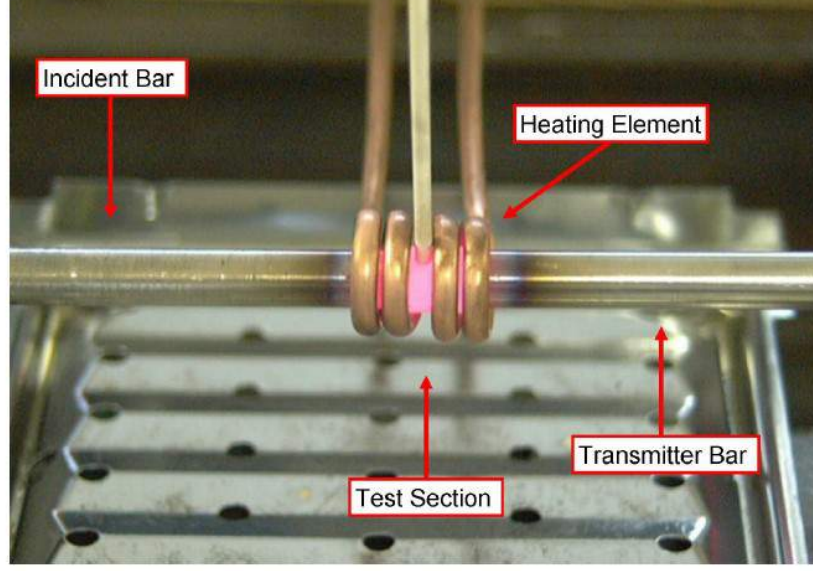


Figure 14. Induction coil used for heating samples at UDRI

specimen so a compressive wave travels over the specimen and then is reflected back as a tensile wave, breaking the specimen in tension during the reflection [58].

Split-Hopkinson Bar Stress and Strain.

The engineering stress and strain of the experiment can be obtained by utilizing elastic wave relations and the stress pulses measured by the strain gages on the incident and transmitter bars [57]. The relevant equations used are:

$$\epsilon_s = \frac{2C_o}{L} \int_0^t (\epsilon_R) dt \quad (19)$$

and

$$\sigma_s = \frac{A_H}{A_s} E \epsilon_t \quad (20)$$

where ϵ_s is the sample strain, C_o is the elastic wave speed of the striker bar (4968 m/s), L is the starting gage length of the sample (8.89mm), ϵ_R is the reflected strain wave, σ_s is the sample stress, A_H is the cross-sectional area of the Hopkinson

bars ($1.27\text{E-}7\text{m}^3$) and A_s is the cross-sectional area of the gage section of the sample measured at room temperature. ($7.92\text{E-}9\text{m}^3$). The full derivation of these equations can be found in Chen and Song's work for compression, and is presented here for tension (also available in Cinnamon's dissertation)[57][9].

A stress pulse is assumed to be:

$$\sigma = \rho C_o V_s \quad (21)$$

where ρ is density of the striker bar material (Inconel 718, 8.19g/cc) and V_s is the striker bar velocity [59]. C_o is found by using the wave equation relation:

$$C_o = \sqrt{\frac{E}{\rho}} \quad (22)$$

where E is the elastic modulus of the bar material (Inconel 718, 202MPa) [59]. In Cinnamons experiment, a specimen is used that causes a tensile wave to go through the section of interest.

First we want to define the displacements occurring in the specimen. We define strain to be:

$$\epsilon = \frac{\delta u}{\delta x} \quad (23)$$

where u is the displacement. We also define stress according to Hookes Law:

$$\sigma = E\epsilon = \frac{P}{A} \quad (24)$$

where E is the elastic modulus of the specimen, P is the pressure force at the ends of the specimen, and A is the cross-sectional area of the Hopkinson bar. We can define the displacements at either end of the specimen as given below:

$$u_1 = \int_0^t C_0 \epsilon_1 dt = C_0 \int_0^t (\epsilon_i - \epsilon_R) dt \quad (25)$$

$$u_2 = \int_0^t C_0 \epsilon_2 dt = C_0 \int_0^t \epsilon_t dt \quad (26)$$

Since this derivation is in tension, u_1 is the sample interface at the transmitter bar and u_2 is the sample interface at the incident bar.

The strain occurring in the sample is just the difference in displacements divided by the samples original length:

$$\epsilon_s = \frac{u_1 - u_2}{L} \quad (27)$$

Substituting in u_1 and u_2 values:

$$\epsilon_s = \frac{C_o}{L} \int_0^t (\epsilon_i - \epsilon_R - \epsilon_t) dt \quad (28)$$

We next are interested in solving for the relationship between the stresses. Using a force equilibrium equation, the forces on both ends of the specimen must be equal. The forces, P_1 and P_2 are given below:

$$P_1 = EA\epsilon_1 = EA(\epsilon_i + \epsilon_R) \quad (29)$$

$$P_2 = EA\epsilon_2 = EA\epsilon_t \quad (30)$$

Equating P_1 and P_2 , we can conclude:

$$\epsilon_i + \epsilon_R = \epsilon_t \quad (31)$$

Making substitutions and simplifications, we can solve for the sample strain:

$$\epsilon_s = \frac{C_o}{L} \int_0^t (\epsilon_t - \epsilon_R - \epsilon_R - \epsilon_t) dt \quad (32)$$

$$\epsilon_s = \frac{2C_o}{L} \int_0^t \epsilon_R dt \quad (33)$$

Similarly, we know the force at the specimen ends must equal the force in the bars. We can build the relationship:

$$\sigma_s = \frac{A}{A_s} \sigma_b \quad (34)$$

where σ_s is the sample stress, σ_b is the bar stress, A is the area of the Hopkinson bar and A_s is the specimen area. Substituting Hookes law in for the bar stress, we arrive at our result:

$$\sigma_s = \frac{A}{A_s} E \epsilon_t \quad (35)$$

Finally, the strain rate is obtained by simply differentiating the strain equation we previously solved in Equation 33.

$$\dot{\epsilon}_s = -\frac{d\epsilon_s}{dt} \quad (36)$$

$$\dot{\epsilon}_s = -\frac{2C_0}{L} \epsilon_R \quad (37)$$

A spectrum of strain rates is needed to demonstrate the effect of strain rate on flow stress. For this specific SHB set-up, 500/s is on the low end of strains that can be generated and 1800/s is on the high end. Similarly, the plastic behavior in a variety of thermal environments needs to be observed. The range of temperatures are room temperature (23°C) and then $\frac{1}{6}$, $\frac{1}{3}$, and $\frac{1}{2}$ of the melting temperature based on English units. In SI units, they are 223°C, 466°C, and 707°C respectively.

In this section, the experimental equipment was reviewed and an overview of how split-Hopkinson bar tests work was given. The raw engineering stress-strain curves are available in Appendix B. Next the results of the experiments and their conversion from engineering stress-strain to true stress-strain will be covered.

3.3 Experimental Results

Data Reduction.

For brittle materials, it is relatively simple to convert engineering stress and strain to true stress and strain using Equations 38 and 39:

$$\sigma_{true} = \sigma_{eng}(1 + \epsilon_{eng}) \quad (38)$$

$$\epsilon_{true} = \ln(1 + \epsilon_{eng}) \quad (39)$$

where σ_{eng} and ϵ_{eng} are engineering stress and strain.

These equations are only reliable until the cross-sectional area begins to shrink during the necking process of failure initiation just beyond the ultimate tensile stress [60]. This makes Equations 38 and 39 ideal for brittle materials which exhibit little to no necking. For ductile materials that exhibit significant necking, the only way to obtain true stress-strain curves is to use Equations 40 and 41, which require having continuous measurement of the changing cross-sectional area.

$$\sigma_{true} = \sigma_{eng} \frac{A_o}{A_i} \quad (40)$$

$$\epsilon_{true} = \ln \frac{A_o}{A_i} \quad (41)$$

where A_i is the current area and A_o is the original starting area.

The changing area can be measured using high speed cameras or digital image

correlation. Since our specimens in the split-Hopkinson bar device were enclosed in a metal collar during test runs, neither of these options were viable. Sasso has presented an area change approximation method correcting for necking present in high strain rate tension Hopkinson bar experiments [61]. This was applied to the engineering stress and strain to obtain true stress and strain data for the Split-Hopkinson data. The correction used was:

$$\left(\frac{A_0}{A}\right)_{linear} = 4 \left(\sqrt{\frac{3(3 - \epsilon_{eng})}{1 + \epsilon_{eng}}} - 1 \right)^{-2} \quad (42)$$

By approximating the changing area and assuming the radial and tangential stresses are equal due to isotropy, the stress obtained by substituting Equation 42 in Equation 40 results in the measurement of average axial stress. It is only the axial stress because it is assumed that the area reduction is constant and does not take any curvature into account. The Bridgman correction factor, seen in equation 43, provides a method of estimating the additional contributions from the progressing curvature in the sample as failure is taking place [62].

$$\sigma_{eqv} = \frac{\sigma_{axial}}{(1 + 2R/a) \ln(a/2R)} \quad (43)$$

The Bridgman correction factor is regularly used to account for the additional hoop stresses generated from necking. It is a geometry-based measurement which again requires continuous measurement of the necking area dimensions during failure, or straining a sample beyond necking but not to failure to obtain curvature measurements [62] [63]. For steels, there is a popular function that approximates these measurements and it is used in this work shown in Equations 44 and 45 [60] [62].

$$B = 0.0684x^3 + 0.0461x^2 - 0.205x + 0.825 \quad (44)$$

$$\sigma_B = B\sigma_{true} \quad (45)$$

where $x = \log_{10} \epsilon_{true}$ and is true for valid for strain values $0.12 \leq \epsilon_{true} \leq 3$. Correction is not required for strains below 0.12. These corrections will allow an axial curve to represent the overall response of a 3D effect.

True Stress-Strain Curves.

The following figures show the experimental curves obtained from the experiments. Each curve is an average of the stress-strain results for three runs at the indicated experimental condition. Figure 15 shows the averaged quasistatic and 0.5/s data, performed on the MTS servo-hydraulic test stand at room temperature. The results in Figures 16-18 were carried out on the SHB test stand at strain rates ranging from 500/s to 1800/s, and temperatures ranging from room temperature to 707°C. Figure 16 shows the 500/s curves, Figure 17 shows the 1000/s curves, and Figure 18 shows the 1800/s curves.

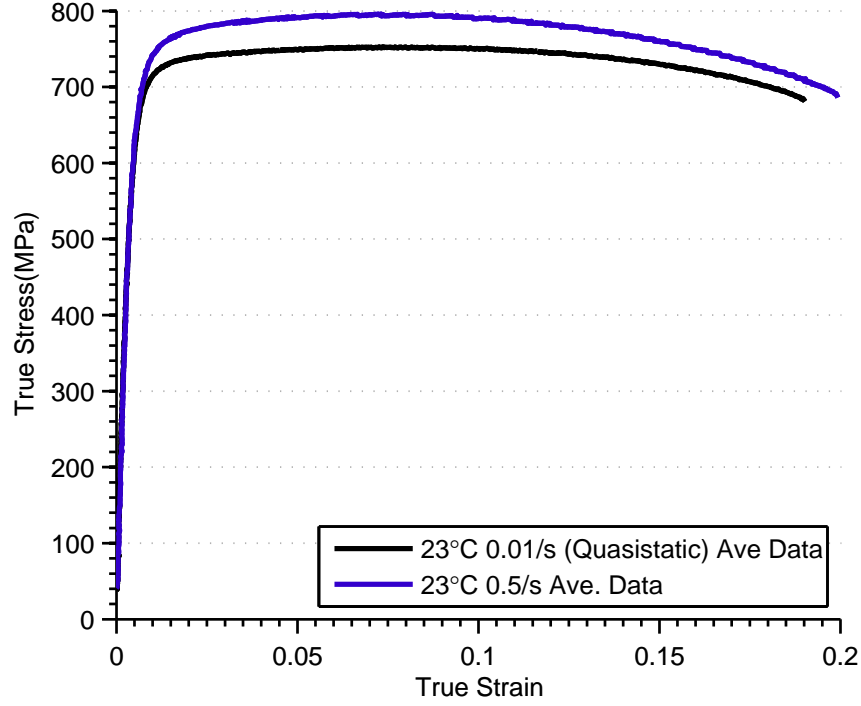


Figure 15. Averaged experimental data for the 0.01/s (quasistatic) and 0.5/s (reference) strain rates.

In the quasistatic curves shown in Figure 15, the flow stress rises with the increased strain rate, and the failure strain also increase slightly, leading to an overall increase in toughness between the two. For these curves, the basic correction in Equations 38 and 39 are used to convert the curves from engineering to true stress and strain due to the low strain rate and lack of necking observed in the samples. There is a small amount of strain softening that can be seen in both curves as the stress and strain decreases beyond the ultimate tensile strength instead of increasing consistently.

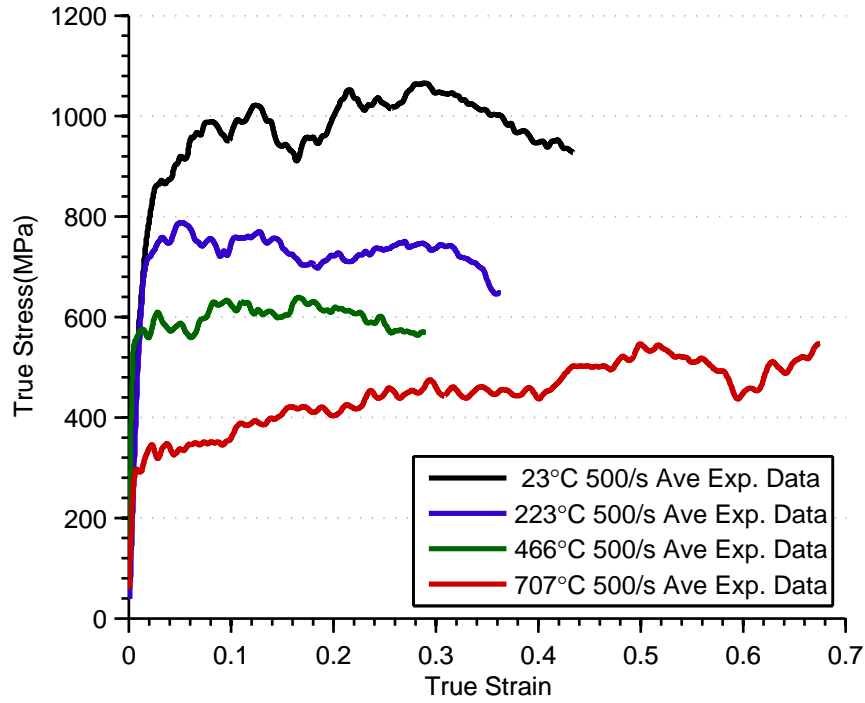


Figure 16. Averaged experimental data for the 500/s strain rates

In the 500/s experimental data in Figure 16, there is an unusual trend that continues throughout all of the results, where the fracture strain decreases with increasing temperature up until the highest temperature. There is some strain softening that becomes more pronounced with increasing temperature, until the highest temperature where there actually appears to be strain hardening more typically expected in steels.

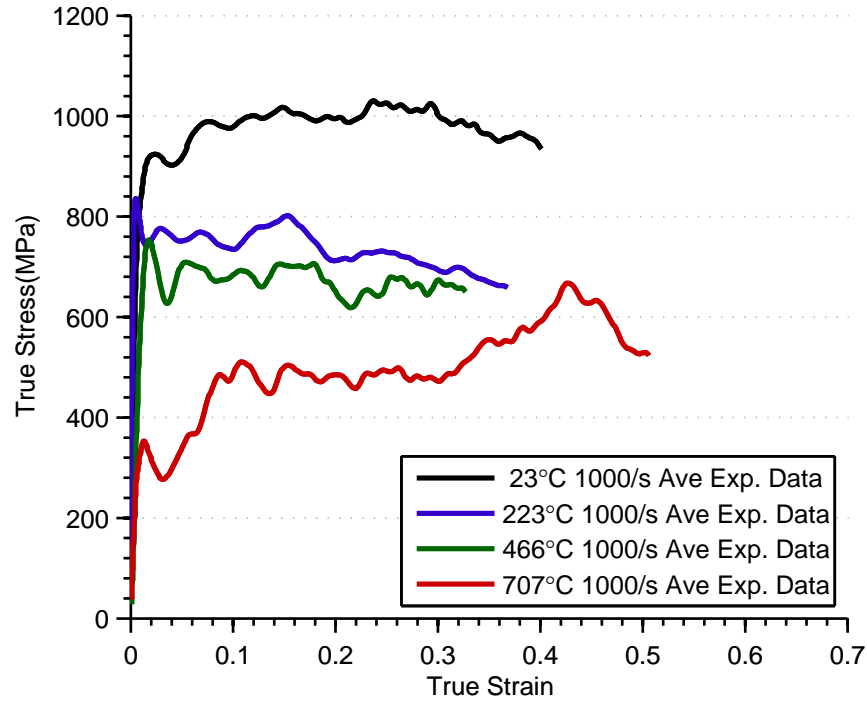


Figure 17. Averaged experimental data for the 1000/s strain rates

The 1000/s results again show unusual failure strain behavior. The increased strain rate reduces the yield strain for the room temperature and 223°C experiments, and the thermal softening appears to be more pronounced for the 223°C and 466°C curves. The difference in flow stress between the two is decreasing. Conversely, the 707°C results have a more pronounced increase in flow stress with increasing strain.

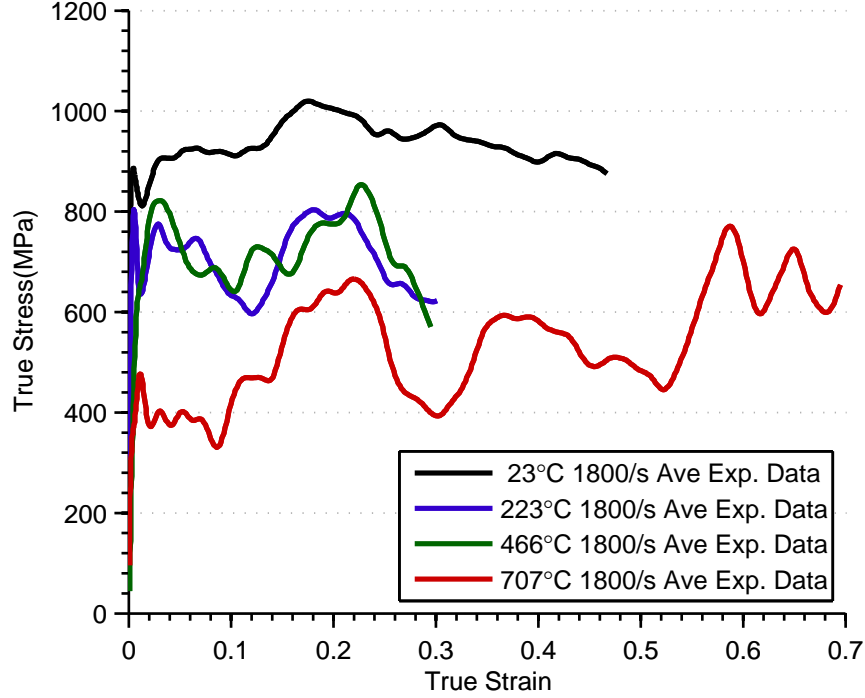


Figure 18. Averaged experimental data for the 1800/s strain rates

The 1800/s curves still keep with the same unusual failure strain pattern as with the 500/s and 1000/s curves. In general, the thermal data is showing more noise than the previous strain rates. The effects from thermal softening are minimal, and again the 707°C shows no signs of it. The 223°C and 466°C curves are overlapping.

Overall for the dynamic curves, we can note a general trend of strain softening for the first three temperature regimes, and then for the 707°C material there is strain hardening. Presumably, the strain softening is not a result of necking since the Bridgman correction and area reduction approximation has already been applied during the true stress-strain conversion. The increasing flow stress for the 707°C runs might be an indication that dynamic recrystallization has more of an effect at this temperature. Dynamic recrystallization is a process where due to increased temperatures and strain rates, new grains nucleate in the microstructure and strengthen the material by lowering the general grain size. More on this topic will be discussed in subsequent

chapters.

One very apparent observation one can make is that the experiments run on the servo-hydraulic test stand (0.01/s and 0.5/s) are much smoother in comparison to the the higher strain rate experiments run on the split-Hopkinson bar test stand. High strain rate experiments as a general rule are subject to an affect known as ringing. As defined in Yang's study: "Ringing artifacts, which are a consequence of the inertial response of the load frame, are spurious oscillations that can obscure the desired material response (i.e. load vs. time or load vs. displacement) from which flow data are derived." [64]. There are studies going on trying to research how to reduce these effects. Some approaches as outlined in Xioa's conference proceedings include, IISI guides recommended the following: "To reduce the stress oscillation, in addition to a careful design of the testing machine, clamping system and specimen, the proper selection of the load measurement device is critical." [65] [66]. It is believed that the the test stand set-up, in addition to other possible contributing factors (surface roughness in turned gage section) are the source of these oscillations. While they clearly make analysis more difficult, they are typical of high strain rate dynamic tests.

This chapter has covered the experimental program carried out at UDRI and shown the results gathered. In the next chapter, the results will be used to calculate the Johnson-Cook model material parameters. The raw experimental data will be available as an electronic attachment.

IV. Johnson-Cook Model Fitting

4.1 Coefficient Determination

Johnson-Cook Strength Coefficient Determination.

Determining the Johnson-Cook strength coefficients is a fairly straight-forward process of isolating a portion of the strength equation through normalization, plotting it against the experimental true stress-strain data (recall, the averaged result of three experimental runs for each curve), and performing a curve fit. The Johnson-Cook strength equation is again stated:

$$\hat{\sigma}_y = (A + B\epsilon_p^n)(1 + C \ln \frac{\dot{\epsilon}_p}{\dot{\epsilon}_o})(1 - T^{*m}) \quad (46)$$

The static stress terms, yield stress (A) and isothermal strain (B and n), are found using data from the averaged 0.5/s reference strain rate ($\dot{\epsilon}_o$) tensile experiments. A is determined by the 0.2% offset method. First, the elastic modulus (E) is determined by calculating the slope of the linear portion of the stress-strain curve, and then the slope is offset by 0.2%. The intersection of the experimental curve and the 0.2% offset line is the yield stress of the material. This is shown in Figure 19. The curve is a typical one for a low-alloy carbon steel, and we are able to determine a yield stress of 673 MPa and an elastic modulus of 160 GPa.

B and n are found by plotting the logarithmic reference 0.5/s plastic stress and strain, isolated using Equations 47 and 48.

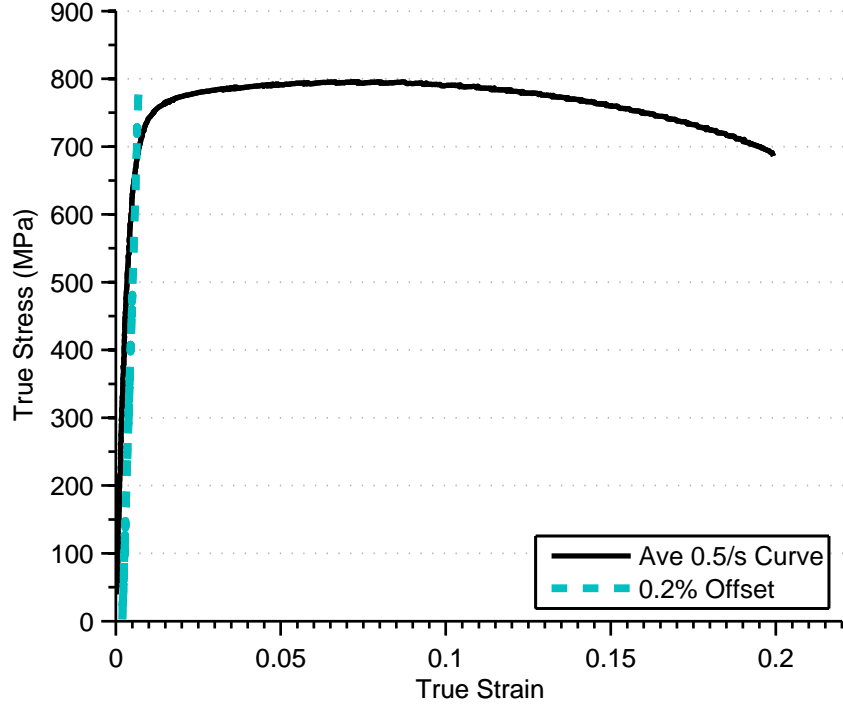


Figure 19. 0.2% offset fit for treated 4130 using averaged 0.5/s tension data. The calculated Young's Modulus and yield stress are 160,000 MPa and 673 MPa respectively

$$\sigma_p = \sigma_t - A \quad (47)$$

$$\epsilon_p = \epsilon_t - \frac{A}{E} \quad (48)$$

where σ_t is true stress. The logarithmic plastic stress is plotted against the logarithmic plastic strain while the curve exhibits hardening. The data is then fit linearly to obtain the slope (n) and the intercept, which is used to find the B coefficient by raising 10 to the power of the intercept. This is shown in Figure 20. The region of plastic hardening was small, and it was found that this fitting portion was subjective to how much data was included or excluded. B was calculated to be 190 MPa and n , 0.1538.

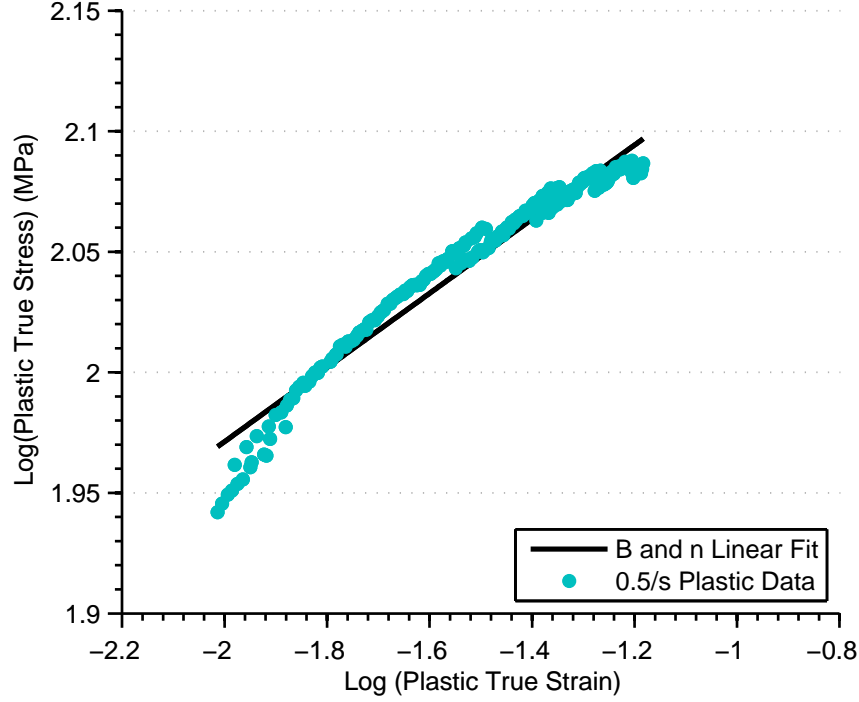


Figure 20. Curve fit for Johnson Cook strain rate coefficients B and n of treated 4130 steel. The plastic portion of the quasistatic curve that exhibits strain hardening is isolated and fit linearly. B is 10 raised to the power of the intercept, found here to be 190 MPa, and n is the slope of the line, 0.1538.

To continue, a dynamic reference strain (ϵ_{ref}) must be defined. It is used as a reference point for comparing dynamic stress values when calculating C and m . The value is chosen from the reference data, and must be large enough that the stress is in the flow region, but not so large as to be greater than the ultimate tensile strength of the material where failure or necking has begun to occur. In other studies, the value has ranged between 5% and 10% [3] [43]. For this study, the reference strain is found by plotting the experimental 0.5/s plastic stress-strain curve against the solved $\sigma = (A + B\epsilon_p^n)$ curve. The point when the two curves meet is taken as the reference strain, found to be 4% of the total strain for our data, as seen below in Figure 21.

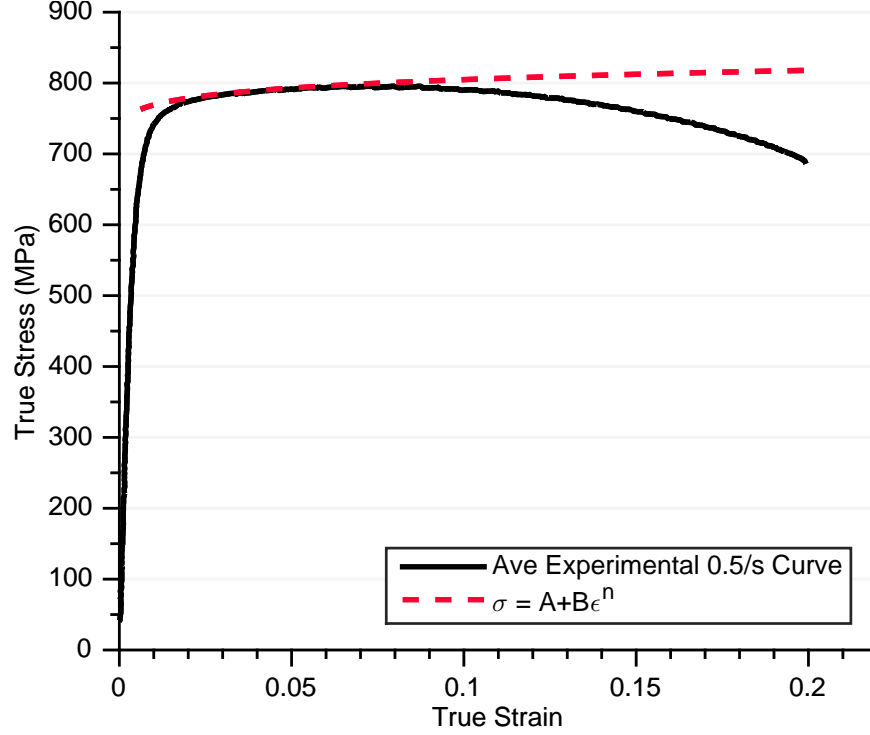


Figure 21. 0.5/s average reference stress-strain curve plotted against the solved $\sigma = (A + B\epsilon_p^n)$ curve. The two curves come together between 0.03 and 0.04 of the total strain. The reference strain 0.04 was chosen as it produced the best fitting results.

Room temperature strain rates of 0.01/s, 0.5/s, 500/s, 1000/s, and 1800/s tensile data is used to calculate the strain rate coefficient C. To isolate the strain rate effects, the flow equation is normalized against the static stress and thermal stresses:

$$\frac{\hat{\sigma}_y}{(A + B\epsilon_{ref}^n)(1 - T^{*m})} = (1 + C \ln \frac{\dot{\epsilon}_p}{\dot{\epsilon}_o}) \quad (49)$$

Since only room temperature data is used, the thermal term becomes one and thus cancels.

$$\frac{\hat{\sigma}_y}{(A + B\epsilon_{ref}^n)} = (1 + C \ln \frac{\dot{\epsilon}_p}{\dot{\epsilon}_o}) \quad (50)$$

A, B, and n are the constants solved for previously, $\dot{\epsilon}_o$ is the reference strain rate 0.5/s, and ϵ_{ref} is the dynamic reference strain 0.04. Thus on the left hand side of Equation 50 we have the normalized dynamic stress, and on the right hand side we have the

strain rate effects. The $\hat{\sigma}_y$ term is the dynamic stress found from the experimental true stress-strain curve (which recall, is the average of three experimental runs) at 0.04 strain.

The normalized stresses for each strain rate are plotted against the natural log of their strain rates producing a plot that can be linearly fitted to obtain the value for C, found to be 0.017. This is shown in Figure 22.

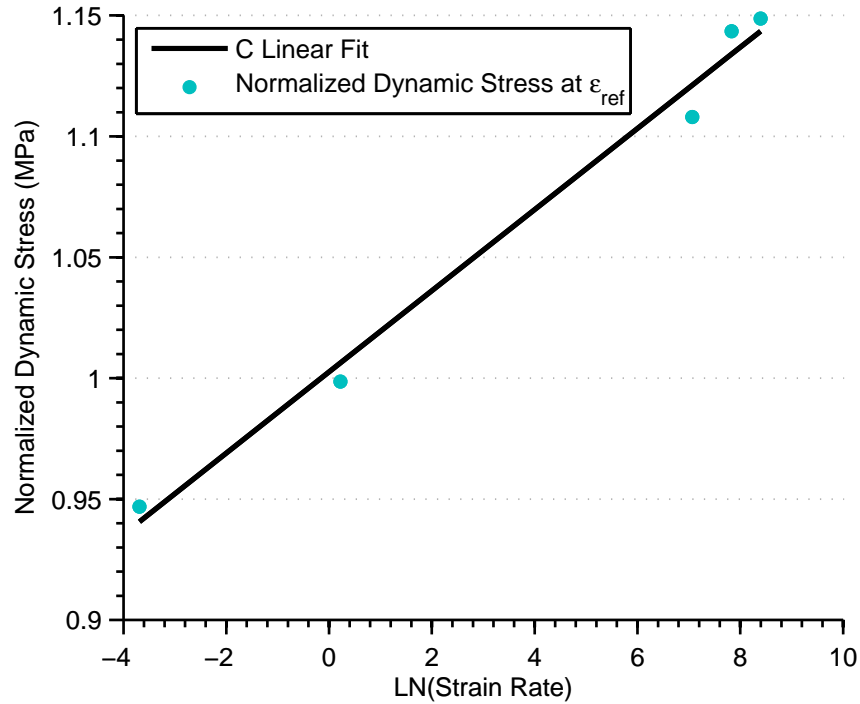


Figure 22. Curve fit for the strain rate coefficient Johnson Cook C for treated 4130 steel. The stress at a reference strain (in this study, 0.04) is normalized against the 0.5/s stress and plotted at the natural log of each room temperature strain rate (0.01/s, 0.5/s, 500/s, 1000/s, and 1800/s). The points are linearly fit, and the slope is the value of C, 0.017.

The fit shows good correlation with other Johnson-Cook fits for metals, and indicates that the 4130 steel flow stress does have a response dependence on strain rate [3] [43].

When fitting the data for the thermal coefficient 'm', the low strain rate data is excluded (0.01/s, 0.5/s) as is any room temperature data. The 500/s, 1000/s, and

1800/s strain-stress curves for 223°C, 466°C, and 707°C temperatures (approximately 1/6, 1/3, and 1/2 the melting temperature) are all used. As before, the dynamic stress obtained at the reference strain is normalized to isolate the thermal contributions to the curve. This is done by dividing the experimental stress at the reference strain by the room temperature stress portions as seen in Equation 51.

$$\frac{\hat{\sigma}_y}{(A + B\epsilon_{ref}^n)(1 + C \ln \frac{\dot{\epsilon}_p}{\dot{\epsilon}_o})} = (1 - T^{*m}) \quad (51)$$

The left hand side of Equation 51 is the normalized thermal stress, and the right hand side is the predicted thermal contribution. The logarithms of the normalized stress and the homologous temperature are plotted against each other, and the slope of the linear fit of the data represents m as in Figure 23.

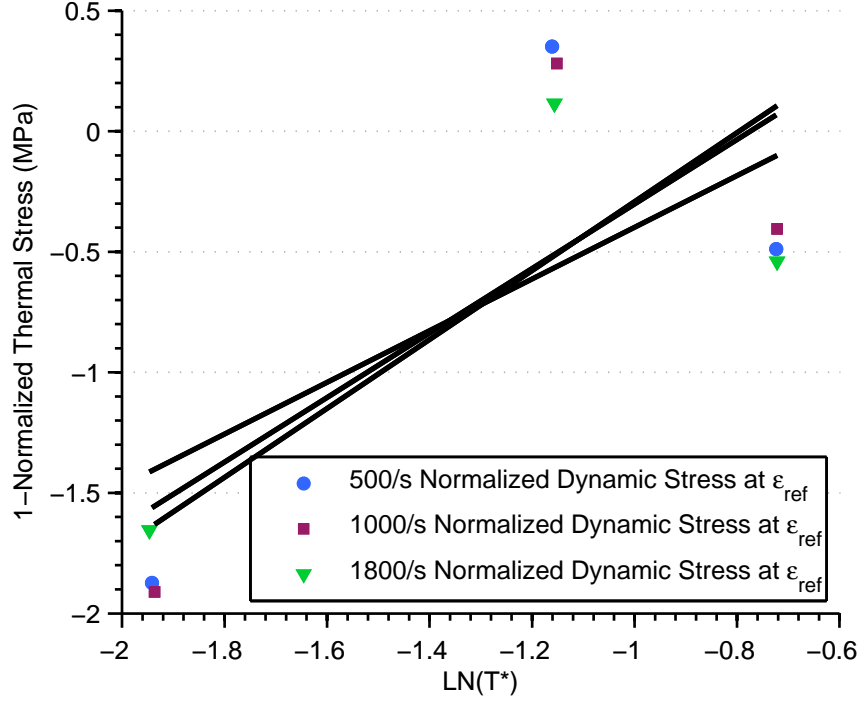


Figure 23. Curve fitting for the Johnson Cook thermal coefficient m of treated 4130 steel. The stress at the same reference strain is found for each strain rate (500/s, 1000/s, 1800/s) and at each temperature (223°C, 466°C, 707°C) and normalized against their respective room temperature counterparts. Then the normalized strains are subtracted from one and plotted against the natural log of the homologous temperature and fit linearly for each of the strain rate resulting in three separate linear fits. Each slope is an m value, and in this study the final chosen value of m is 1.07 as it gave the best fit results in simulations.

Each strain rate is plotted and fitted individually, resulting in a spread of m values. So, there is an m value associated with the 500/s data, another for the 1000/s data, and another for the 1800/s data. The three different m values are tested in a finite element simulation to see how they affect the flow stress (the model will be further explained in Section 4.2). The final value of m is chosen based on which one gives the best analytical results when testing the coefficients in a finite element simulation and comparing them to the experimental data. Unlike the previous fits, the data does not line up linearly indicating the thermal contributions might not be correctly represented with this fitting.

Damage Coefficients.

A similar process is undertaken to calculate the Johnson-Cook damage coefficients.

Recall the damage equation:

$$\epsilon_f = [D_1 + D_2 e^{-D_3 Q}] [1 + D_4 \ln \frac{\dot{\epsilon}_p}{\dot{\epsilon}_0}] [1 + D_5 T^*] \quad (52)$$

where ϵ_f is the equivalent plastic strain at fracture, Q is the stress triaxiality factor, ϵ_0 is the reference strain rate (0.5/sec), $\dot{\epsilon}_p$ is the plastic strain rate, T^* is the homologous temperature, and D_1 - D_5 are the damage coefficients.

The first step is calculating the triaxiality-dependent factors D_1 – D_3 . The notched specimens' geometry and failure strains are used to calculate initial triaxiality and coefficient values using an equation developed by Bridgman and used by Hopperstad and Borvik:

$$Q_0 = \frac{1}{3} + \ln \left(1 + \frac{a_0}{2R_0} \right) \quad (53)$$

where a_0 is radius of the initial cross-sectional area of the notched specimen and R_0 is the radius of the specimen notch [67] [68] [69].

The equation uses the same $(\frac{a}{R})$ ratio developed by Bridgman for smooth necking specimens, but here it is applied to predict plastic conditions of pre-strained, notched specimens.

From Borvik et al: It is noted that Bridgman's analysis was developed for a necked smooth specimen, but has been used as an approximation to the pre-notched specimens after having reached fully plastic condition, where the cross-section of the specimen has exceeded the yield stress of the material [69] [47]. It was further assumed that the stress triaxiality is constant during straining, and that the plastic strain is constant over the cross section of the neck.

The initial stress triaxiality σ_0^* in the center of the notch is obtained by inserting

the initial radius of the minimum cross-section a_0 and the initial notch radius R_0 into Eq. (9). Mackenzie et al. (1977) investigated ductile failure in notched high strength steel specimens with original ratios a/R between 0.6 and 3.4. They measured the ratio a/R before testing and after fracture initiation, and found that the change in a/R resulted in an under-estimation of the calculated stress triaxiality for the largest notch radius by about 20% when the strain was large. However, in most of their tests the change in a/R and its effect on the calculated stress triaxiality were much less. The initial stress triaxiality was also used for the smooth specimen, even if it is well established that the stress triaxiality will increase strongly after necking owing to the introduction of hydrostatic tension stresses in the neck. The adopted approach should, however, lead to conservative estimates on the ductility [47].

There was some concern about the variation in the notch radius causing issues with this relationship however. To verify this relationship, an ABAQUS model of the notched specimen was created to do a check. Theoretically, the measured trivialities should match with those predicted in the simulations.

The finite element model created was an axisymmetric shell, built with three-node and four-node solid axisymmetric elements that do not support torsional loads (coded CAX3 and CAX4R in ABAQUS, respectively). The 0.48mm model has 343 CAX3 and CAX4R elements and 295 nodes, the 0.87mm model uses 221 CAX3 and CAX4R elements and has a total of 270 nodes, and the 2.52mm model uses 206 CAX3 and CAX4R elements and has a total of 261 nodes. The material was elastic 4130 steel with a density of 7.85 g/mm³, Youngs Modulus of 160 MPa, and a Poissons ratio of 0.27 [54]. The boundary conditions applied were an x-symmetric condition along the center axis, allowing only a half of the model to be built and then the other half to be symmetrically simulated, and x-displacement, y-displacement, and z-rotation are restrained along the base of the specimen. A 20,000N load is applied to the free end,

simulating the process of a tension test. Triaxiality is measured where its value is maximized: at the center of the specimen.

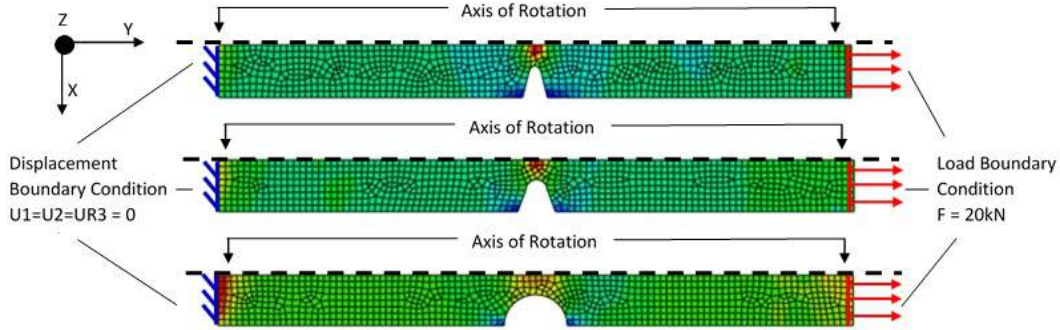


Figure 24. Finite element model used to verify the triaxiality using Equation 53. Notch sizes from top to bottom are 0.38mm, 0.79mm, and 2.38mm. For axisymmetric simulations usually cylindrical coordinate system is used, but ABAQUS is converting it to a Cartesian coordinate system.

The triaxialities calculated from Equation 53 and those obtained from the simulation are compared in Table 4.

Table 4. Comparison of notch triaxialities predicted by finite element modeling and calculated using equation 16

Average Notch Radius	Average Area	Calculated, Equation53	ABAQUS Simulation
0.48mm \pm 0.02	8.34 mm ² \pm 0.29	1.33 \pm 0.31	1.41
0.87mm \pm 0.03	7.62 mm ² \pm 0.28	0.96 \pm 0.31	1.20
2.52mm \pm 0.03	7.81 mm ² \pm 0.29	0.61 \pm 0.32	0.62

Variations in the machining process resulted in a spread of the measured values. The standard deviations of the measurements are used to represent uncertainty. The simulated results are within the uncertainty of the calculated triaxiality, so it is not believed the surface roughness will negatively affect the results.

Recall, the triaxiality value is always fluctuating throughout deformation. But for a mathematical simplification for the purpose of this coefficient fitting, one can

assume that during straining the hydrostatic stress (σ_m) and equivalent stress ($\hat{\sigma}$) change at the same rate and the plastic strain is constant across the necking cross section [47] [67]. This creates a constant triaxiality value. In an investigation by Mackenzie et al., it was found that using the initial triaxiality as the constant value results in an under-prediction of stress triaxiality in large notches by as much as 20% for large a/R ratios, but the difference decreases as the notch size decreases [70]. Thus, it is shown to provide a good conservative value for ductility measurement [69].

The initial triaxiality results from Equation 53 and failure strains (the last recorded strain of the true stress-strain curve before the curve drops dramatically, indicating failure) of the notched specimens are used to calculate the first coefficients, D_1 - D_3 . The failure strains from each run of the tension tests of the notched specimens are plotted against the triaxialities. The curve is fitted in MATLAB using the Levenberg-Marquardt numerical solving method, a standard method for solving non-linear least squares problems [71].

For those unfamiliar with the algorithm, the Levenberg-Marquardt method fits a set of data points to a parameterized function by minimizing the sum of squares of the errors between the data points and the function [71]. It is one of the most popular optimization method used for solving nonlinear problems, and combines two different solving algorithms: the method of steepest descent and the Gauss-Newton method. The Method of Steepest Descent (or Gradient Descent Method) finds a minimum moving point to point by calculating a slope gradient until the value is within a small amount of error. However, depending on the particular function, this can be a time-consuming process hence the method has a poor rate of convergence. The Gauss-Newton Method assumes the function is locally quadratic, and minimizes the sum of squares errors by finding the minimum of the quadratic. As the errors become

smaller, the algorithm switches from behaving like the steepest descent method to the Gauss-Newton method [71]. By combining the two methods, the rate of convergence and the overall fit is improved.

The method is used to fit the equation $D_1 + D_2e^{-D_3Q}$ resulting $D_1 - D_3$ fit is seen in Figure 25. The fit looks good, and the coefficient value compares well to other similar metals.

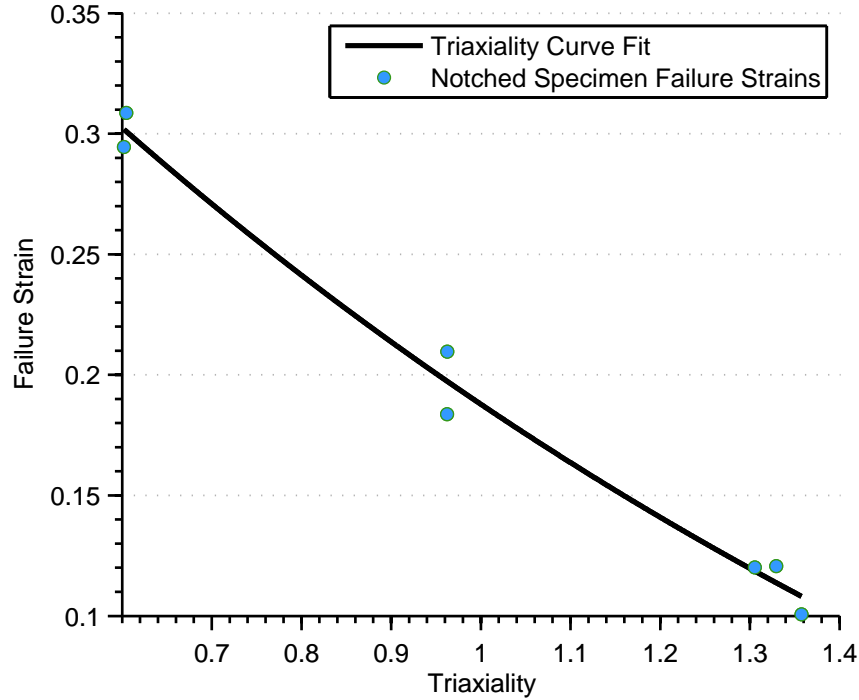


Figure 25. Curve fit for the Johnson-Cook damage ductile metal failure void coefficients D_1 , D_2 , and D_3 for treated 4130 steel. The failure strains of the triaxiality specimens are plotted against their calculated triaxiality Equation 53. These points are fit using the Levenberg-Marquardt algorithm, and found to be -0.1895, 0.7324, and 0.6633

For D_4 and D_5 , the solving process mirrors that of C and m in that a reference point is used, though rather than a dynamic reference strain, it is a triaxiality value [43]. This triaxiality is selected from the range of triaxialities used in the notch fitting (1.33, 0.96, and 0.61). Similar to the m fitting, all values were tried in a finite element simulation (described in section 4.2) when fitting the next two coefficients, D_4 and D_5 . The reference triaxiality is chosen based on which combinations of D_4 and D_5

results produced the best fit when compared to the experimental data. In this study it was found to be the largest triaxiality: 1.33.

D_4 is found by negating the thermal portion of the damage equation by only analyzing room temperature fractures and by isolating the strain rate portion of the curve by normalizing the dynamic fracture to the effects of void formation. The resulting normalized equation is seen in Equation 54.

$$\frac{\epsilon_f}{[D_1 + D_2 e^{-D_3 Q_{ref}}]} = [1 + D_4 \ln \frac{\dot{\epsilon}_p}{\dot{\epsilon}_0}] \quad (54)$$

Thus, the left hand side of the equation is the normalized failure strain and the right hand side is the strain contributions from strain rate effects. D_1 , D_2 , and D_3 are the previously solved values, ϵ_f is the average fracture strain of three runs at each experimental condition, and $\dot{\epsilon}_0$ is the reference strain rate 0.5/s. Q is the selected reference triaxiality. Three values for D_4 result from trying each of the three different reference triaxialities and are shown in Figure 26.

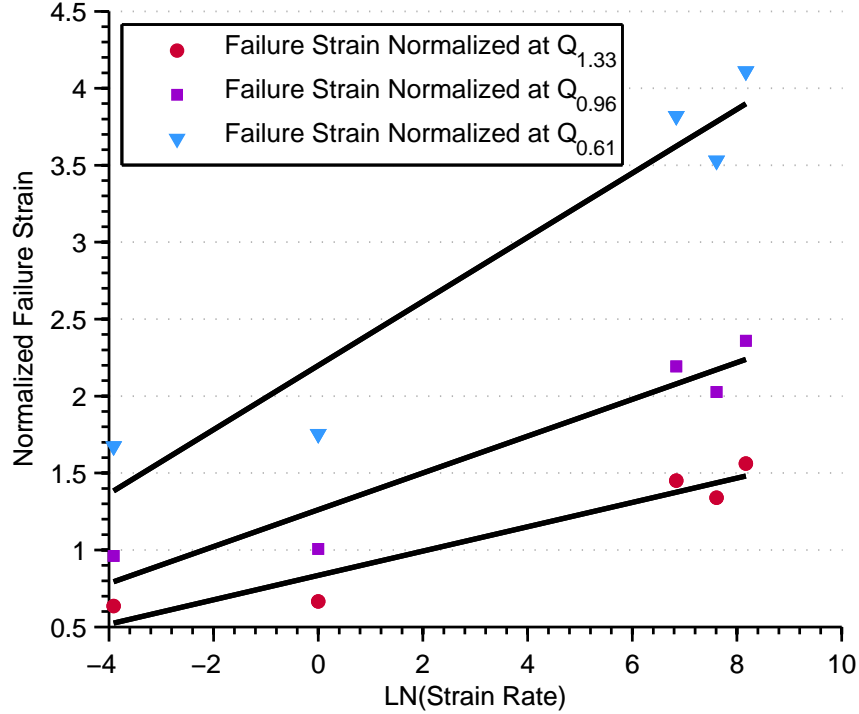


Figure 26. The failure strains of treated 4130 steel are found at each room temperature strain rate (0.01/s, 0.5/s, 500/s, 1000/s, 1800/s) and normalized against the triaxiality data at a calibrated reference triaxiality (1.33). These are plotted against the natural log of each of the strain rates and fit linearly. There are three different fits for each of the three triaxialities that are being calibrated. The slope of the line is D_4 , and the calibrated value is 0.0291.

The value produced when the reference triaxiality was 1.33 produced the best results, and that value was 0.0291. Figure 26's trend is along the lines of what is seen in other documentation, however the slope for the smaller triaxiality values are higher than other metals' reported values [43].

Since D_1 - D_4 are all solved for, all that needs to be done is normalizing the equation against the other effects as is shown in Equation 55.

$$\frac{\epsilon_f}{[D_1 + D_2 e^{-D_3 Q_{ref}}][1 + D_4 \ln \frac{\dot{\epsilon}_p}{\dot{\epsilon}_0}]} = [1 + D_5 T^*] \quad (55)$$

D_5 is solved by normalizing the average of the failure strains for each of the high strain rate (500/s, 1000/s, 1800/s) and high temperature runs (223°C, 466°C, 707°C)

and plotting them against the homologous temperatures. The linear fit is taken to acquire a slope with the value of D_5 . Thus, the left hand side of Equation 55 is the normalized failure strain, and the right hand side are the contributions to the failure strain from thermal conditions. Again, there are three different slopes produced by varying the triaxiality, and are shown in Figure 27.

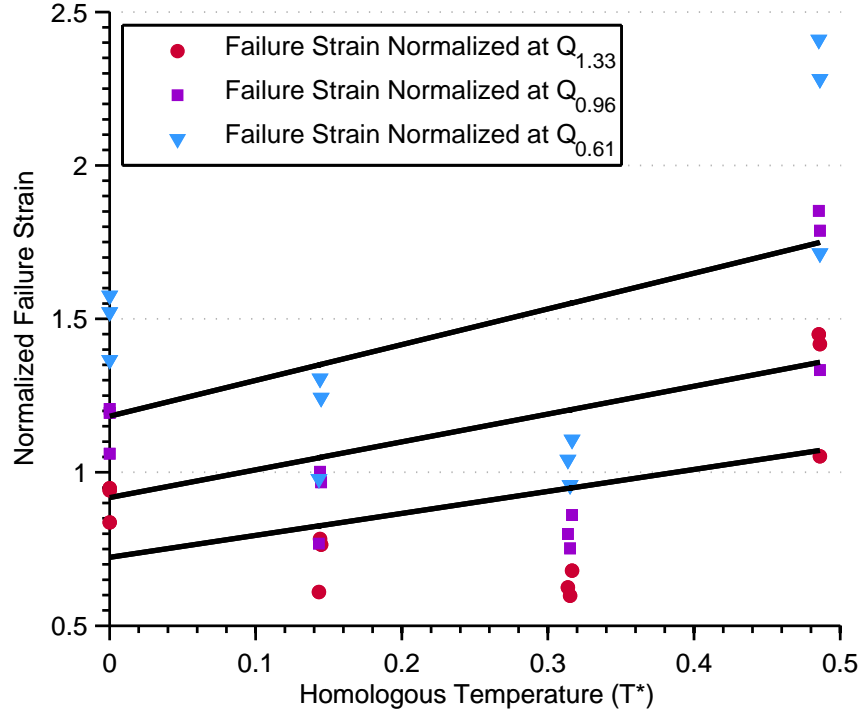


Figure 27. The failure strains of treated 4130 steel are found at each strain rate (500/s, 1000/s, 1800/s) for each temperature (23°C, 223°C, 466°C, 707°C) and normalized against the triaxiality data at the chosen reference triaxiality. These are plotted against the correlating homologous temperature and fit linearly. As in the thermal m fitting, each strain rate is plotted separately to allow for calibration. The slope of the line is D_5 , and the calibrated value is 0.7162

The value of D_5 that produced the best results occurred when $Q = 1.33$, which was 0.7162. Figure 27 is a departure from what is expected. While it is not unusual for increasing strain rates to cause earlier fracture strains, typically the increase of temperature would induce more ductile behavior and thus larger fracture strains. The decrease in failure strain with increasing temperature until the final highest temperature is odd. However the value of D_5 does fall within other reported values,

despite the linear fit not matching the data well. This is an indication that the damage criterion is not fully capturing the thermal dynamic behavior of the material as formulated.

The above discussion is associated with the method incorporated in experimentally developing the parameters associated with Johnson-Cook relations. Subsequently, a discussion is to be presented which will tie the micromechanics into these parameters, this aspect of the research is a major contribution to evaluating the effectiveness of the use of Johnson-Cook in representing heat-treated 4130 steel in a high strain environment.

4.2 Finite Element Modeling

A finite element model was created in ABAQUS to validate the calculated coefficients [72]. ABAQUS explicit mode is used as opposed to implicit mode. Explicit mode is geared for involved wave mechanics problems, which is ideal for a high strain rate deformation problem. A flow chart for the solution algorithm ABAQUS uses in solving non-linear viscoelastic problems incorporating the Johnson-Cook model will be shown in Appendix C. The incremental time step used was 1e-6 seconds to ensure enough data points were collected to form a smooth true stress-effective plastic strain curve. Johnson-Cook constitutive and damage models are used to model the plastic stress and the accumulating damage, and 90% of the plastic strain energy is converted into heat [73]. Inputs for the model are the solved Johnson-Cook parameters, the inelastic heat fraction, Poisson's ratio, the elastic modulus, and the specific heat (works in tandem with the inelastic heat fraction to convert strain energy into heat). The material properties and Johnson-Cook parameters for the model can be found in Tables 5 and 6.

Table 5. Mechanical, elastic, and thermal material properties of 4130 steel used for ABAQUS finite element simulation

Property	Symbol	Value
Density	ρ	7850 kg/m ³
Poisson's Ratio	ν	0.29
Elastic Modulus	E	160 GPa
Specific Heat	c_p	523 J/kg-°C
Inelastic Heat Fraction	β	0.9

Table 6. Summary of Johnson-Cook Strength and Damage Coefficients calculated for treated 4130 steel.

Strength Coefficients		Damage Coefficients	
A	673 MPa	D_1	-0.1895
B	190 MPa	D_2	0.7324
n	0.1538	D_3	0.6633
C	0.017	D_4	0.0291
m	1.07	D_5	0.7162

The model is an axisymmetric representation of the sub-size E8 dogbone specimen with a clamped boundary condition on one end and a positive displacement boundary condition on the other, resulting in the creation of a tensile stress within the gage section, as seen in Figure 31. The dimensions match those of the sub-size E8 specimens used, with minor simplifications (omitting the threads and approximating the radius of curvature as a straight line). It is composed of 405 quadrilateral linear axisymmetric elements (CAX4R in ABAQUS notation) with 492 nodes. A predefined temperature field is used to apply the different temperature states. The displacement boundary

condition is applied using a tabular amplitude based on target strain rate calculations. Strain rate can be expressed as:

$$\dot{\epsilon} = \frac{d\epsilon}{dt} \quad (56)$$

where a change in strain $d\epsilon$ is occurring over a time step dt . The strain expanded is:

$$\epsilon = \frac{L - L_0}{L_0} \quad (57)$$

where L is the current length of the gage section and L_0 is the original gage length. By substituting Equation 57 and a time step into Equation 56, one can solve for a change in displacement in the gage section.

$$L - L_0 = \dot{\epsilon} L_0 dt \quad (58)$$

A tabular time-amplitude table was created by solving the equation for 1000/s for a series of increasing time steps. By adjusting the value of the U2 displacement, one could scale the strain rate to a different strain rate (0.5 = 500/s, 1 = 1000/s, 1.8 = 1800/s). For example, if one wanted to calculate the changing length required for a time step of $1E-6$ at a strain rate of 500/s, the calculation would follow:

$$\begin{aligned} L - L_0 &= (500/s)(8.89mm)(1E-6s) \\ L - L_0 &= 4.45\mu m \end{aligned} \quad (59)$$

Thus to produce a strain rate of 500/s in our gage specimen, the change of length must be 4.45 microns.

For each time step in the simulation, the equations of motion (displacement, velocity, and acceleration), strain, strain rate, flow stress, and damage are all calculated.

The progression of how ABAQUS applies damage in a simulation is shown in Figure 28.

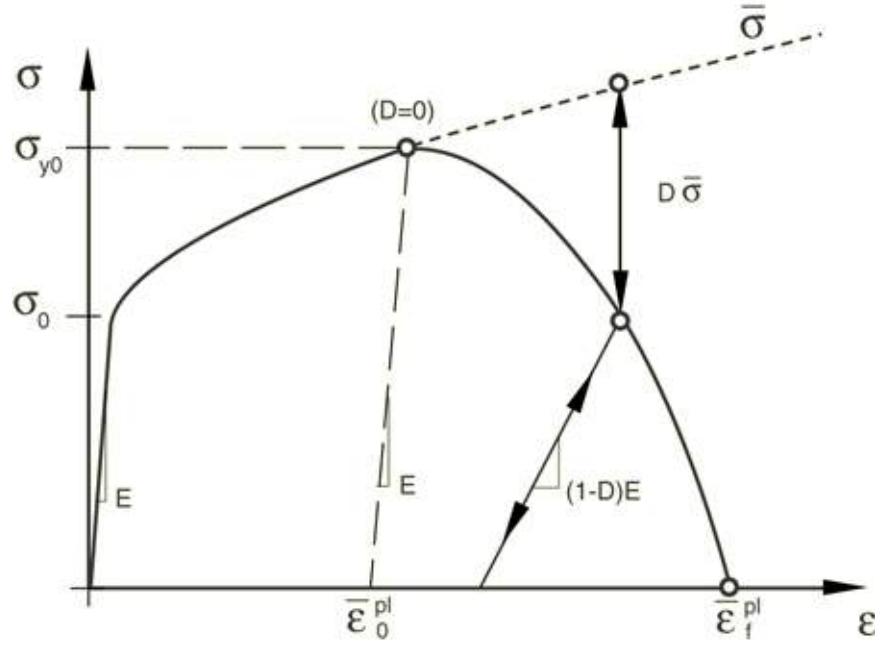


Figure 28. Stress-Strain curve showing ABAQUS's process for applying progressive damage [73]

σ_0 is the yield stress, σ_{y0} and $\bar{\epsilon}_0^{pl}$ are the yield stress and the equivalent plastic strain at the onset of damage, $\bar{\sigma}$ is the flow stress, D is the overall accumulating damage variable, $\bar{\epsilon}_f^{pl}$ is the equivalent plastic strain at failure. Once damage begins to accumulate, the elasticity of the response is gradually reduced in the form of $(1 - D)E$ [73]. This allows for the simulation to be able to take necking and strain softening into account in addition to three-dimensional stress effects as failure progresses. In Figure 29, the output from a simulation of a 1000/s strain rate run at 223°C of the damage criterion, vonMises stress, and equivalent plastic strain is shown for reference.

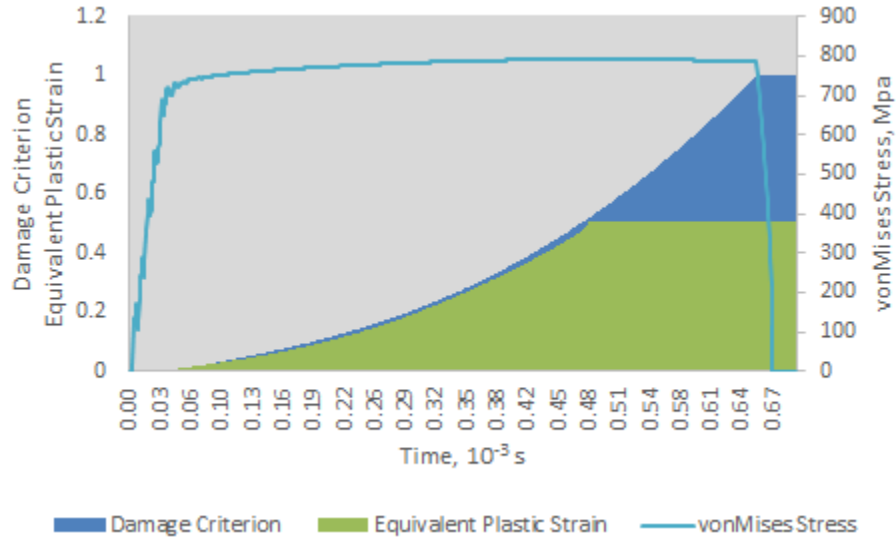


Figure 29. ABAQUS output for the vonMises stress, equivalent plastic strain, and damage criterion for a 1000/s, 223°C simulation

The experimental and simulation results are plotted against each other in Figures 32-34. Each figure features all temperatures (23°C, 223°C, 466°C, and 707°C) run at the same strain rate. Figure 32 shows the 500/s curves, Figure 33 shows the 1000/s curves, and Figure 34 shows the 1800/s curves. Dashed lines indicate the simulated runs, and solid lines indicate averaged experimental curves. Failure strains from the simulation are taken to be the strain value value of D is equal to 1. The failure strains are recorded in Table 8.

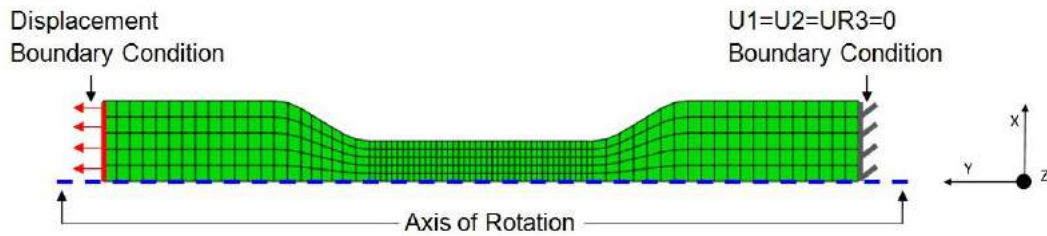


Figure 30. ABAQUS Explicit finite element model of an approximated sub-size E8 dogbone specimen in tension subjected to the same temperatures and strain rates the Split-Hopkinson Bar specimens experienced.

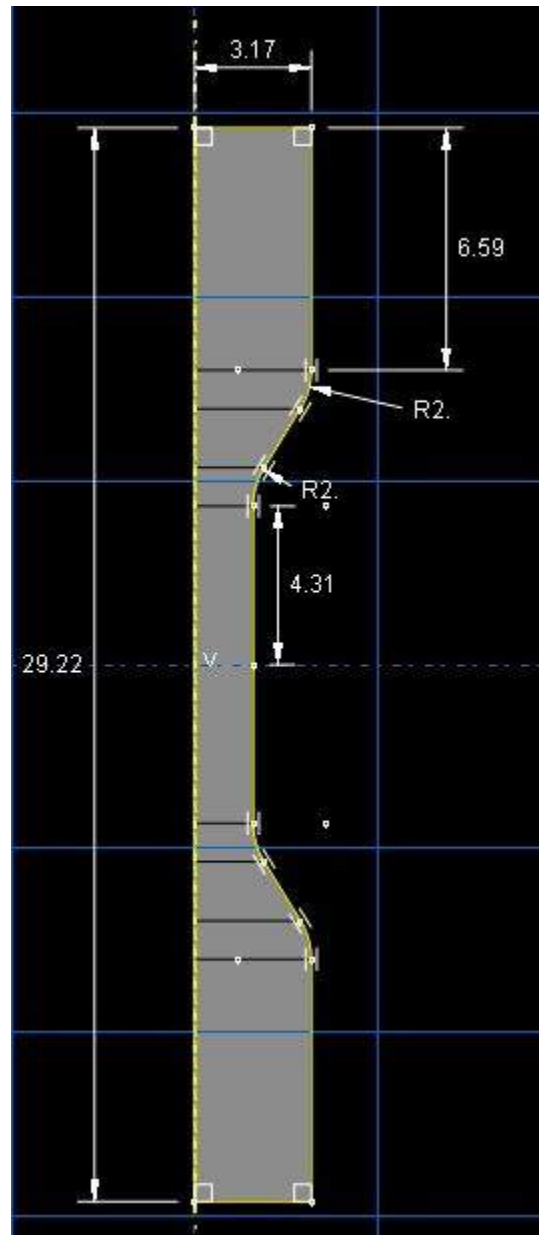


Figure 31. Dimensioned ABAQUS finite element model - units in mm

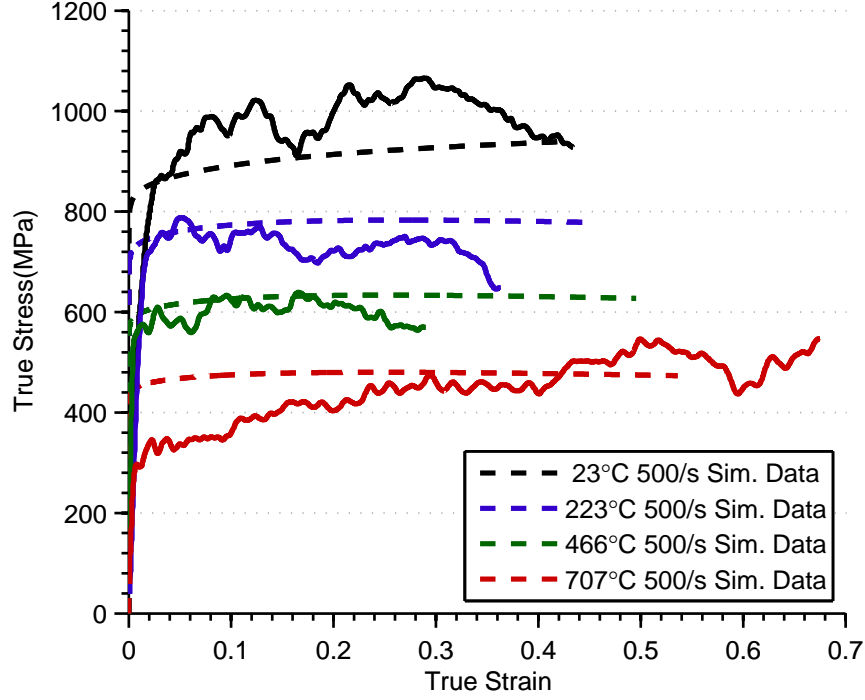


Figure 32. Stress-Strain curve for 500/s impacts at various temperatures. Dashes lines are experimental data, and solid lines are analytically obtained through finite element analysis.

The 500/s curves all show good agreement between experimental and simulated flow stresses at all temperatures. The flow stress decreases as the run temperature increases, which matches what is seen in experiments and what is simulated. The simulated failure strains are larger than what occurred experimentally for the 223°C and 466°C runs, but are fairly close to the 23°C and 707°C experimental curves. The simulations does show some thermal softening, which becomes more prominent as the temperature increases.

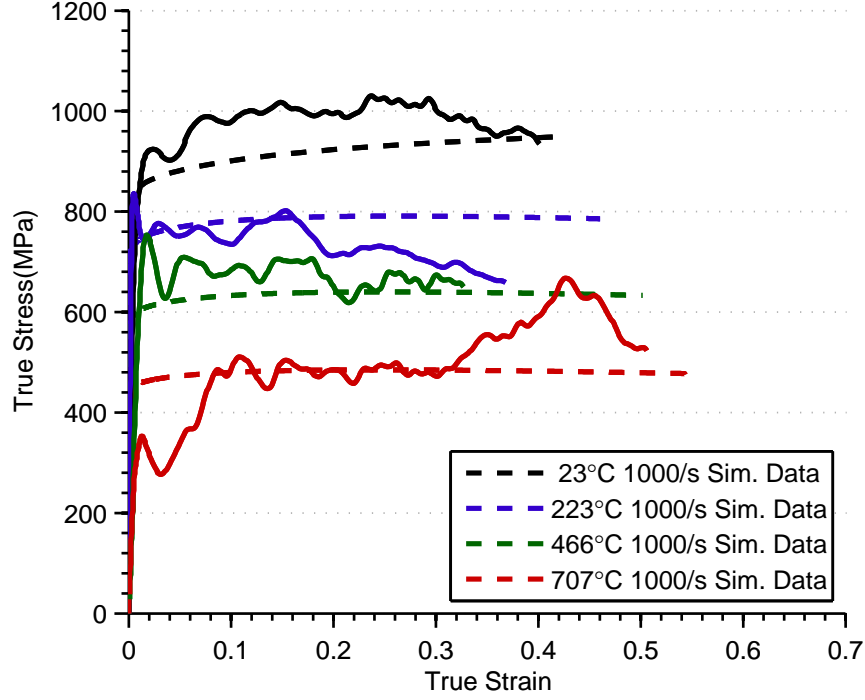


Figure 33. Stress-Strain curve for 1000/s impacts at various temperatures. Dashes lines are experimental data, and solid lines are analytically obtained through finite element analysis.

In the 1000/s curves, the flow stress shows good agreement between simulated and experimental 223°C, 466°C, and 707°C curves, and the 23°C curve is improving over the 500/s runs. Again the failure strain is over-predicted in simulations for 23°C and 707°C, but is very close to the 23°C and 707°C experimental runs.

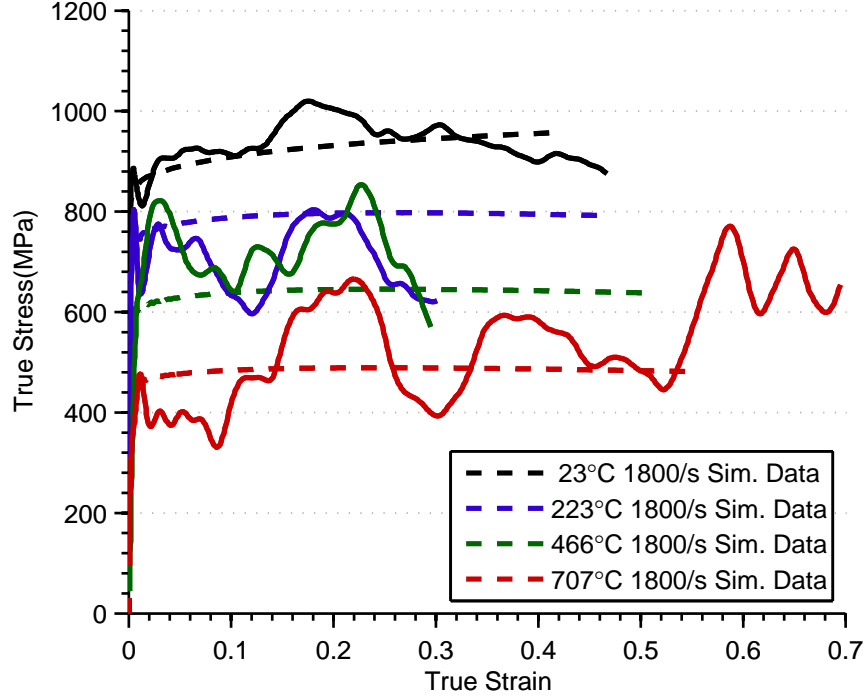


Figure 34. Stress-Strain curve for 1800/s impacts at various temperatures. Dashed lines are experimental data, and solid lines are analytically obtained through finite element analysis.

The 1800/s flow stresses match well for the 23°C and 707°C curves. The noise in the 223°C curves and the 466°C curves makes it difficult to differentiate where exactly the exact trend is, but the predicted flow stresses do give reasonable predictions. As in the other cases, the failure strain is still over-predicted for the mid-range temperatures, but is a little under-predicted for the 23°C experimental failure strain, and ever more so for the 707°C experimental failure strain.

4.3 Discussion

The Johnson-Cook constitutive and damage coefficients can be compared to other characterizations for similar materials. Table 7 contains a few materials regularly used in aerodynamic applications that have been characterized.

Table 7. Comparison of Johnson-Cook strength and damage coefficients for various metals.

Coefficient	4340 Steel [45]	S7 Tool Steel [74]	1045 Steel [75]	Ti06Al4V [43]	Treated 4130 Steel
A	792	1539	553	862	673
B	510	476	600	331	190
n	0.26	0.18	0.23	0.34	0.15
C	0.014	0.012	0.013	0.012	0.017
m	1.03	1.00	1.00	0.80	1.07
D1	0.05	-0.8	0.06	-0.09	-0.19
D2	3.44	2.1	3.31	0.25	0.732
D3	-2.12	0.5	1.96	0.5	0.663
D4	0.002	0.002	0.002	0.014	0.029
D5	0.61	0.61	0.58	3.87	0.716

Comparing the strength coefficients, the yield strength A is a bit low, but is expected as per the specifications of the the heat treatment. The strain hardening coefficients B and n are lower than those compared, but match more closely with materials like Tungsten or VascoMax 300 [11] [3]. The strain rate coefficient C matches well with the other materials, which all show little strain rate dependence on flow stress. The thermal coefficient m is on the low side, but is still reasonable.

Comparing the damage coefficients, void formation coefficients D1, D2, and D3 are all within expected ranges. The strain rate coefficient D4 is higher than the other reported materials, indicating a stronger influence of strain rate on the fracture strain. The thermal coefficient D5 is also within the expected ranges, but is suspect since the experimental behavior was not linear, thus not matching the expected behavior

that the Johnson-Cook model usually uses.

The values of the coefficients themselves are within the expected ranges. When actually using them in the Johnson-Cook model, it generally gives good results, but it is better at some temperatures (room, 707°C) than others (223°C and 466°C) for failure strains. Consider Table 8 for a comparison. The flow equation does give good results, though the results at room temperature are under-predicted.

Table 8. Failure Strains of 4130 steel as measured experimentally and as predicted using the Johnson-Cook failure equation, with calculated percent differences.

Temperature	Strain Rate	Experimental Failure Strain	Simulated Failure Strain	Percent Difference
23°C	570	0.455	0.419	7.91
23°C	1172	0.480	0.421	12.3
23°C	1793	0.493	0.415	15.8
223°C	497	0.363	0.454	25.1
223°C	1116	0.395	0.460	16.5
223°C	1761	0.356	0.463	30.1
466°C	542	0.295	0.496	68.1
466°C	1095	0.330	0.502	52.1
466°C	1757	0.304	0.508	67.1
707°C	525	0.686	0.536	21.9
707°C	1045	0.513	0.544	6.04
707°C	1680	0.706	0.547	22.5

Note that the first three temperatures, 23°C, 223°C, and 466°C actually show a decrease in failure strain, then it more than doubles at 707°C. This could be for a number of reasons. Steel is an allotropic material, and at raised temperatures will

undergo phase transformations altering its structure and material behavior, notably ductility. The highest temperature run in the experiment, 707°C , is close to the transformation temperature point of steel (732°C). The steel may be undergoing a phase change which increases the ductility.

Published thermal properties of 4130 steel seem to support this idea. Right around 700°C , the specific heat capacity begins to deviate from its previously linear trend and starts to spike [76]. Figure 35 shows that right around our highest experimental temperature, the behavior deviates significantly. This most likely explains the sudden uptake in ductility at 707°C .

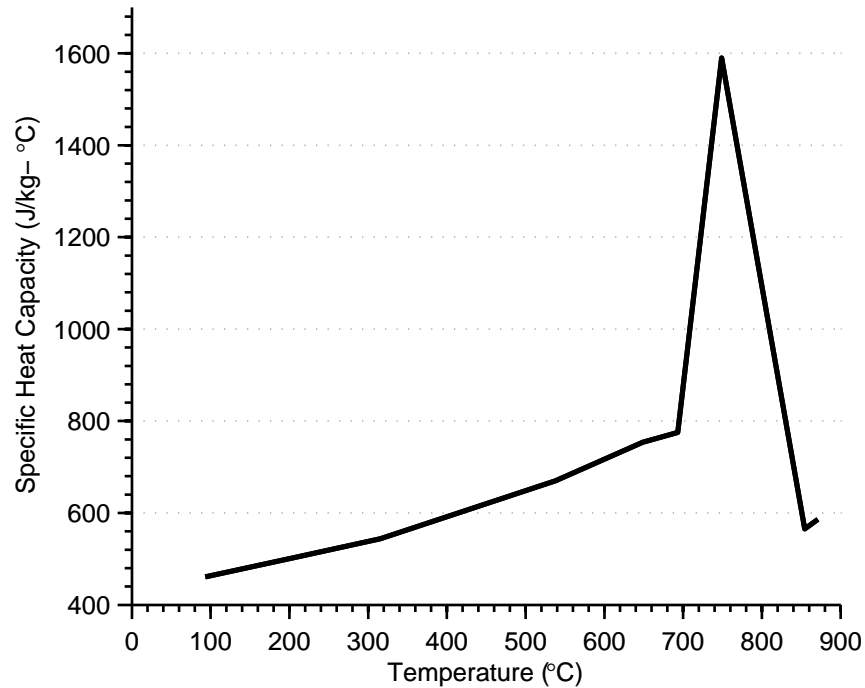


Figure 35. Variation of 4130 specific heat capacity C with temperature. Behavior of α and C begins differing right around 1300°F , or roughly 700°C [76]. Where the specific heat capacity suddenly peaks, the thermal diffusivity dramatically dips.

In order to attempt to improve the failure strain predictions, the damage coefficients were calculated a second time excluding the 707°C data shown in Figure 36. This changed D_5 from 0.7162 to -0.8053 . The failure results are compared in Table

9.

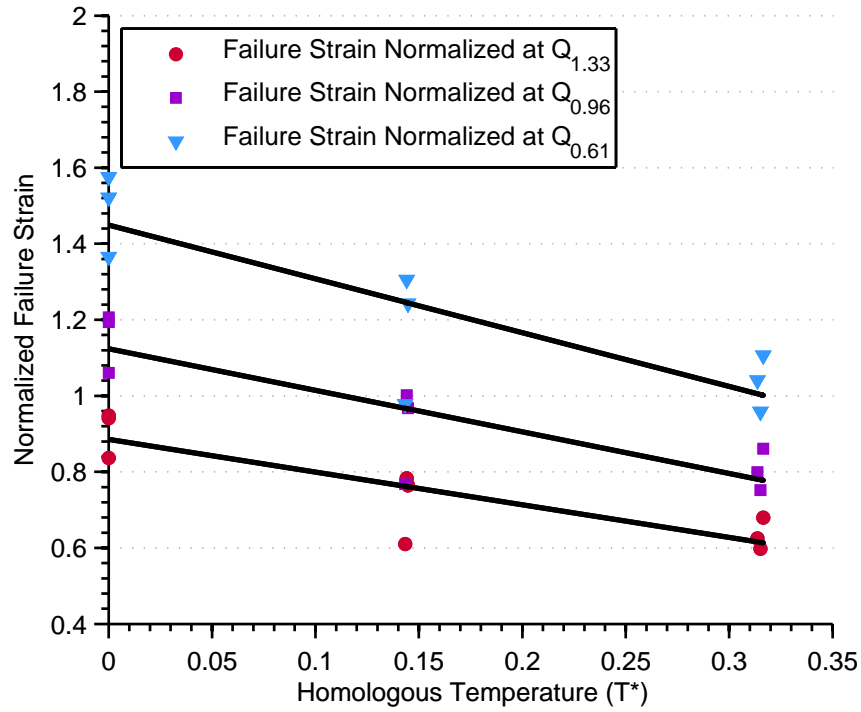


Figure 36. The failure strains of treated 4130 steel are found at each strain rate (500/s, 1000/s, 1800/s) for each temperature (23°C, 223°C, 466°C) and normalized against the triaxiality data at the chosen reference triaxiality. These are plotted against the correlating homologous temperature and fit linearly. As in the thermal m fitting, each strain rate is plotted separately to allow for calibration. The slope of the line is D5, and the calibrated value is -0.8503

Table 9. Failure Strains of 4130 steel as measured experimentally and as predicted using the Johnson-Cook failure equation refit with D5 equal to -0.8503, with calculated percent errors.

Temperature	Strain Rate	Experimental Failure Strain	Simulated Failure Strain, D5 = -0.8503	Percent Difference
23°C	570	0.455	0.403	11.4
23°C	1172	0.480	0.409	14.8
23°C	1793	0.493	0.412	16.4
223°C	497	0.363	0.369	1.65
223°C	1116	0.395	0.365	7.59
223°C	1761	0.356	0.368	3.37
466°C	542	0.295	0.306	3.73
466°C	1095	0.330	0.311	5.76
466°C	1757	0.304	0.314	3.29

The failure strains are closer to the experimental values and significantly more precise. Previously the maximum percent difference was 68.1%, but now it has dropped to 11.4%. This solution is only viable for a the 23-466°C temperature range though, so for AFIT’s modeling efforts where the temperature reaches the melting point, it is less than ideal for use.

There is another curiosity in addition to the non-linear failure strains. At 466°C the material exhibits high strain rate sensitivity, raising the flow stress almost to the level of the 223°C curve, which is not seen as dramatically at any other temperature.

Most likely the behavior is a result of interactions between strain rate and thermal factors that the model is not built to take into account. This will be verified in subsequent sections.

Figuring out the dislocation intricacies happening during deformation, while ex-

tremely interesting, will be time consuming and may not be the quickest approach for addressing AFIT’s present modeling challenges. If the fracture details are not of interest, the flow model does do a good job and would be acceptable for modeling. However, if the failure of the material is of interest, the damage model does not seem to be a reliable option. This is especially true considering that the material being modeled at AFIT is at temperatures much higher than the ones run in these experiments and the fracture does not occur in a consistent manner.

The fact that the fracture behavior does not have a consistent trend may mean that the Johnson-Cook model may not be the best choice of a damage criterion for high temperature applications. It may be worth investigating other materials-based damage models for simulation purposes, or doing additional characterization work at higher temperatures to get an improved fit for a larger temperature range. Another idea is to simply modify the Johnson-Cook equation to fit the experimental results for this particular material. This is a common practice, and a published example can be found in Couque’s work [52].

4.4 Analytical Numerical Modeling

It is additionally possible to run a simple numerical solution in MATLAB as one more further check of the results. By substituting the solved coefficients into the solved equation, and selecting the desired strain rates and temperatures, the solution for the strength portion is solved easily enough. The same principle applies to the damage criterion, except that that a static triaxiality value must be chosen so the phenomenon of necking is not truly accounted for since we are assuming a 1D case and not varying Q , we assume ϵ_f is the final failure strain. The static triaxiality value is the smallest triaxiality tested, 0.61, as it produced the best results. The results of the numerical analysis are plotted below in Figures 37-39.

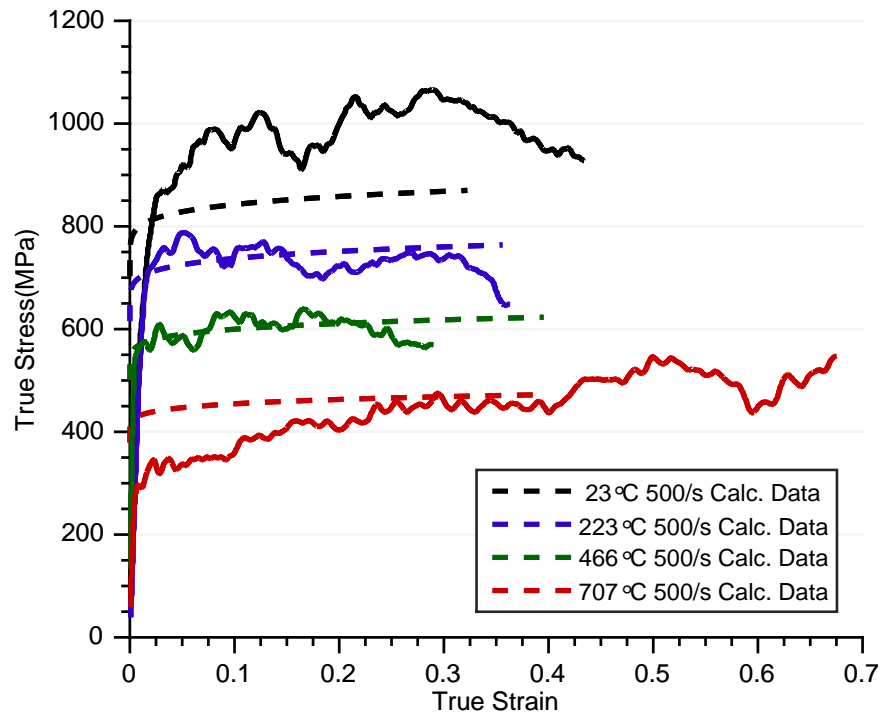


Figure 37. Analytical solution for 500/s curves compared against experimental data

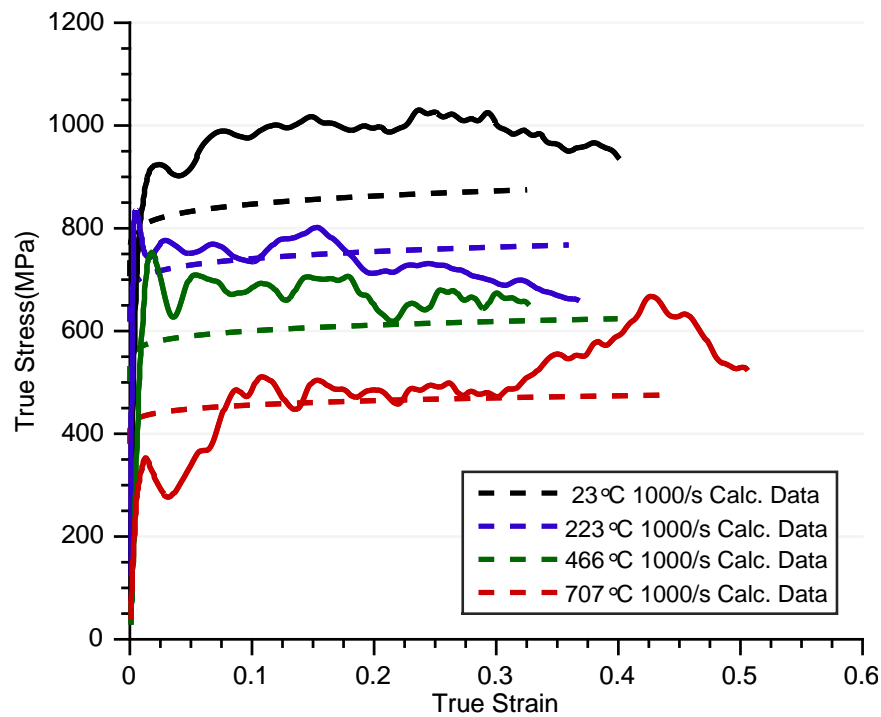


Figure 38. Analytical solution for 1000/s curves compared against experimental data

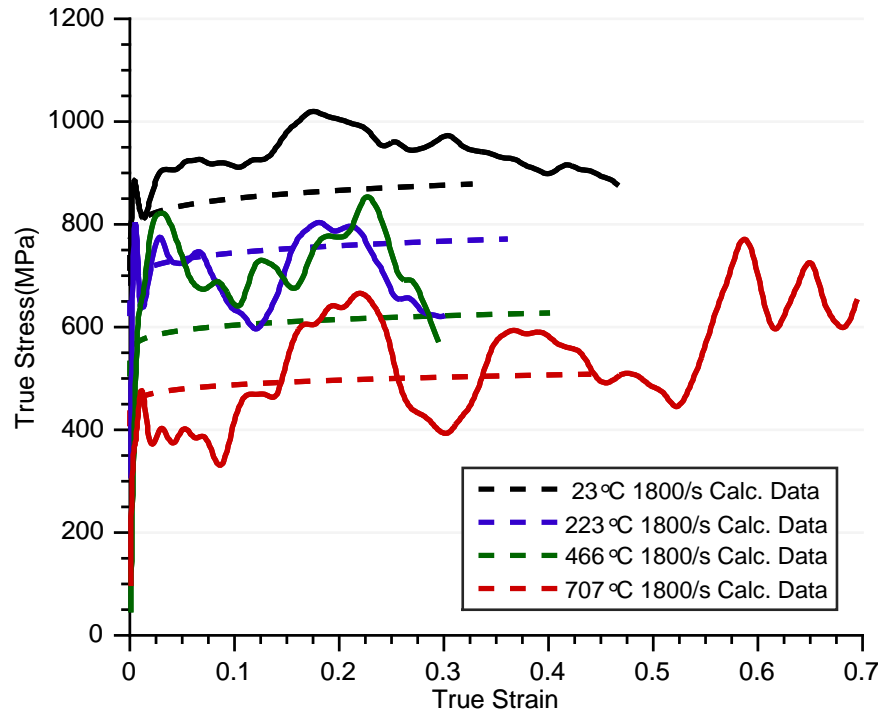


Figure 39. Analytical solution for 1000/s curves compared against experimental data

Comparing these results to the predicted flow stress from ABAQUS, the values are roughly the same, but the analytic solution fails to capture any of the strain softening seen as the temperature of impact increases. ABAQUS however is able to include more features that are not accounted for in the numerical simulation. For one thing, the flow stress being predicted is an equivalent stress, produced from strains that have many different components. The experiments that were run were set up in such a way that it is an approximation of a one-dimensional scenario, so at the center of the gage section the three-dimensional effects should be reduced. However as it is with the nature of testing in the real world, it is unlikely that there are no three-dimensional effects present that would be reflected in the experimental results. The ABAQUS simulation used was an antisymmetric model, so while still an approximation of a three-dimensional scenario occurring, it does have the capability of including some residual stresses effects unaccounted for in the numerical simulation. Additionally,

there is a matter of heat generation going on internally as deformation occurs. As the numerical model is set up now, it does not add any of that, and thus misses out on any thermal softening effects it may have added to the results. Finally, there is the matter of the triaxiality value, which fluctuates as necking is occurring within a specimen, but is chosen as a static value in the numerical simulation. This shows the advantage of being able to include adiabatic heating in the ABAQUS simulation. While the analytical result works as a good estimation, the ABAQUS simulation with its adiabatic heating and variable triaxiality produces more accurate flow stress predictions.

The MATLAB code and ABAQUS input files used to generate these results will be available as an electronic attachment. Now that the material has been characterized for the Johnson-Cook models and compared against numerical and finite element simulations, we will move into the materials characterization portion of this research. In the following chapter, the broken samples from this experimental program will be prepped for measurement and characterized.

V. Material Analysis

The stress-strain curves from high speed dynamic impacts have been successfully generated and used to characterize the macrobehavior for the Johnson-Cook model. Now that the formal testing program has been accomplished and the stress-strain data analyzed, there is still a wealth of information to be gleaned from the material itself. As acknowledged earlier, most material behavior has been characterized via phenomenological experiments. This has led to a somewhat segmented approach to modeling the behavior of materials, with many models being generated only for specific materials with limitations based on the conditions the material will be placed into. The model in this study, Johnson-Cook, is popular for ductile materials but is only valid for certain ranges of strain rates. It would appear there are even further limitations for the damage model. Making observations about what is occurring in the internal material structure under high strain rates will be of value in determining what exactly occurs during deformation. It will help define important areas of focus by identifying exactly which portions of the Johnson and Cook equations are tied to what material features. These observations are useful in building structure-property relationships for material behavior.

The next section will make several observations about the microstructure that occurs near the failure region of the sample. Electron Backscatter Diffraction (EBSD) was used for the primary method of measurement in conjunction with orientation imaging software (OIM) produced by the company EDAX, and the variables of interest are the grain size, misorientation, dislocation density, and elastic modulus. Since the testing program allowed systematic variation of the temperature and the strain rate the material was exposed to, each of these variables will be analyzed to determine whether they vary for the conditions. If a variable is identified as varying with temperature and strain rate in a statistically significant way, then it is identified as being

statistically significant. These features are targeted for creating structure-property relationships. Two sections of a sample are tested for these variables: a pre-necking region, in the gage section, but not in the area where necking occurs, and then at the site of failure, as shown in Figure 40.

This way observations can be made about the microstructure as applicable to the flow stress equation in the pre-necked region and as applicable to the damage equation in the failure region. They will then be related back to the the Johnson-Cook damage model to see if there can be any relationships built between the Johnson-Cook coefficients and the microproperties of the material. In the next few paragraphs, the microstructural variables will be described and their significance to plastic deformation highlighted.

Misorientation Angle.

The misorientation angle is the minimum rotation angle required to bring two lattices into coincidence [77]. These angles can be divided into two groups: Low Angle Grain Boundaries (LAGB), which occur between 2-15 degrees, and High Angle Grain Boundaries (HAGB), which are angles greater than 15 degrees. In the process of deformation, for planes of atoms to move, they need to be oriented just right to

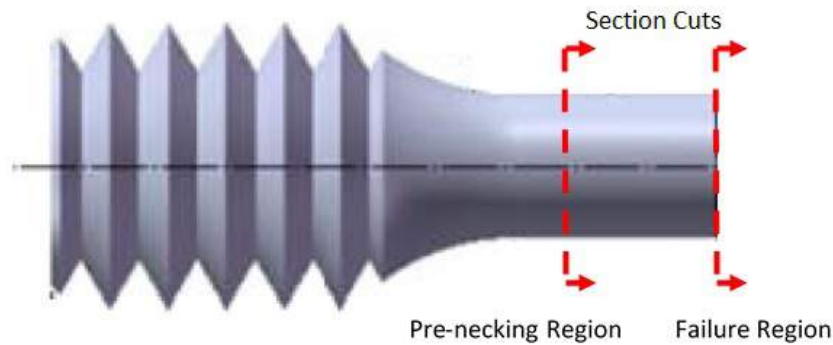


Figure 40. Sites on sample where measurements were taken for pre-necking and failure regions.

initiate movement. Every crystal structure has preferential orientations where these occur, and they are known as slip planes. The greater the angle of misorientation, the more resistance there is to plastic flow, because it will take more effort to re-align the material so the preferred slip plane will be in the ideal position to allow movement.

Grain Size.

Grains are a collection of repeating crystal lattices that all have the same orientation. In a monocrystalline material, there is only one grain with one orientation, but in polycrystalline materials, there are many grains all divided by boundaries where a new grain begins at a new orientation. The grain size is the average size in micrometers of the grains in a scanned area, not including those on the edge of the scan taken. This measurement is important because grain size has been shown to highly impact the mechanical performance of materials. It is well established that larger grains, due to having fewer grain boundaries in the overall structure, allow plastic deformation to happen more easily, resulting in a lower ultimate stress and an increase in ductility. Smaller grains have the opposite effect. Grains can increase in size with increasing temperature, and can also nucleate and form new, smaller grains when dynamic impact occurs.

Geometrically Necessary Dislocations.

Dislocations are defects within the crystal structure that move as plastic deformation is occurring. A higher dislocation density indicates that plastic deformation is easier to induce. These occur most frequently between grain boundaries, but also can occur within the grains themselves. To actually see the dislocations, a transmission electron microscope must be used, but it is possible to make a mathematical estimation based on the misorientation of the grains. In OIM (the orientation imag-

ing software), the equation used provides a lower-bound estimation of the density of dislocations [78].

This density is calculated from a dislocation tensor known as Nye's tensor, α_{ij} , expressed in the equation below

$$\alpha_{ij} = e_{ijk}(\varepsilon_{jl,k}^e + g_{jl,k}) \quad (60)$$

ε^e is the elastic strain tensor, g is the lattice orientation matrix.

Without the presence of long range elastic stress fields, the tensor can also be written as

$$\alpha_{ij} = e_{ijk}g_{jl,k} \quad (61)$$

or

$$\alpha_{ij} = \text{curl}(g) \quad (62)$$

Thus, the dislocation tensor is calculable from the measured gradient of the orientation field measured during EBSD scans. This tensor can be used to find a relationship to the dislocation density. Again Nye has a relationship for us:

$$\alpha_{ij} = \sum_{k=1}^K \rho^k b_i^k \hat{z}_j^k \quad (63)$$

ρ is the dislocation density, k is the type of dislocation, b is the Burger's vector, and z is the line direction. Numerical methods are used to solve this equation using constraints like minimization of the total dislocation line length.

Elastic Modulus.

OIM software can also make an estimation of the stiffness, the macroproperty that most recognized as the slope of the linear portion of the stress-strain curve [78].

This is a variable of interest to determine if dynamic impact is having an effect on the elastic properties, which would indicate that they cannot be assumed to be a constant value in modeling. OIM is able to approximate the elastic modulus again by using the orientation matrix g to calculate a stiffness strain tensor. In the generalized Hook's law, it is expressed as

$$\varepsilon_{ij} = S_{ijkl}\sigma_{kl} \quad (64)$$

where S_{ijkl} are 81 elastic compliance constraints for the material [78]. Or expressed as stress in terms of strain,

$$\sigma_{ij} = C_{ijkl}\varepsilon_{kl} \quad (65)$$

where C_{ijkl} is the stiffness tensor for a crystal. The elastic modulus for a polycrystalline material can be approximated using the Voight and Reuss averaging schemes shown in Equations 66 and 67 respectively [78].

$$C_{ijkl}^V = \frac{1}{N} \sum_{n=1}^N g_{ip}^{nT} g_{jq}^{nT} g_{kr}^{nT} g_{ls}^{nT} C_{pqrs}^X \quad (66)$$

$$S_{ijkl}^R = \frac{1}{N} \sum_{n=1}^N g_{ip}^{nT} g_{jq}^{nT} g_{kr}^{nT} g_{ls}^{nT} S_{pqrs}^X \quad (67)$$

where X is a single crystal tensor, C_{ijkl}^V is the stiffness tensor approximated using the Voight averaging scheme, S_{ijkl}^R is elastic compliance constraints matrix approximated using the Reuss averaging scheme, T is the transpose of the matrix, equivalent to the inverse for rotation matrices. N is the number of measurements taken in the EBSD scan [78].

The Voight compliance tensor can be inverted to calculate a stiffness tensor, which

can be averaged with the Reuss stiffness tensor resulting in an approximated polycrystalline average stiffness tensor (the Bishop-Hill average) [78].

Now that the variables themselves are defined, in the next section the methods used to measure them will be described.

5.1 Microstructural Sample Preparation and Measurement

Since 4130 steel has been systematically tested at certain conditions (strain rate and temperature), the opportunity exists to examine what is happening microstructurally and try to determine which factor (strain rate or temperature) is the driving cause of observed changes.

The Materials Characterization Facility (MCF) at the Air Force Research Laboratory (AFRL) supplied the equipment used in this portion of research. Scanning Electron Microscope (SEM)s are extremely robust pieces of equipment with a wide variety of measuring capabilities, so it is used most extensively. The SEM allows us to measure chemical composition using Energy Dispersion Spectroscopy (EDS) detectors and a variety of grain structure features using Electron Backscatter Diffraction (EBSD). EBSD and orientation imaging microscopy will allow measurements of grain size, misorientation angle, elastic modulus, and dislocation density.

To observe the microstructure, careful sample preparation is required. For EBSD in particular, it is essential that the surfaces being measured be extremely smooth and polished. The following are the steps taken for all specimen preparation to insure uniformity of results.

Specimens were sectioned using an Isomet 1000 equipped with a wafering blade and cut at a speed of 200RPM with an applied weight of 20lbs. Sectioned pieces were mounted in 25mm polyfast molds using a Struers hot compression mounting machine. As the specimens were very small, during mounting polyfast fines were used to first

cover the sample before the courser material was placed on top. The polyfast molds were heated at 180°C for 3.5 minutes at a pressure of 4800 psi, then water-cooled on high for 1.5 minutes. For analysis, it was critical that the samples have an extremely smooth surface finish. Samples were polished using a Buehler Automet 250 automatic grinder/polisher using a sequence defined by MCF staff, based on recommendations from the Buehler polishing manual [79]. The polishing steps are outlined in Table 10.

Table 10. Grinding and polishing sequence used to prepare heat-treated 4130 samples for EBSD analysis

Step	Pad	Primer/Fluid	Base Rotation	Head tation	Ro- tation	Direction	Load	Time (min)	Notes
1	240 grit	Water	300RPM	60RPM		CW*	6lbs/sample	1:00	Repeat until entire surface is exposed
2	320 grit	Water	300RPM	60RPM		CCW**	6lbs/sample	1:00	
3	400 grit	Water	300RPM	60RPM		CCW**	6lbs/sample	1:00	
4	600 grit	Water	300RPM	60RPM		CCW**	6lbs/sample	1:00	
5	Nylon	Water, 9um sion, Metadai	200RPM	50RPM		CCW**	5lbs/sample	2:30	
6	TexmetC	Water, 3um sion, Metadai	200RPM	50RPM		CCW**	5lbs/sample	2:30	
7	TexmetC	Water, 1um sion, Metadai	200RPM	50RPM		CCW**	5lbs/sample	2:30	
8	ChemC	0.05um colloidal silica suspension	150RPM	50RPM		CW*	4lbs/sample	4:00	Rinsed with water for final 20 seconds of polishing

* Clockwise

** Counter-clockwise

Grinding steps for 240, 320, 400, and 600 grit grinding pads all used the same procedure. Samples were ground for 1 minutes using a base rotation of 300RPM and a head rotation of 60RPM run counter-clockwise while applying a force of 6lbs per specimen and rinsing with water. For $9\mu\text{m}$, a nylon polishing pad is primed with water, then a $9\mu\text{m}$ suspension mix is used alternating with metadi (a lubricating fluid) to keep the pad moist. The base rotation is 200rpm, the head rotation is 50RPM, and the force is 5lb per sample, run for 2 minutes and 30 seconds. For $3\mu\text{m}$ and $1\mu\text{m}$ polishes, a TexmetC pad is used, and the same settings are used as with the $9\mu\text{m}$ polishing, but with $3\mu\text{m}$ and $1\mu\text{m}$ polishing suspensions respectively. For the final polish, a ChemC pad is used and primed with colloidal silica. It is run for 2 minutes and 30 seconds, with a force of 4 lbs per sample applied, and a base speed of 150RPM and a head speed of 50RPM, run clockwise. For the final 20 seconds of polishing, water is applied to the pad to rinse off excess silica.

Between every polishing stage, the samples were cleaned to prevent cross-contamination from the prior step. In the final cleaning step, samples were rinsed, cleaned with soap, isopropanol, and distilled water, then sonicated in acetone followed by isopropanol. The final result is a mounted sample ready for SEM insertion. such as one shown in Figure 41.



Figure 41. Final product of sample preparation: Sample has been sectioned, mounted, ground, and polished to a $0.05\mu\text{m}$ surface finish

Once the samples are properly prepared for measurements, they are analyzed via EBSD. EBSD is a robust characterization tool, and operates using a process similar to x-ray diffraction. It records crystallographic information based on the orientation of the crystal lattices of the material. Broadly, it is measuring lattice strain, grain and phase boundaries (subsets: low and high angle boundaries, grain size distribution), and certain orientations (cube orientations). It was chosen as a tool for this study because of the relatively easy sample preparation and because of the vast amounts of microstructural features it could obtain for analysis from a single scan. This next section outlines what is happening exactly in the EBSD process and how the measurements are made.

The actual process takes place within the vacuum chamber of a scanning electron microscope, utilizing the electron beam and the scattering of the electrons as it makes contact with the sample, which is tilted at 70° , as seen in Figure 42.

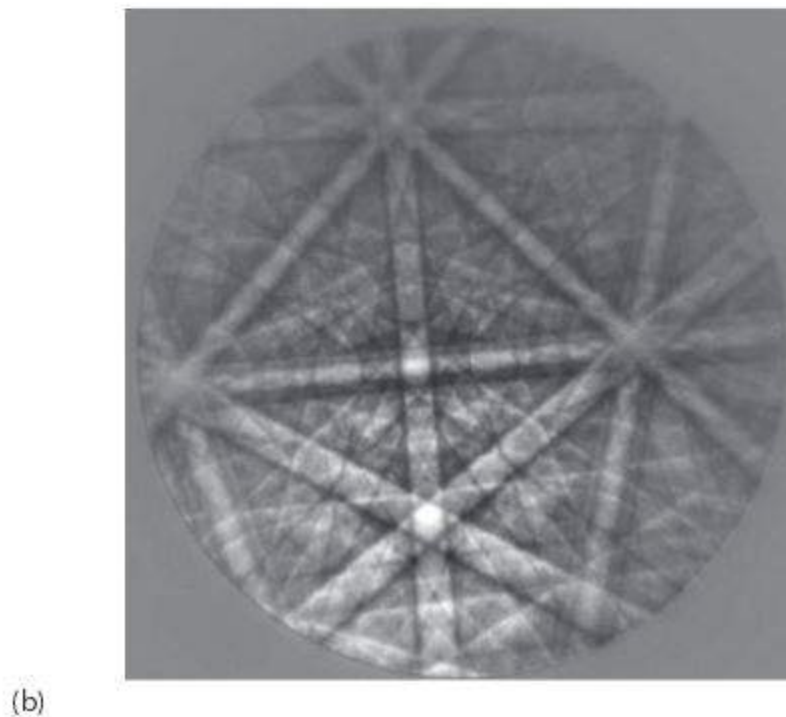
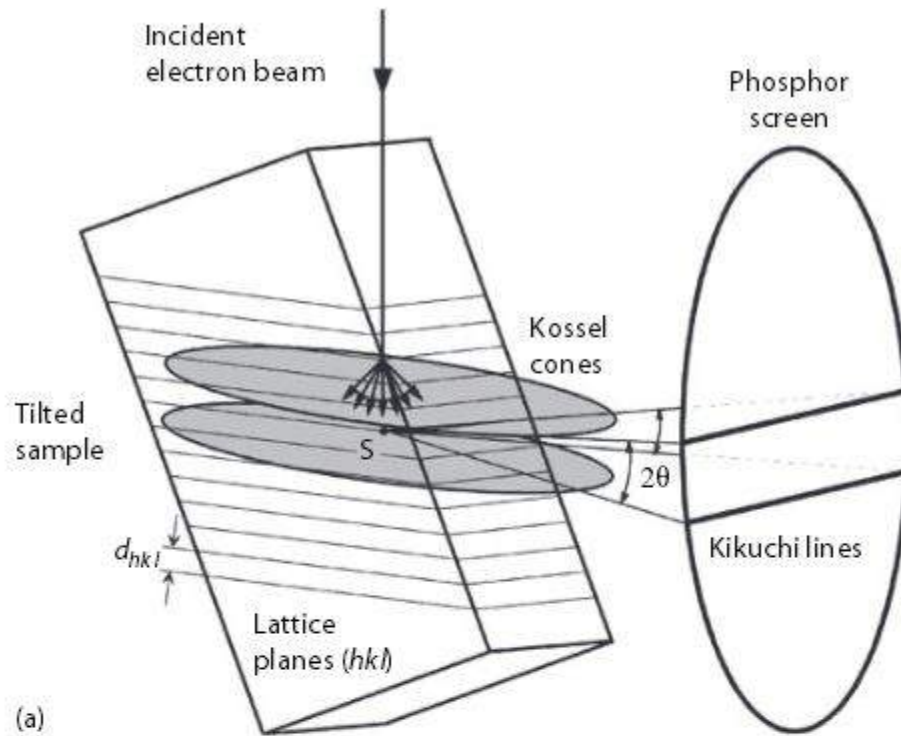


Figure 42. Diagram of the geometry of EBSD alignment. Electrons strike a sample angles at 70° , electrons are diffracted in two cones areas in band lines, which are intercepted and recoded on a phosphor screen [80].

As the electrons impact the sample, some of them are hitting at the precise Bragg angle θ_b at every set of lattice planes, defined in Bragg's equation:

$$n\lambda = 2d\sin(\theta) \quad (68)$$

where n is a constructive interference when equal to a whole number, λ is the wavelength of the electrons, d is the spacing between atomic layers, and θ is the angle of incidence of the electrons. See Figure 43.

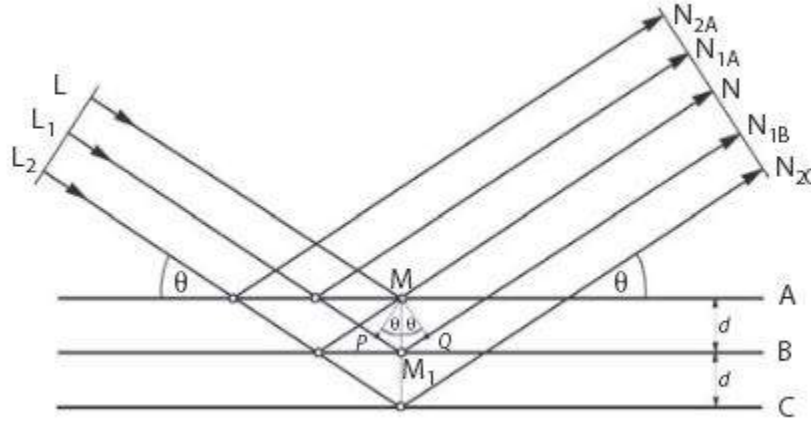


Figure 43. Geometry of Bragg's Law [80].

Backscatter electrons reflect back again in a strong, reinforced beam. These reflections are occurring in all sorts of directions for different planes, so the resulting beam pattern reflects back in the shape of a cone, dubbed the Kossel cone. This cone extends about the normal of the reflecting atomic plane with half apex angle: $90 - \theta_b$. Since it reflects on either side of the plane, there are two resulting cones. Knowing the wavelength of electrons (dependent on the accelerating voltage) and substituting lattice inter-planar spacing into Bragg's Law, the Bragg angle is around. 0.5. Thus the angle of diffraction is close to 180° , making it flat and recordable. A recording medium (phosphor screen) is set in a place where it can intercept these bands, known

as Kikuchi lines, with a spacing equal to $2\theta_b$, proportional to the inter-planar spacing. Each pair of bands corresponds to a distinct crystallographic plane, and each intersection corresponds to a zone axis (pole) and major zone axes correspond to several intersections of bands.

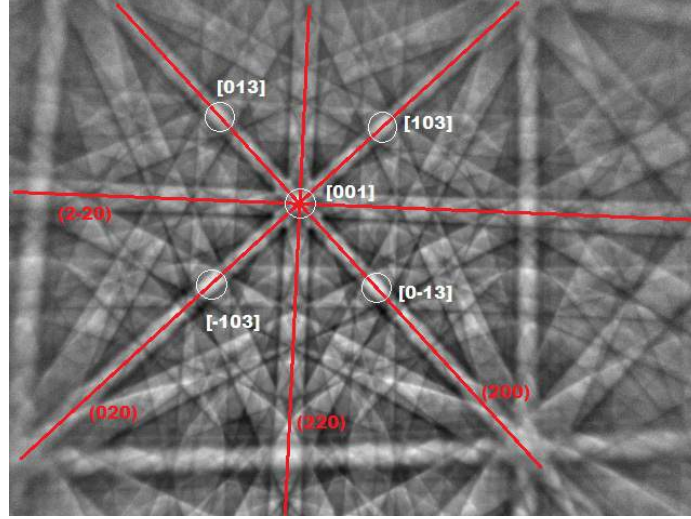


Figure 44. Recorded Kikuchi bands, with intersections indexed [81]

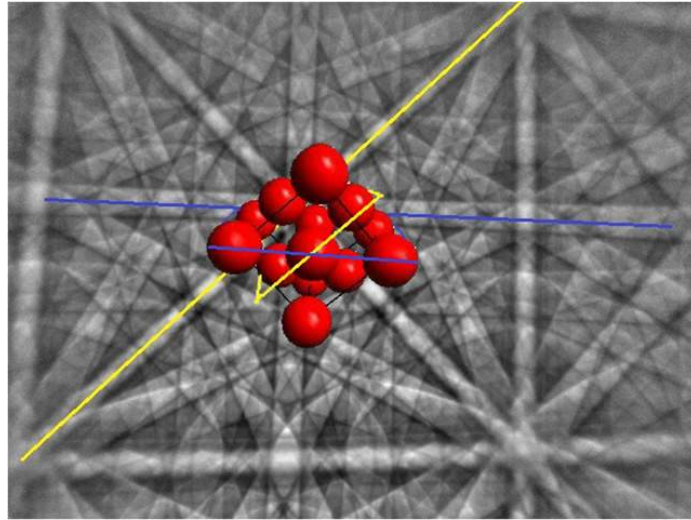


Figure 45. Visualization of a crystal lattice unit cell as indicated by the indexing of the Kikuchi bands [81]

Interpreting the data from the Kikuchi bands is actually a fairly straightforward process. First, the pattern is indexed, whereby crystallographic indices of the Kikuchi

bands and poles corresponding lattice planes are determined. Then the relative position of the bands/poles with respect to the external frame are determined. It is a simple but extraordinarily repetitive and time-consuming process with plenty of opportunity for error, so for practical purposes this process is generally reserved for computer automation.

EBSD Collected Data.

Two different sections from each sample were prepared for analysis: one at the very end of the sample in the fracture region, and one still in the gage section, but farther back so as not to be affected by necking. These will be dubbed the fracture and pre-necked sample groups respectively. The goal is to be able to make observations about microstructural relationships for both the damage criterion, which will correlate to the microstructure seen in the failure region, and the flow equation. Since necking has not taken place where the pre-necked samples were taken, it will not be affected by properties related to the damage equation.

The data was scanned twice in different locations on the surface at one set magnifications, 500x, and scanned with a step size of $0.3\mu\text{m}$. The total area scanned is $140\mu\text{m} \times 140\mu\text{m}$, or (0.0196mm^2) . The numbers are generated from averages of distributions of measurements given by the OIM software.

The results of the pre-necked scans are shown below in Table 11. It denotes which sample is being tested, the experimental conditions the sample was subjected to during testing for the Johnson-Cook coefficients (temperature and strain rate), and then the averaged value for dislocation density, grain misorientation, misorientation angle, stiffness, and grain size as previously described.

Table 11. EBSD Measurements of the pre-necked zones of dynamically-impacted heat treated 4130 steel

Subject	Temp (°C)	Strain Rate (s^{-1})	Dislocation Density** (Number of dislocations)	Misorientation** Angle (Degrees)	Stiffness E (GPa)	Grain Size Microns
25E	24	500	166.500	11.5685	178.498	11.0866
25E	24	500	167.629	11.5593	179.663	12.0241
4E	24	1000	171.947	11.7010	176.454	10.4170
4E	24	1000	158.574	11.5130	171.362	*
8E	24	1800	117.244	12.4444	172.827	*
8E	24	1800	118.803	12.5448	176.017	*
29E	223	500	174.165	11.6113	172.757	11.4382
29E	223	500	158.397	11.4189	174.966	11.4382
13E	223	1000	174.479	11.6415	179.199	10.9003
13E	223	1000	161.442	12.4714	174.911	11.0221
10E	223	1800	113.877	15.6408	172.827	*
10E	223	1800	115.333	13.0074	177.980	*
31E	466	500	163.235	11.6410	173.105	12.4822
31E	466	500	162.808	12.1856	177.438	11.5991
18E	466	1000	176.319	11.7265	177.771	10.8527
18E	466	1000	171.629	11.3354	178.679	11.6645
37E	466	1800	168.623	11.9372	177.178	11.1100
37E	466	1800	173.340	11.8144	178.737	10.4490
34E	707	500	124.432	15.9132	179.038	10.8943
34E	707	500	129.904	15.4259	181.668	10.3075
40E	707	1000	128.104	15.3907	177.803	10.4159
40E	707	1000	118.909	17.1495	176.201	11.0428

Table 11. EBSD Measurements of the pre-necked zones of dynamically-impacted heat treated 4130 steel

Subject	Temp (°C)	Strain Rate (s^{-1})	Dislocation Density** (Number of dislocations)	Misorientation** Angle (Degrees)	Stiffness E (GPa)	Grain Size Microns
43E	707	1800	147.980	14.3681	181.581	10.1187
43E	707	1800	149.139	13.8192	175.863	10.8245

** Non-normal distribution - data transformed for analysis, shown in Chapter V

* Outlier - removed from analysis

Table 12 gives the same information for the fracture region. It denotes which sample is being tested, the experimental conditions the sample was subjected to during testing for the Johnson-Cook coefficients (temperature and strain rate), and then the averaged value for dislocation density, grain misorientation, misorientation angle, stiffness, and grain size as previously described.

Table 12. EBSD Measurements of the fracture zones of dynamically-impacted heat treated 4130 steel

Subject	Temp (°C)	Strain Rate (s^{-1})	Dislocation Density** (Number of dislocations)	Misorientation Angle (Degrees)	Stiffness E (GPa)	Grain Size** Microns
25F	24	500	167.854	13.6434	181.693	10.0270
25F	24	500	173.751	12.6786	181.455	7.0037
25F	24	500	224.574	11.4862	181.481	8.5813
25F	24	500	221.720	12.0136	177.828	8.9754
4F	24	1000	136.150	20.0627	184.270	12.9712
4F	24	1000	136.457	*	185.815	8.4533
4F	24	1000	149.589	14.2631	181.411	8.3115
4F	24	1000	149.317	15.0375	177.676	7.3177

Table 12. EBSD Measurements of the fracture zones of dynamically-impacted heat treated 4130 steel

Subject	Temp (°C)	Strain Rate (s^{-1})	Dislocation Density** (Number of dislocations)	Misorientation Angle (Degrees)	Stiffness E (GPa)	Grain Size** Microns
8F	24	1800	165.235	10.2057	187.339	16.3676
8F	24	1800	136.140	9.8562	183.094	*
8F	24	1800	167.136	13.1357	193.194	10.6991
8F	24	1800	163.971	11.7287	174.612	16.3004
29F	223	500	174.744	12.6264	176.340	8.1752
29F	223	500	232.573	14.0869	*	7.6608
29F	223	500	224.573	11.4843	181.481	8.5591
29F	223	500	229.991	11.9984	*	8.9060
13F	223	1000	185.231	14.3756	180.721	6.46825
13F	223	1000	182.832	14.2178	180.603	7.15227
13F	223	1000	237.306	13.3732	181.655	6.18047
13F	223	1000	238.342	13.1257	182.222	6.16657
10F	223	1800	157.106	10.3383	178.335	18.6718
10F	223	1800	169.084	10.5001	179.791	14.7305
10F	223	1800	199.797	9.5028	176.375	16.9776
10F	223	1800	198.650	10.0513	177.026	8.1016
31F	466	500	170.596	13.3867	179.422	8.0024
31F	466	500	180.319	12.3514	183.452	9.3045
31F	466	500	222.609	10.8040	175.496	10.6547
31F	466	500	218.854	10.8268	189.515	9.2202
18F	466	1000	188.825	11.7860	177.878	9.9626
18F	466	1000	173.809	12.0157	174.942	9.9989

Table 12. EBSD Measurements of the fracture zones of dynamically-impacted heat treated 4130 steel

Subject	Temp (°C)	Strain Rate (s^{-1})	Dislocation Density** (Number of dislocations)	Misorientation Angle (Degrees)	Stiffness E (GPa)	Grain Size** Microns
18F	466	1000	246.084	10.8294	175.644	7.8460
18F	466	1000	226.604	11.9137	181.257	8.4278
37F	466	1800	184.624	11.0946	178.684	9.5176
37F	466	1800	186.108	11.0843	182.608	9.2782
37F	466	1800	222.920	10.7514	169.961	9.1253
37F	466	1800	213.625	10.6650	178.385	12.4403
34F	707	500	144.813	15.3444	176.743	6.5444
34F	707	500	139.955	15.2095	181.853	7.3508
34F	707	500	177.655	16.1479	185.706	6.4946
34F	707	500	173.908	15.1757	184.648	6.9449
40F	707	1000	147.405	15.9609	180.391	5.9882
40F	707	1000	152.940	14.2561	183.617	8.7955
40F	707	1000	171.771	16.1745	185.740	8.9014
40F	707	1000	179.623	15.1450	189.906	6.8820
43F	707	1800	148.926	15.4953	180.799	7.8826
43F	707	1800	138.755	16.3606	179.072	7.1144
43F	707	1800	155.598	17.7212	181.542	6.9144
43F	707	1800	169.093	14.8263	173.156	6.2769

** Non-normal distribution - data transformed for analysis, shown in Chapter V

* Outlier - removed from analysis

To show a more visual representation of the data collected in Tables 11 and 12,

the following section will show samples of the grain maps, grain orientation maps, and inverse pole figure (orientation of the specimen projected into the crystal coordinate system [82]) recorded by OIM. Then a summary of the data for all strain rate and temperature combinations normalized against an untested specimen is shown graphically. Additionally, these graphs include error bars that are calculated from standard deviations obtained from the OIM software if provided, or calculated from the variation of measurements in the average taken otherwise.

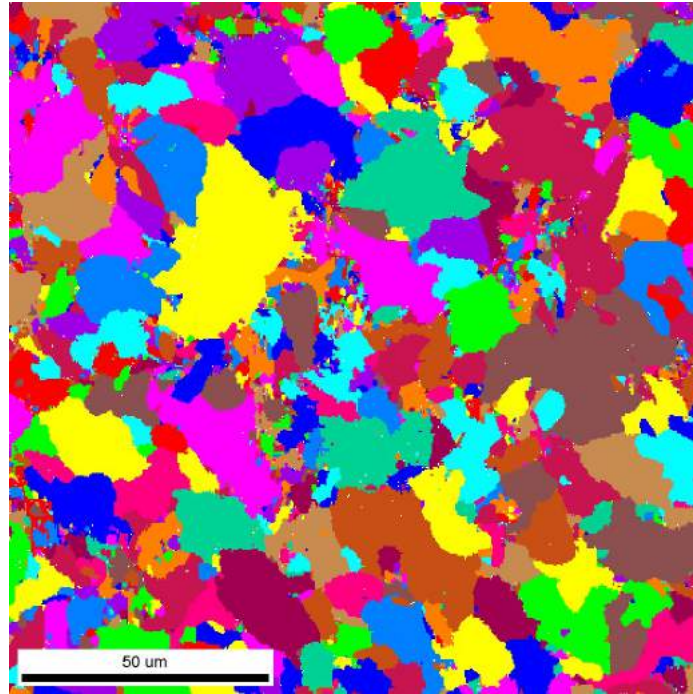


Figure 46. Unbroken Grain Map

Figure 46 shows the division of grains within an untested specimen. It is used to calculate the average grain size with the exception of incomplete grains around the edges, which are excluded from the calculation. The average grain size for this particular grain map came out to $13.2\mu m$. We can compare this against grain measurements for pre-necked and fracture regions of a specimen that underwent dynamic testing. For comparison, we will observe Sample 29 which underwent impact at 500/s at a temperature of $223^{\circ}C$. The grain maps are shown in Figures 47 and 48.

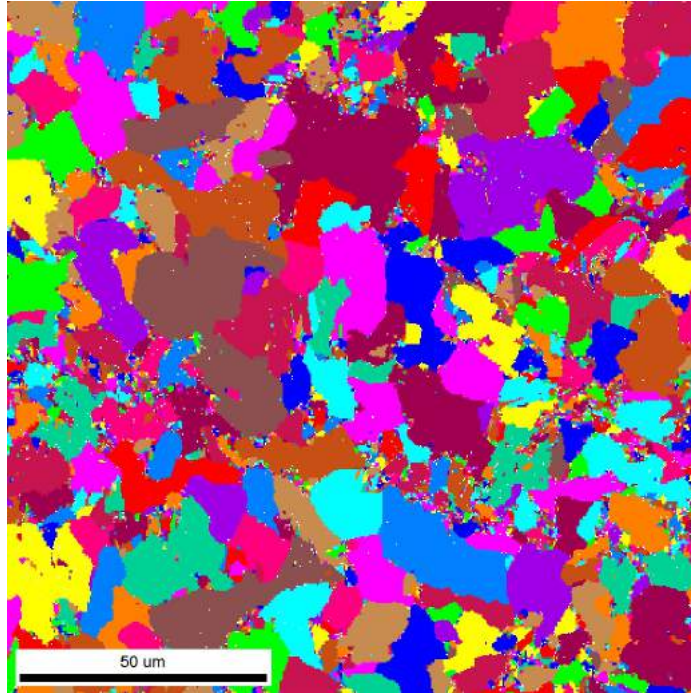


Figure 47. Grain Size for Sample 29E in the pre-necked region -Temperature: 223°C, Strain rate: 500/s

For the pre-necked region in Figure 47, the average grain size measurement was $11.4\mu m$.

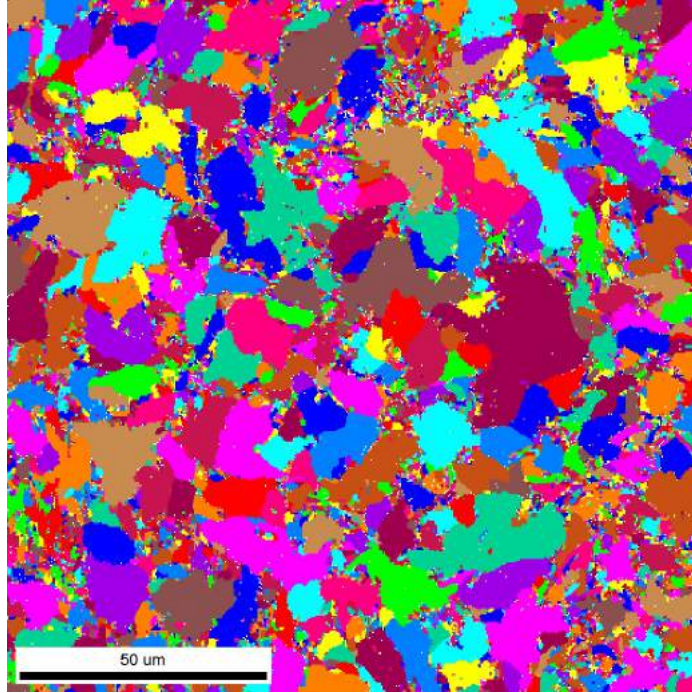


Figure 48. Grain Size for Sample 29E in the fracture region -Temperature: 223°C, Strain rate: 500/s

For the fracture region in Figure 48, the grain measurement was $8.2\mu m$.

The results can be further analyzed by normalizing them against the untested specimen, as shown in Figure 49 and 50. In these figures, the readings for each of the specimens were averaged together to find a single value for each condition, and then divided by the values found in the untested specimen. Error bars are plotted by combining the standard deviations calculated from the distribution measurements in OIM. This process is repeated for the misorientation, dislocation densities, and stiffness measurements shown a little later.

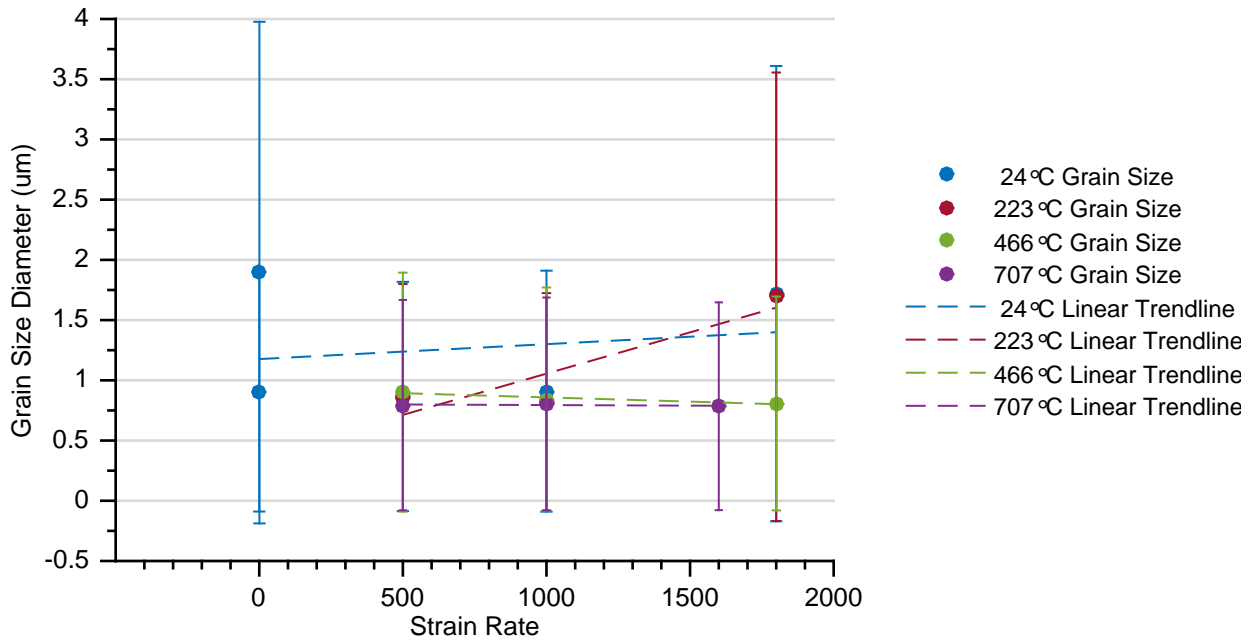


Figure 49. Average normalized grain size for all strain rates and temperature conditions in the pre-necked, where each point is the average of two difference EBSD scans

For the most part, strain rate does not seem to effect the grain size measurement except for at 223°C, where there is a sizable increase at the highest strain rate. Temperature seems to also not have an effect except at the highest strain rate at 24°C and 223°C.

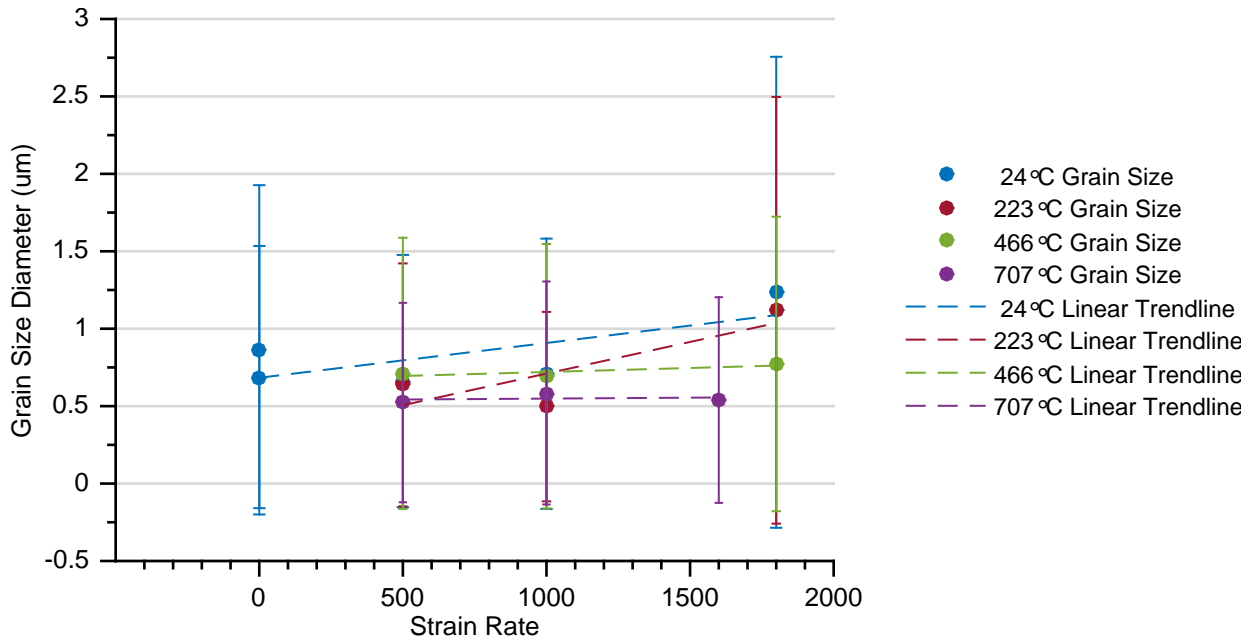


Figure 50. Average normalized grain size for all strain rates and temperature conditions in the fracture region, where each point is the average of four difference EBSD scans

Looking at the linear trends, one can see that as temperature increases the grain size decreases. Increasing strain rate does seem to produce a small increase in grain size. Strain rate has the strongest impact on grain size at room temperature, and the effect decreases with increasing temperature.

Another map that is produced is the boundary angles between/within grains. Figure 51 shows the boundary angle map for an untested specimen.

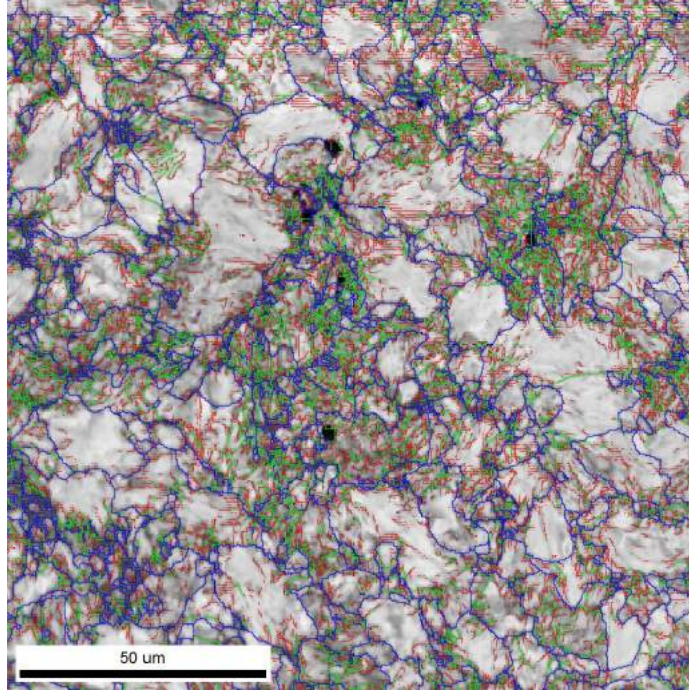


Figure 51. Untested Sample Boundary Angles - red lines indicate angles between 2-5°, green lines indicate angles between 5-15°, blue lines represent angles >15°

Here we can see the measured boundary rotations on the surface of an unbroken specimen coded by color. The red lines indicate angles between 2-5°, the green lines indicate angles from 5-15°, and blue lines indicate angles >15°. Thus the red and green lines are low angle boundaries (LAGBs), and blue lines are high angle boundaries (HAGBs). Note that for the most part, the HAGBs divide the grains, while the LAGBs are within the grains. For this scan the average misorientation was 15.4°.

Now let us look at the boundary density in a fractured sample shown in Figures 52 and 52.

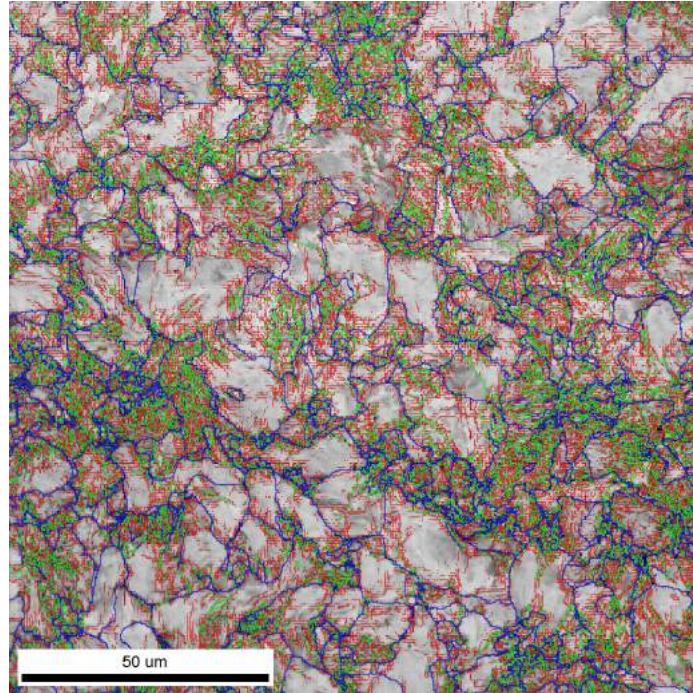


Figure 52. 29E Boundary Density map of the pre-necked region

In the pre-necked region, Figure 52, the average misorientation was 11.6° .

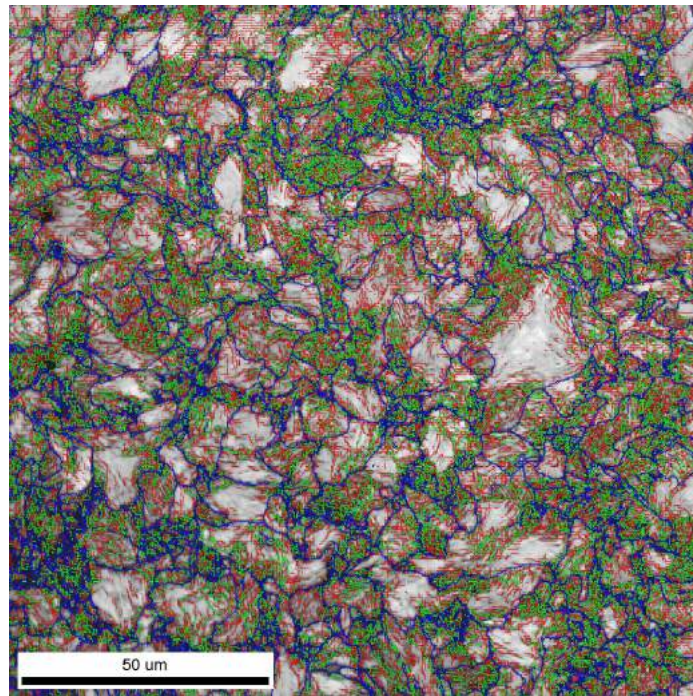


Figure 53. 29F Boundary Density map of the fracture region

In the fracture region, Figure 53, the average misorientation was 12.6° .

Another way to visualize the misorientation is the inverse pole figure, which is a figure that shows the crystallographic orientations observed during the scan. Figure 54 show the color-coded legend used to show the crystal orientations registered in the scan.

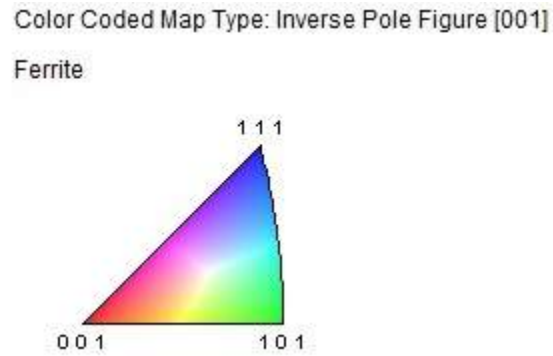


Figure 54. Inverse Pole Function Plot Legend

The variation in colors shows the variations in crystallographic orientations registered in the scan for the ferrite phase. Blue is the $[111]$ series of planes, green is the $[101]$ series of planes, and red is the $[001]$ series of planes. The colors in-between indicate the variation possibilities between those specific planes.

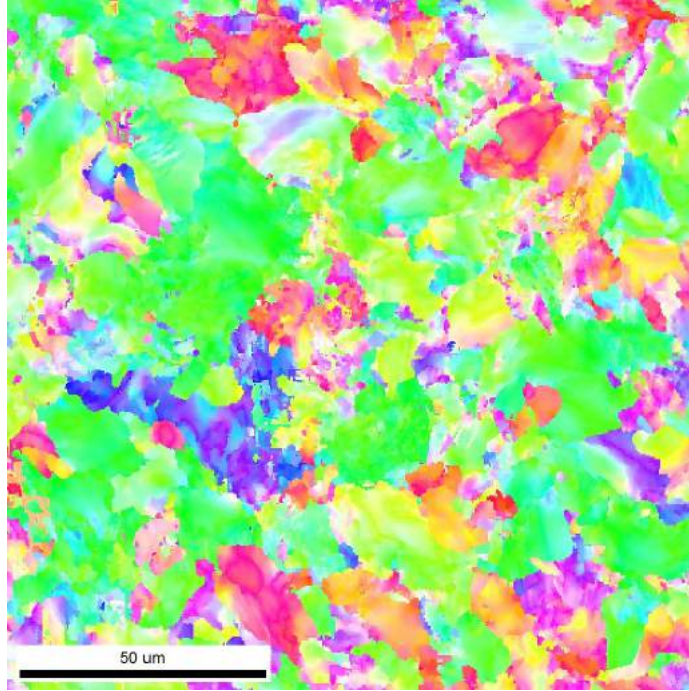


Figure 55. Unbroken Specimen Inverse Pole Function Plot

The inverse pole function plot is a figure that shows all of the different crystal orientations of the existing lattices in the structure. The unbroken IPF is shown in Figure 55, and can be compared against our broken sample 29F's IPF in Figure 57. In the unbroken specimen, we see the $[101]$ and $[201]$ are dominating, with a good mix of $[111]$ and $[221]$. The variety of orientations shows the material is not isotropic.

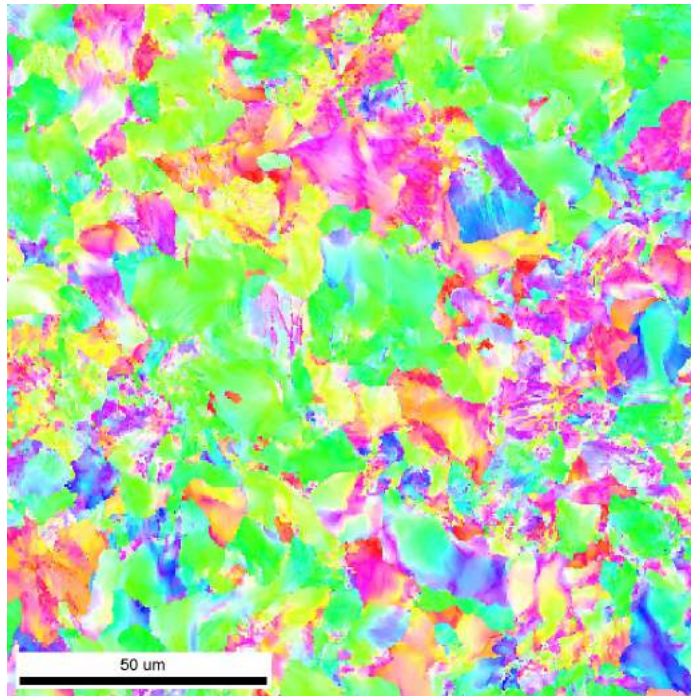


Figure 56. Sample 29E Inverse Pole Function Plot of the pre-necked region

In Figure 56, there appears to be more $[111]$ and $[221]$ orientations.

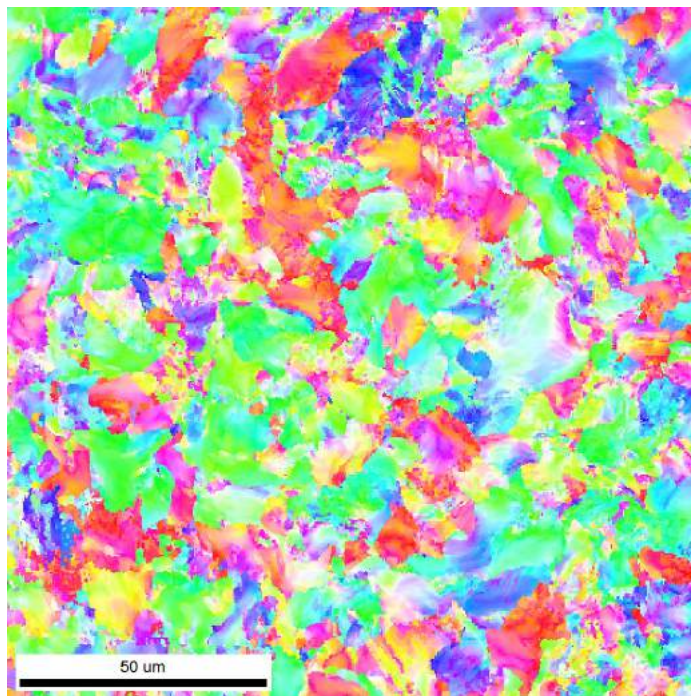


Figure 57. Sample 29F Inverse Pole Function Plot of the fracture region

In Figure 57, there appears to be more [001] and [111] and [101] orientations. Next we can look at the measured responses for each condition.

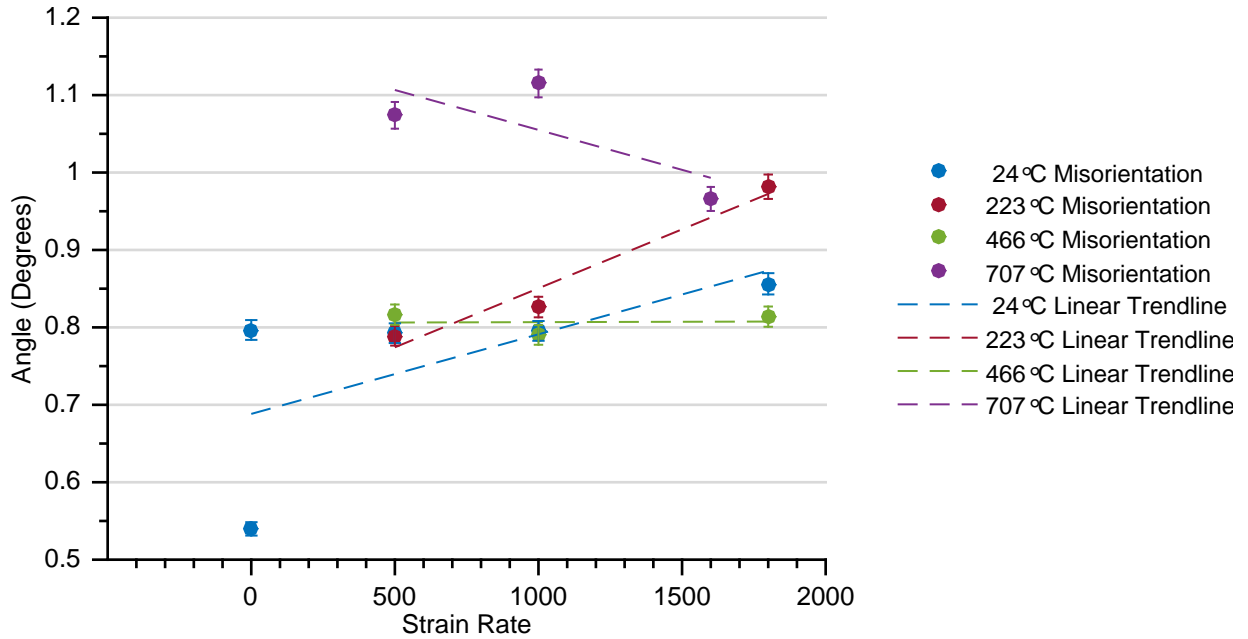


Figure 58. Average normalized misorientation in the pre-necked zone for all strain rates and temperature conditions, where each point is the average of four difference EBSD scans

There is a strong increase with increasing strain rate for temperatures up to 466°C, where then the misorientation begins to decrease. With the exception of 466°C, there is a increase in misorientation with temperature.

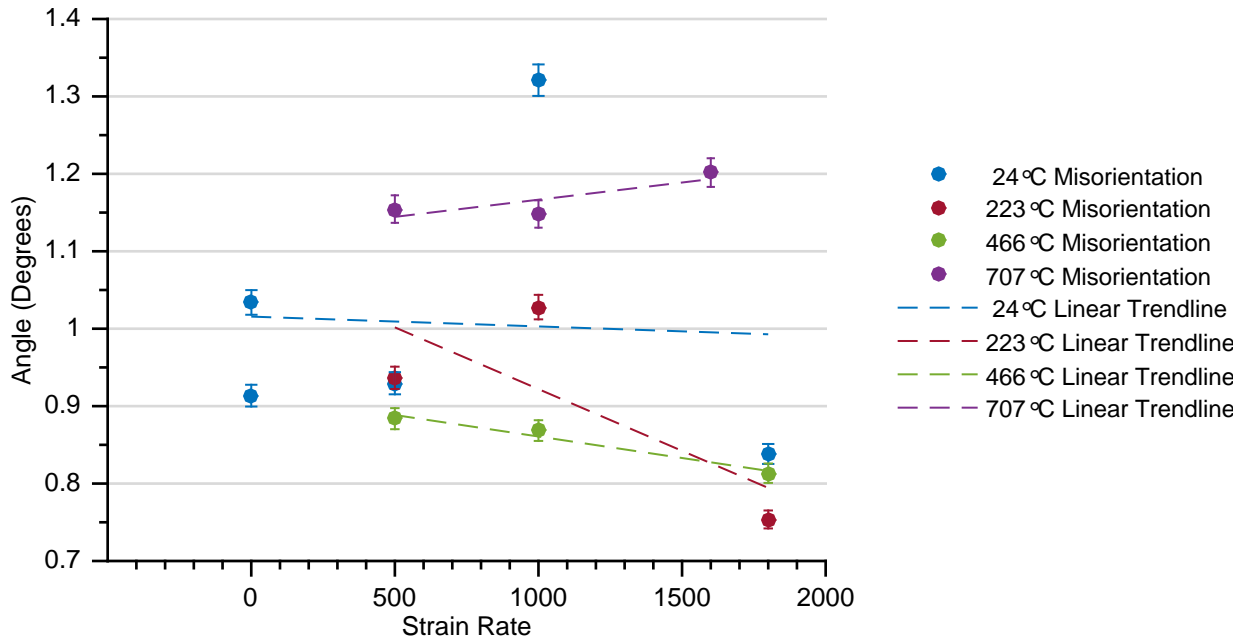


Figure 59. Average normalized misorientation in the fracture zone for all strain rates and temperature conditions, where each point is the average of four difference EBSD scans

The response is quite different for the failure region. The misorientation results for room temperature are extremely varied; the misorientation drops with increasing temperature until it increases for 707°C, and with increasing strain rate, the misorientation does not respond for 24°C and 707°C, and for the mid-range temperature there is a decrease in misorientation.

The dislocation density is a figure based on mathematical calculations, as previously discussed. Figure 60 shows the measured results for all the samples measured in the pre-necked region and Figure 61 shows the normalized measured results in the fracture region.

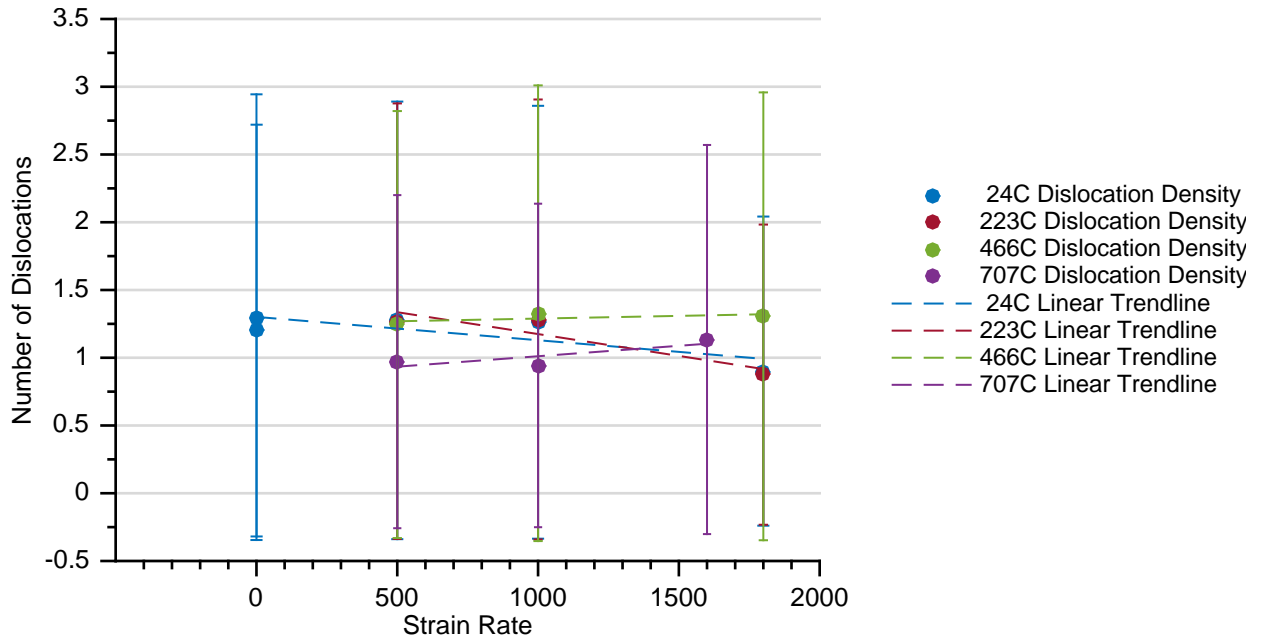


Figure 60. Average normalized dislocation density in the pre-necked zone for all strain rates and temperature conditions, where each point is the average of two difference EBSD scans

Figure 60 shows that the trend switches from negative with increases strain rate for 24°C and 223°C, to neutral at 466°C and then positive at 707°C. Then as temperature increases, the dislocation density increases until 707°C, where the density drops.

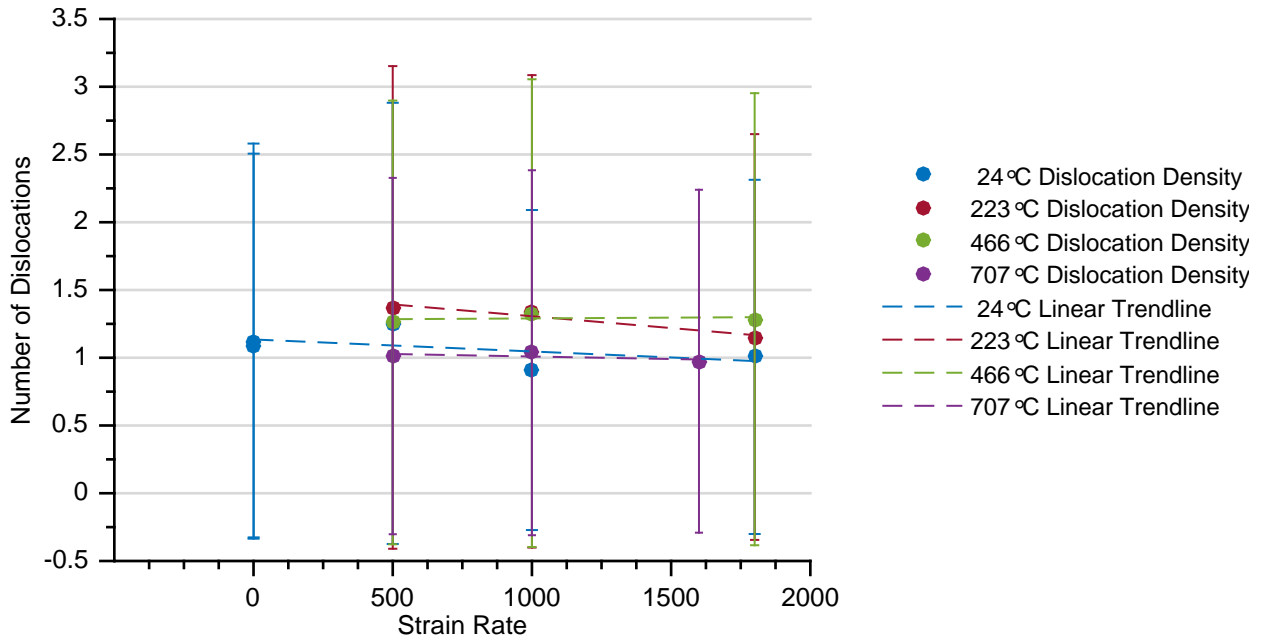


Figure 61. Average normalized dislocation density in the fracture zone for all strain rates and temperature conditions, where each point is the average of four difference EBSD scans

Again we see grouped behaviors. The room temperature and the 707°C results are all grouped together, but there is an increase with 223°C and 466°C temperatures. Strain rate does not appear to have a significant impact on the trends except for perhaps the 223°C group, where there is a decreasing trend.

The final materials feature measured is stiffness. The normalized results are shown in Figures 62 and 63.

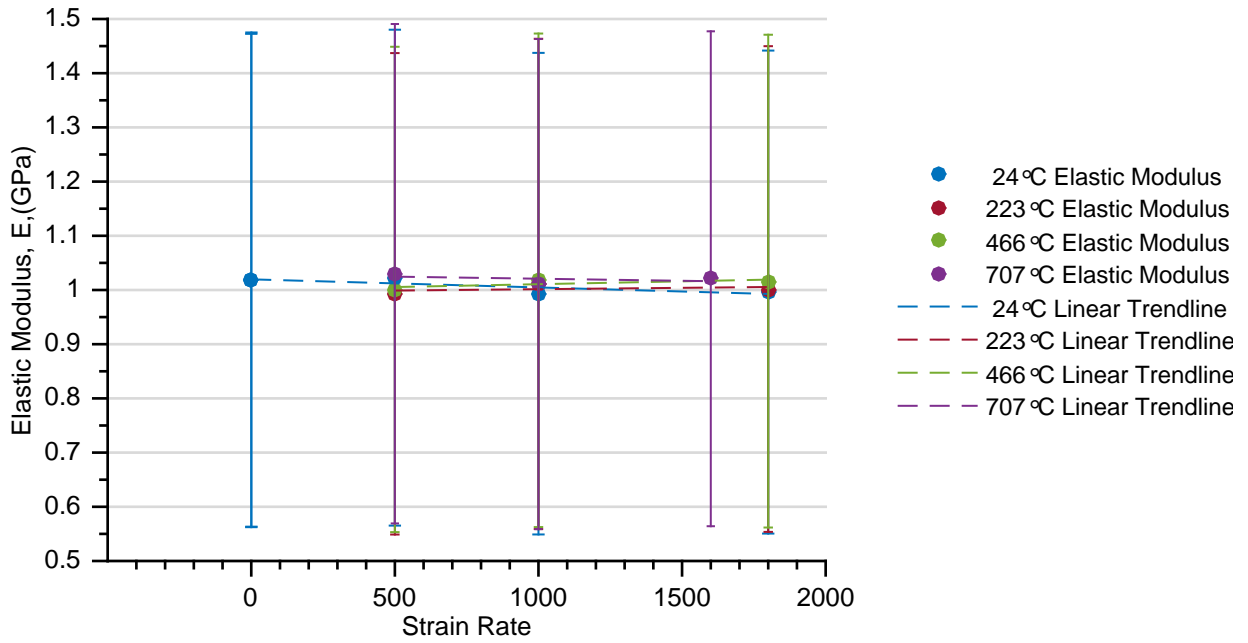


Figure 62. Average normalized stiffness in the pre-necked zone for all strain rates and temperature conditions, where each point is the average of four difference EBSD scans

All of the results are almost all consistent - there is little variation between the strain rate and temperature changed.

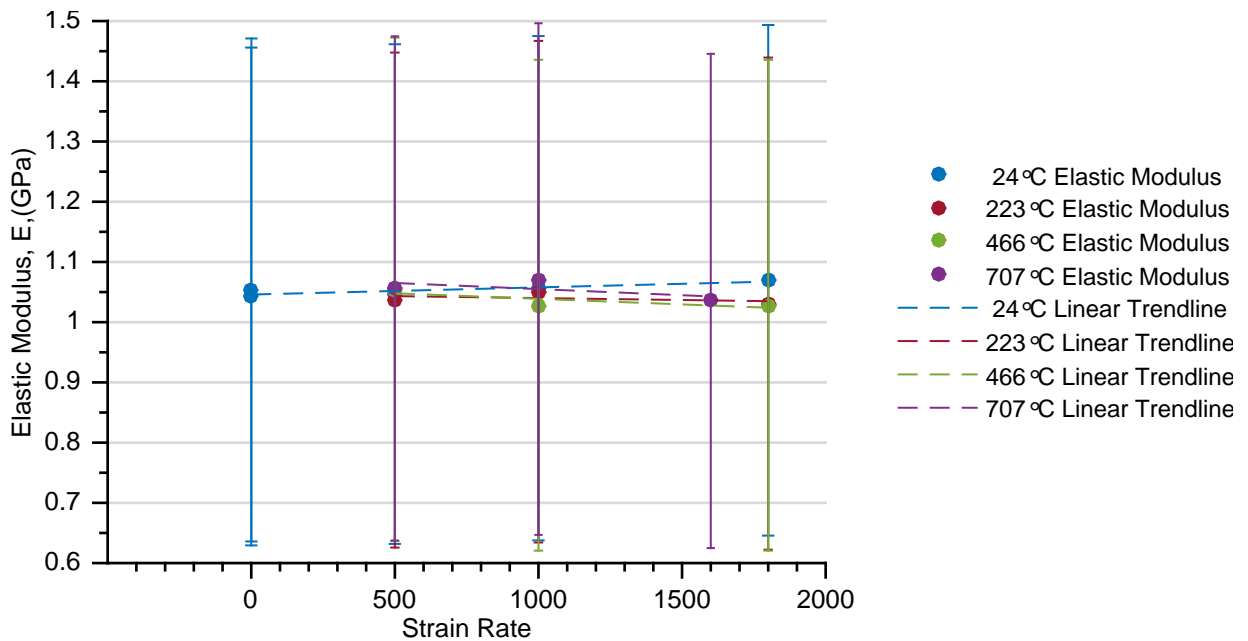


Figure 63. Average normalized stiffness in the fracture zone for all strain rates and temperature conditions, where each point is the average of four difference EBSD scans

Again, all of the results are almost all consistent with little variation between the strain rate and temperature changes.

The initial observations of the trends present in the collected failure microstructural data has been addressed. The raw data will be available in electronic format as an attachment. It is of interest to know whether any of these observed trends are statistically significant. To discern this, a tool known as the analysis of variance (ANOVA) is used. It is outlined in the next chapter.

VI. Statistical Analysis

6.1 Statistical Analysis

The next challenge is to ascertain if any relevant conclusions can be made. Trends have been observed from the data analysis, but is it coincidence, or is any of it significant? There is a statistical tool designed to manipulate large sets of data which can be utilized to help us make these determinations.

In the 1920s, statistician Sir Ronald Aylmer Fisher developed the analysis of variance method, or ANOVA, to analyze a particularly large set of data: genetic crop data collected since the 1840s [83]. The general idea of the method is that if there are true differences between the groups of data at different conditions, the measured variance between the groups will exceed the error variance within the groups [84]. The analysis method has evolved to be flexible depending on the conditions of the experiment, utilizing a different model for different conditions. Depending on the design of the experiment, there are generally three different models to choose from: a fixed-effects model, a random-effects model, or a mixed-effects model [85].

Before jumping into the models, it is of interest to define some terminology used for ANOVA. When taking experimental data, there are subjects which are all tested for an expected value. There can be multiple subjects, tested many times, and at different experimental conditions. Each experimental condition being tested is known as a treatment, and each variation of the treatment is known as a level. For example, in our case, we have several subjects (metal samples) being tested for two different treatment effects - strain rate and temperature. Each of these treatments has several different levels that were being observed: for the dynamic strain rates, there were low, medium and high levels of 500, 1000, and 1800/s. For temperature, there were room, mid-low, mid-high, and high level temperatures. Every measured response of

a subject is a replicate, so each scan of a sample at the same condition is a replicate. There are two replicates for pre-necked readings, and four replicates for the fracture readings. Now that terminology is established, we can jump into the different models.

A fixed-effects model is one where the independent variable, or treatments, in the experiment all have set values - there are specific levels (ex: low, medium, high) which always are the same [86]. A random-effects model is one where there are no set values for the treatment. They are all different, but at no specified intervals [86]. A mixed-effects model is just what it sounds like, a mix of the two models where some treatments are fixed, but others are random [87]. This also opens up the possibility for analysis of variance between subjects, and variance within subjects.

The number of treatments also defines the analysis procedure for an ANOVA analysis - if there is only one treatment being applied, a one-way ANOVA analysis is sufficient. However if there are multiple treatments (2+), a two-way ANOVA analysis needs to be used.

The model that should be used for analysis depends on the data that is collected. Looking at the data for this experiment, one sample from each experimental condition where temperature and strain rate, scanned it four times at two different magnifications in random locations. The model chosen for use is dependent on the assumptions made in this analysis. It was assumed that the magnification does not matter and the location scanned is unimportant thus, a two-way ANOVA analysis using the fixed effects model is appropriate.

For an ANOVA analysis to be valid for a two-way fixed-effects model, there are 6 assumptions that need to be checked before proceeding:

1. The dependent variables must be continuous
2. There must be at least two independent variables
3. There is an independence of observations

4. There are no significant outliers
5. The dependent variables must be normally distributed
6. There needs to be homogeneity of variances

A continuous variable is defined as one that can take on any value between its minimum and maximum value [88]. All of our dependent variables are continuous, and there are two independent variables, so there are no issues with the first two checks. The measurements are taken in different locations on the sample, so they are independent, meeting our third check. The final three assumptions can be easily checked using statistical analysis software. Minitab was used to run a check for outliers, data outside of three standard deviations of the mean of the dataset [89]. Probability plots were run to check for normality, and then the check for the homogeneity of variances was run to see if the variation between measurements is the same. It is not terribly unusual for collected data sets to fail some of these last three tests, but in that case, data transformations can help get things in order. Some examples of different transformations that can be applied are listed below:

- Squaring the data
- Taking the reciprocal
- Square root
- Log transformation
- Reciprocal of the square root
- Reciprocal of the square
- Box-Cox transformation
- Johnson transformation

When running checks on the data taken, any outliers identified were removed from analysis. Not all data met the normality and homogeneity assumptions, so there were some transformations that needed to be made. In all cases, the Johnson transformation produced the best results for normality and homogeneity of variances.

From the Minitab documentation: “Johnson transformation optimally selects a function from three families of distributions of a variable, which are easily transformed into a standard normal distribution. These distributions are labeled as S_B , S_L , and S_U , where B, L, and U refer to the variable being bounded, lognormal, and unbounded. [89]”

Jones gives a nice summary of the transformation in his summary for MATLAB. “Johnson (1949) developed a flexible system of distributions, based on three families of transformations, that translate an observed, non-normal variate to one conforming to the standard normal distribution. The exponential, logistic, and hyperbolic sine transformations are used to generate log-normal (SL), unbounded (SU), and bounded (SB) distributions, respectively. The coefficients defining a Johnson distribution consist of two shape (γ , δ), a location (ξ), and a scale (λ) parameter. This allows a unique distribution to be derived for whatever combination of mean, standard deviation, skewness, and kurtosis [(how sharp or flat the peak of a distribution is)] occurs for a given set of observed data. Once a variate is appropriately transformed, probability densities and percentage points may be derived based on the standard normal curve [90].”

Of our data, the pre-necked region dislocation density and misorientation both needed to have a transformation performed. The resulting fits and data are shown below in Figures 64, 65, 66, and 67, and in Tables 13 and 14.

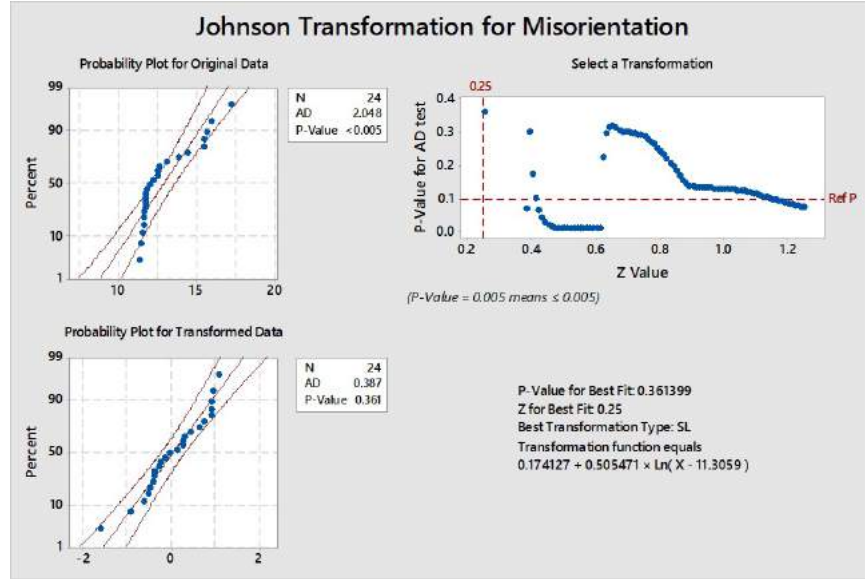


Figure 64. Johnson Transformation of the misorientation angle in the pre-necked region

At the top left of Figure 64, the original distribution is plotted in a probability plot, plotting the percentage of data points vs the value overlayed on top of a predicted normal distribution. For a distribution to be considered normal, the p-value, the calculated probability, must be greater than 0.05 for a 95% confidence fit. The data in the original distribution falls outside of the lines of the normal probability test, and the p-value is less than 0.05, indicating a non-normal distribution. On the right hand side, the Johnson distribution is applied. The transformation type selected is the SL function, and the transformation equation comes out to:

$$MIS_{Flow,T} = 0.174127 + 0.505471 \times \ln(MIS_{Flow} - 11.3059) \quad (69)$$

where $MIS_{Flow,T}$ is the transform of the misorientation data from the pre-necked region and MIS_{Flow} is the original, non-normal misorientation data in the pre-necked region, also represented as “X” in Minitab.

The improved fit is seen on the bottom left corner. With a p-value of 0.361, the distribution is now normal.

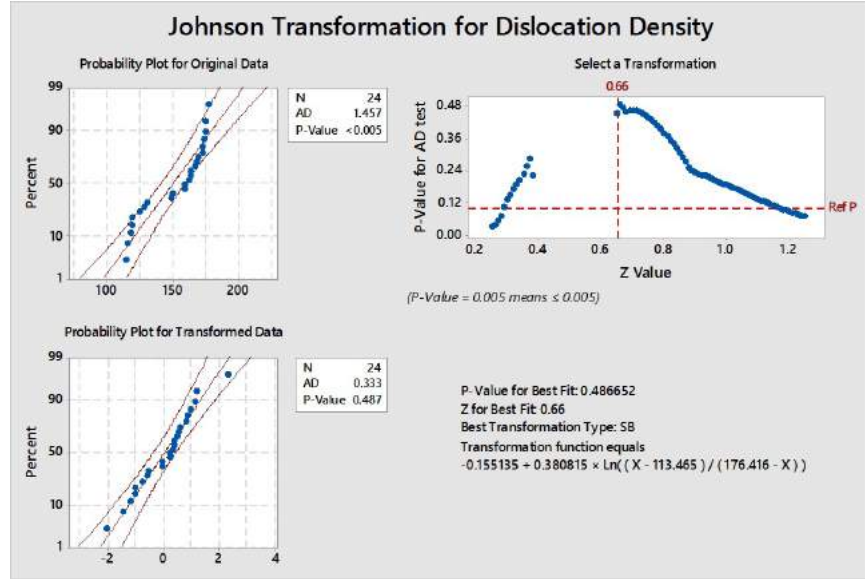


Figure 65. Johnson Transformation of the dislocation density in the pre-necked region

The transformation type selected for the dislocation density shown in Figure 65 is the SB function, and the transformation equation comes out to:

$$DIS_{Flow,T} = -0.155135 + 0.380815 \times \ln((DIS_{Flow} - 113.465)/(176.416 - X)) \quad (70)$$

where $DIS_{Flow,T}$ is the transform of the misorientation data from the pre-necked region and DIS_{Flow} is the original, non-normal misorientation data in the pre-necked region, also represented as “X” in Minitab.

The improved fit is seen on the bottom left corner. With a p-value of 0.487, the distribution is now normal. The new distributed values are shown in Table 13.

Table 13. EBSD Measurements of the pre-necked zones of dynamically-impacted heat treated 4130 steel

Sample Number	Dislocation Density (Number) (Johnson Transformation)	Misorientation (Degrees) (Johnson Transformation)
25E	0.48342	-0.50177
25E	0.53747	-0.51979

Table 13. EBSD Measurements of the pre-necked zones of dynamically-impacted heat treated 4130 steel

Sample Number	Dislocation Density (Number) (Johnson Transformation)	Misorientation (Degrees) (Johnson Transformation)
4E	0.82415	-0.29527
4E	0.19808	-0.62178
8E	-1.20271	0.23969
8E	-1.06102	0.28241
29E	1.09947	-0.42544
29E	0.19283	-0.92802
13E	1.15865	-0.37778
13E	0.28829	0.25154
10E	-2.06736	0.91550
10E	-1.48308	0.44279
31E	0.35083	-0.37853
31E	0.33541	0.10933
18E	2.30990	-0.26366
18E	0.79589	-1.60698
37E	0.59011	-0.05838
37E	0.97536	-0.16773
34E	-0.74768	0.94631
34E	-0.55119	0.88980
40E	-0.60981	0.88546
40E	-1.05283	1.06646
43E	-0.08135	0.73982
43E	-0.05293	0.63997

In the fracture region, the grain size and the dislocation density both had non-normal distributions and needed to be transformed. The results are shown in the figures below:

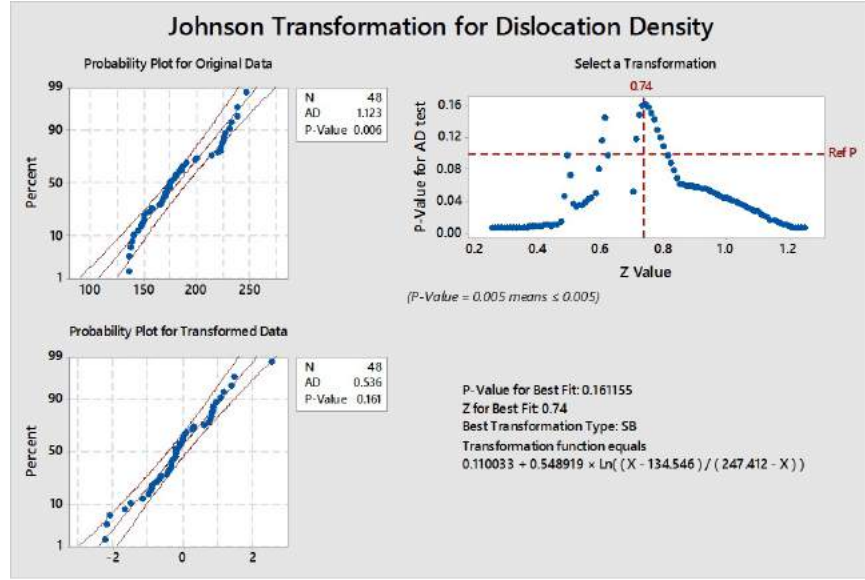


Figure 66. Johnson Transformation of the dislocation density in the failed region

The transformation type selected for the dislocation density shown in Figure 66 is the SB function, and the transformation equation comes out to:

$$DIS_{Frac,T} = 0.110033 + 0.548919 \times \ln((DIS_{Frac} - 134.546)/(247.412 - X)) \quad (71)$$

where $DIS_{Frac,T}$ is the transform of the misorientation data from the fracture region and DIS_{Frac} is the original, non-normal misorientation data in the fracture region, also represented as “X” in Minitab.

The improved fit is seen on the bottom left corner. With a p-value of 0.161, the distribution is now normal.

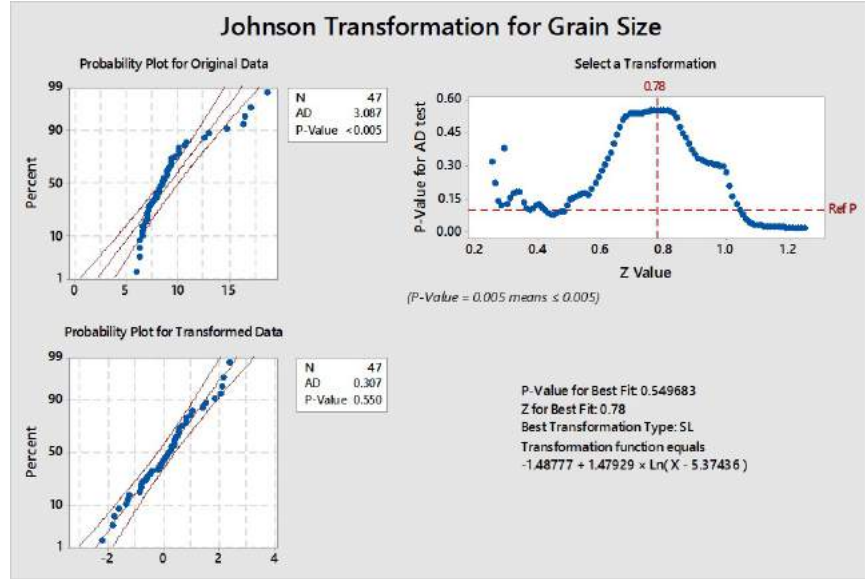


Figure 67. Johnson Transformation of the grain size in the failed region

For grain size, the transformation type selected is the SL function, and the transformation equation comes out to:

$$GS_{Frac,T} = 1.48777 + 1.47929 \times \ln(GS_{Frac} - 5.37436) \quad (72)$$

where $GS_{Frac,T}$ is the transform of the misorientation data from the fracture region and GS_{Frac} is the original, non-normal misorientation data in the fracture region, also represented as “X” in Minitab.

The improved fit is seen on the bottom left corner. With a p-value of 0.550, the distribution is now normal.

The new distributed values are shown in Table 14.

Table 14. EBSD Measurements of the pre-necked zones of dynamically-impacted heat treated 4130 steel

Sample number	Dislocation Density (Number) (Johnson Transformation)	Grain Size(μm) (Johnson Transformation)
25F	-0.36790	0.78654

Table 14. EBSD Measurements of the pre-necked zones of dynamically-impacted heat treated 4130 steel

Sample number	Dislocation Density (Number) (Johnson Transformation)	Grain Size(μm) (Johnson Transformation)
25F	-0.23615	-0.76560
25F	0.86298	0.23607
25F	0.78066	0.40752
4F	-2.21699	1.51184
4F	-2.11935	0.17581
4F	-0.91767	0.10605
4F	-0.92921	-0.50494
8F	-0.43063	2.05850
8F	-2.22047	*
8F	-0.38480	0.98614
8F	-0.46210	2.04943
29F	-0.21497	0.03576
29F	1.14638	-0.26443
29F	0.86295	0.22579
29F	1.04367	0.37874
13F	-0.00218	-1.35502
13F	-0.04957	-0.63653
13F	1.38312	-1.80661
13F	1.44799	-1.83234
10F	-0.65133	2.34000
10F	-0.33944	1.81997
10F	0.28299	2.13839

Table 14. EBSD Measurements of the pre-necked zones of dynamically-impacted heat treated 4130 steel

Sample number	Dislocation Density (Number) (Johnson Transformation)	Grain Size(μm) (Johnson Transformation)
10F	0.26019	-0.00361
31F	-0.30523	-0.05845
31F	-0.09986	0.53690
31F	0.80556	0.97375
31F	0.70426	0.50483
18F	0.06811	0.76592
18F	-0.23491	0.77759
18F	2.54209	-0.14918
18F	0.92632	0.16354
37F	-0.01412	0.61500
37F	0.01504	0.52698
37F	0.81442	0.46786
37F	0.57682	1.40467
34F	-1.15351	-1.25549
34F	-1.53068	-0.47994
34F	-0.15415	-1.31986
34F	-0.23279	-0.81999
40F	-1.01590	-2.20968
40F	-0.78815	0.33173
40F	-0.27916	0.37683
40F	-0.11394	-0.88049
43F	-0.94612	-0.12746

Table 14. EBSD Measurements of the pre-necked zones of dynamically-impacted heat treated 4130 steel

Sample number	Dislocation Density (Number) (Johnson Transformation)	Grain Size(μm) (Johnson Transformation)
43F	-1.67446	-0.66842
43F	-0.69839	-0.84896
43F	-0.33924	-1.63951

* Outlier - excluded from analysis

Once all of these assumptions have been met, the ANOVA analysis can be performed. ANOVA compares the variances caused by each factor or interaction of factors. The hypothesis that is being tested is that all of the variances are essentially equal, and that no one factor is dominating. The important figures of interest to test this idea are the mean, the sum of squares of the variables, the mean sum square, and the F-statistic of each term. These are all calculated for each of the treatments, interaction between treatments, and the error associated between all of the measurements. Mathematically, this is represented for the fixed-effects model as:

$$Y_{ijk} = \mu + A_i + B_j + AB_{ij} + \epsilon_{ijk} \quad (73)$$

where Y_{ijk} is the expected value of the observation, μ is the overall average, A_i is a fixed treatment effect (Temperature), B_j is the other fixed treatment effect (Strain Rate), AB_{ij} is the interaction effect of both treatments, and ϵ_{ijk} is the random error [86]. The effect of each treatment are deviations from the overall mean. “i” is the index value for the levels of the temperature treatment, of which there are a total number of “a” (24°C, 223°C, 466°C, 707°C, so $a = 4$) “j” is the index value for the levels of the strain rate treatment, of which there are a total number of “b” (500/s,

1000/s, and 1800/s so $b = 3$) The total number of measurement replicates is represented as “n”, which for this experiment is 4 for the fracture regions (4 measurements made on 12 different samples) or two for the pre-necked regions, and is indexed by “k”. The hypothesis of the model is that the different treatments effects will have no effect on the mean. Applying this to Equation 73, it would mean that the sum of A_i , B_j , and AB_{ij} are zero, as shown below [86].

$$\sum_{i=1}^a A_i = 0 \quad (74)$$

$$\sum_{j=1}^b B_j = 0 \quad (75)$$

$$\sum_{i=1}^a AB_{ij} = \sum_{j=1}^b AB_{ij} = 0 \quad (76)$$

The overall objective of ANOVA is to calculate the F-statistic for comparative purposes. To get to this number, the sum of squares, degrees of freedom, and mean sum squares must be calculated. The necessary calculations are summarized in Table 15, and expanded on in the following sections.

Table 15. ANOVA calculations for a two-way, fixed effects model. An example calculation is shown in Appendix 9.2

Source of Variation	Sum of Squares	Degrees of Freedom	Mean Square	F_0
A (Temperature)	SS_A	$a - 1$	$MS_A = \frac{SS_A}{a-1}$	$F_{A0} = \frac{MS_A}{MS_E}$
B (Strain Rate)	SS_B	$b - 1$	$MS_B = \frac{SS_B}{b-1}$	$F_{B0} = \frac{MS_B}{MS_E}$
AB (Interaction)	SS_{AB}	$(a - 1)(b - 1)$	$MS_{AB} = \frac{SS_{AB}}{(a-1)(b-1)}$	$F_{AB0} = \frac{MS_{AB}}{MS_E}$
Error	SS_E	$ab(n - 1)$	$MS_E = \frac{SS_E}{ab(n-1)}$	
Total	SS_T	$abn - 1$		

Our first goal is calculating the sum of squares for each of our factors. The sum of squares is defined as the sum of squared deviations of the factor means about the overall mean. These are calculated for all factors: Temperature, Strain Rate, the interaction, the error, and the experiment total. Mathematically, this is expressed:

$$SS_A = \frac{1}{bn} \sum_{j=1}^b \sum_{k=1}^n y_{i..}^2 - \frac{y_{...}^2}{abn} \quad (77)$$

$$SS_B = \frac{1}{an} \sum_{i=1}^a \sum_{k=1}^n y_{.j.}^2 - \frac{y_{...}^2}{abn} \quad (78)$$

$$SS_{AB} = \frac{1}{n} \sum_{i=1}^a \sum_{j=1}^b y_{ij.}^2 - \frac{y_{...}^2}{abn} - SS_A - SS_B \quad (79)$$

where

$$y_{...} = \sum_{i=1}^a \sum_{j=1}^b \sum_{k=1}^n y_{ijk} \quad (80)$$

$$y_{i..} = \sum_{j=1}^b \sum_{k=1}^n y_{ijk} \quad (81)$$

$$y_{.j.} = \sum_{i=1}^a \sum_{k=1}^n y_{ijk} \quad (82)$$

$$y_{ij.} = \sum_{k=1}^n y_{ijk} \quad (83)$$

The total sum of squares is the sum of all of the sum of squares, or:

$$SS_T = \sum_{i=1}^a \sum_{j=1}^b \sum_{k=1}^n y_{ijk}^2 - \frac{y_{...}^2}{abn} \quad (84)$$

Finally the sum of squares for the error is:

$$SS_E = SS_T - SS_{AB} - SS_A - SS_B \quad (85)$$

The remainder of the calculations follow quite easily from those shown in Table 15.

The degree of freedom of each factor is found for each of the main effect treatments by subtracting one. The degrees of freedom for the interaction term are the number of degrees of freedom for each cell (each combination of temperature/strain rate, so in this case, $ab - 1$) minus the number of degrees of freedom for each of the main effects. Finally, for the degrees of freedom for error. Within the cells, there are $n - 1$ degrees of freedom between the n replicates. Thus, there are $ab(n - 1)$ degrees of freedom within the subjects. The total degrees of freedom is simply the sum of all the calculated degrees of freedom, or alternatively, $abn - 1$.

Next one calculates the mean square by dividing the sum of squares by the appropriate degree of freedom. For factor A, this looks like:

$$MS_A = \frac{SS_A}{a - 1} \quad (86)$$

Following the mean square calculation, the F statistic is calculated. This is the ratio of mean sum of squares of the treatment or interaction factor compared to the error. For treatment A, this looks like:

$$F_{A0} = \frac{MS_A}{MS_E} \quad (87)$$

This number is the one that will be used for a comparative factor to determine if the factor is statistically significant. One can manually use the degrees of freedom and a chosen confidence level to look up a comparative F factor using F-sampling distribution table, usually found in the back of statistics books [91]. If the table value of F is less than the calculated F value, the hypothesis is rejected and the factor is significant. If this is done via computer analysis, a p value is calculated for comparison rather than looking up a table value. This p-value is the probability that the table F value would be larger than the calculated F value. If the p value is less than the confidence interval chosen (for a 95% confidence level, 0.05), then the hypothesis is rejected, and the factor is statistically significant. For an example of how these calculations work in action, see Appendix D.

The above calculations have all been carried out for each of the micromechanical variables of interest using MiniTab. The calculated tables are presented in Tables 16-23. Where factors are determined to be statistically significant, the main effects plots, showing how each factor varies against the mean of the measurements from Tables 11, 12, 13, and 14 as applicable. The interaction plot, showing how the average of each condition's mean measurement (again taken from the same tables) changes with both effects included will be briefly addressed and discussed in further detail in the following section.

Table 16. Grain Size ANOVA for the pre-necked region of dynamically-impacted 4130 steel

Source	DF	SS	MS	F	P
Temperature	3	1.749	0.5828	2.48	0.107
Strain Rate	2	1.728	0.8640	3.68	0.054
Error	13	3.054	0.2349		
Lack of Fit	4	2.003	0.2628	1.18	0.382
Pure Error	9	2.003	0.2225		
Total	18	6.704			

The grain size analysis results in the pre-necked region are shown in Table 16. Looking at the p-values for the temperature and strain rate, which are 0.107 and 0.054, both are too large to reject the null hypothesis for a 95% confidence interval. However, if a 90% confidence interval were considered, strain rate would be an impacting factor on the grain size measurement.

The grain size ANOVA results from the fracture region are shown in Figure 17.

Table 17. Grain Size ANOVA for the fracture region of dynamically-impacted 4130 steel

Source	DF	SS	MS	F	P
Temperature	3	16.22	5.4072	11.30	0.000
Strain Rate	2	10.48	5.2385	10.95	0.000
Interaction	6	12.89	2.1486	4.49	0.002
Error	35	16.75	0.4785		
Total	46	54.95			

For the fracture region, the grain size is affected by the temperature and strain rate, and the interaction effects. The main effects are shown in the Figure 68.

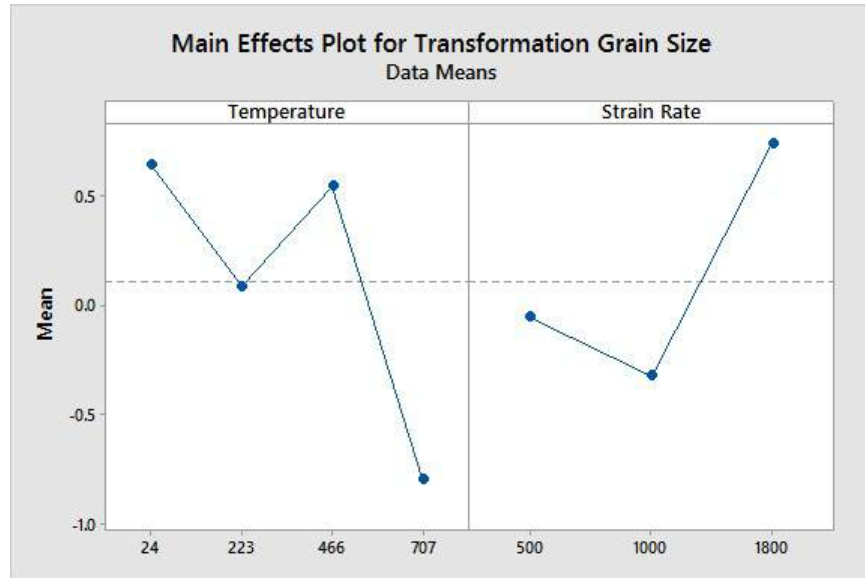


Figure 68. Main Effects plot for the grain size of the fracture region

The trend for grain size is decreases with increasing temperature, and increases with increasing strain rate. The interaction effects are shown in Figure 69.

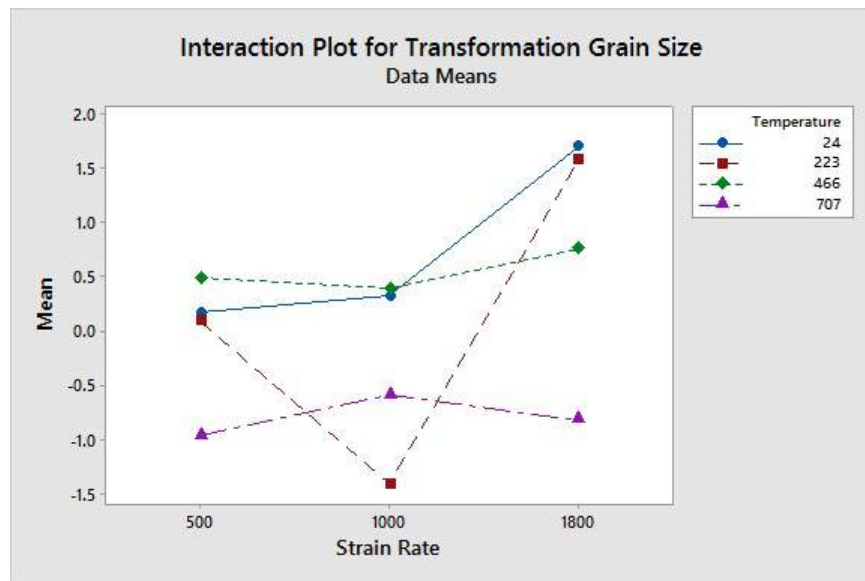


Figure 69. Main Effects plot for the grain size of the fracture region

There is a strong interactions between 707°C and 223°C. 707°C has an opposite trend compared to the other three temperatures.

The ANOVA results for the misorientation measurements for the pre-necked region in Table 18.

Table 18. Misorientation ANOVA for the pre-necked region of dynamically-impacted 4130 steel

Source	DF	SS	MS	F	P
Temperature	3	5.654	1.8848	14.68	0.000
Strain Rate	2	1.281	0.6407	4.99	0.026
Interaction	6	2.277	0.3794	2.96	0.052
Error	12	1.541	0.1284		
Total	23	10.753			

The misorientation in the pre-necked zone is impacted by the temperature and the strain rate, but not the interaction of the two. The strain rate main effects plot is shown in Figure 70.

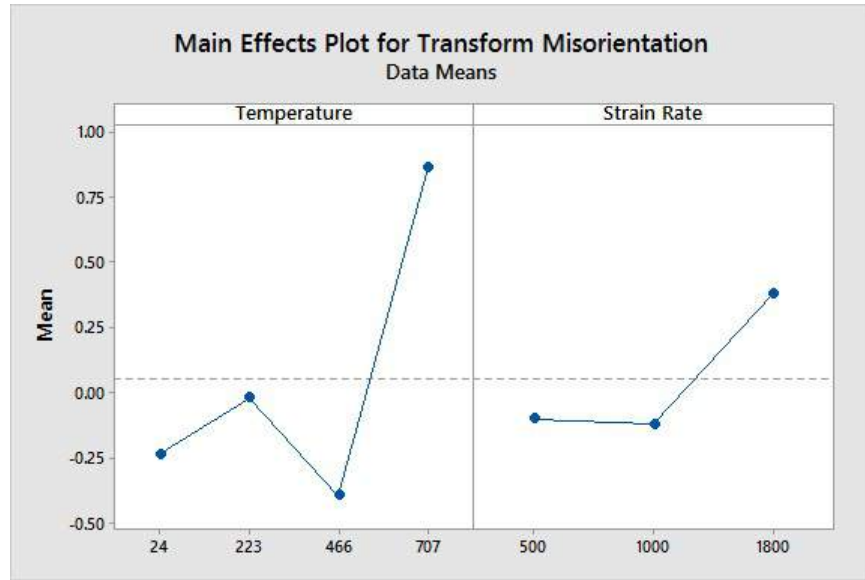


Figure 70. Main Effects plot for the misorientation of the pre-necked region

Overall, the misorientation increases with increasing temperature (with the exception of 466°C), and increases with increasing strain rate.

The ANOVA results for the misorientation measurements in the fracture region are shown in Table 19.

For misorientation, temperature, strain rate, and the interaction are all statistically significant effects on the resulting measurement as all of their p-values are below 0.05. The main effects plot is shown in Figure 71.

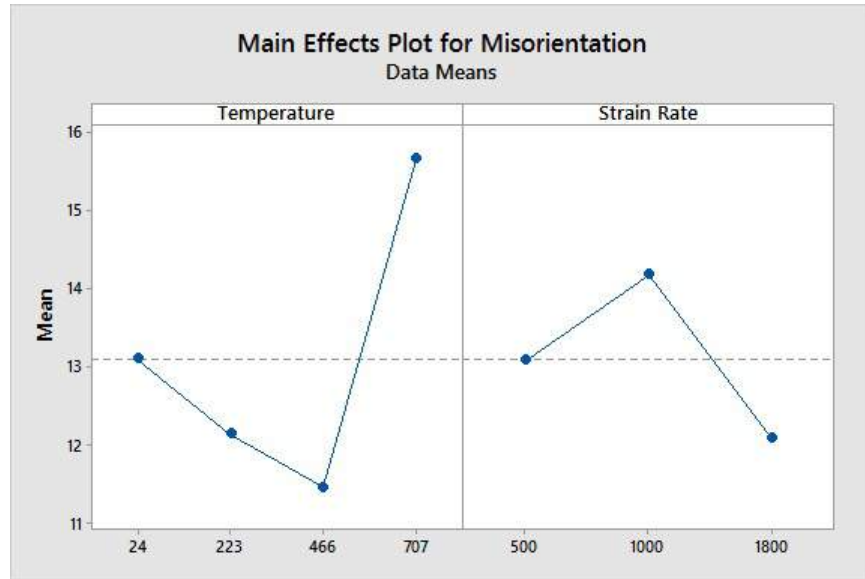


Figure 71. Main Effects plot for the misorientation of the pre-necked region

The temperature is lowering the misorientation until the highest temperature, where it jumps significantly. The interaction effects are shown in the Figure 72.

Table 19. Misorientation ANOVA for the fracture region of dynamically-impacted 4130 steel

Source	DF	SS	MS	F	P
Temperature	3	122.21	40.737	29.60	0.000
Strain Rate	2	38.24	19.118	13.89	0.000
Interaction	6	46.77	7.795	5.66	0.000
Error	35	48.16	1.376		
Total	46	250.23			

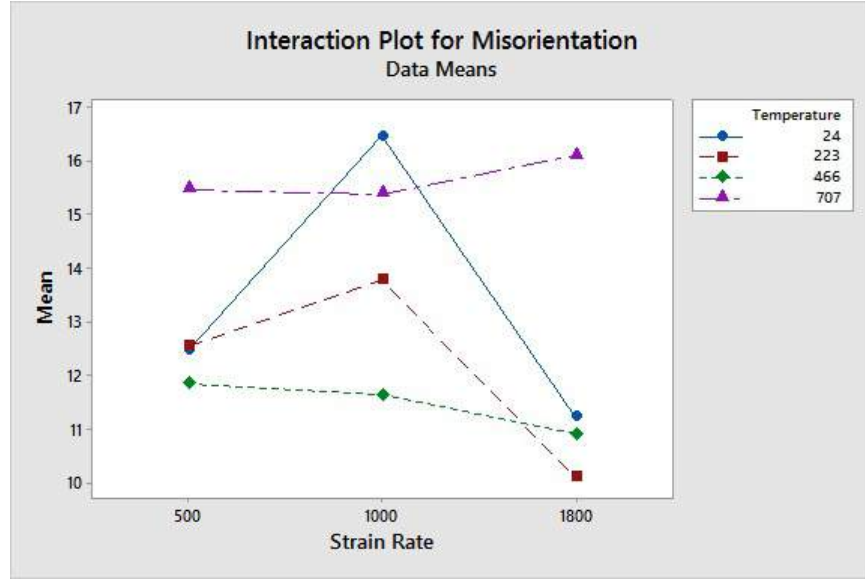


Figure 72. Interaction plot for the misorientation of the fracture region

The interaction effects shows that for the first three temperatures, the trend is an inverted V, but for the highest temperature the trend reverses and is a regular "v" shape.

Th dislocation density measurements are given next. The ANOVA results for the pre-necked region are shown in Table 20

Table 20. Dislocation Density ANOVA for the pre-necked region of dynamically-impacted 4130 steel

Source	DF	SS	MS	F	P
Temperature	3	6.436	2.1453	10.27	0.001
Strain Rate	2	4.613	2.3065	11.04	0.002
Interaction	6	9.197	1.5328	7.34	0.002
Error	12	2.506	0.2089		
Total	23	22.752			

The temperature, strain rate, and interaction effects are all statistically significant for the dislocation density in the pre-necked region. The main effects are shown in

Figure 73.

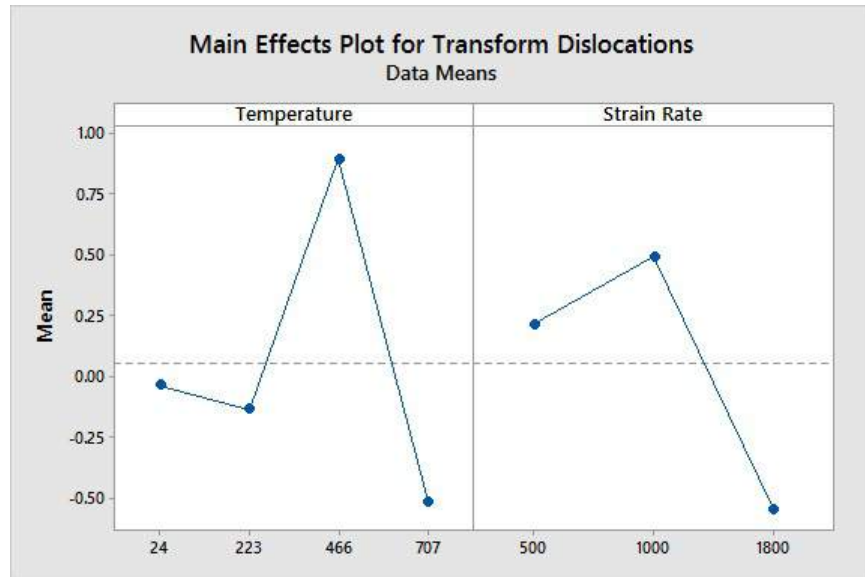


Figure 73. Main Effects plot for the dislocation density of the pre-necked region

Misorientation decreases with increasing temperature with the notable exception of 466°C, where it spikes dramatically. Strain rate increases through 1000/s until a certain threshold is reached and it drops at 1800/s. The interaction effects are shown in Figure 74.

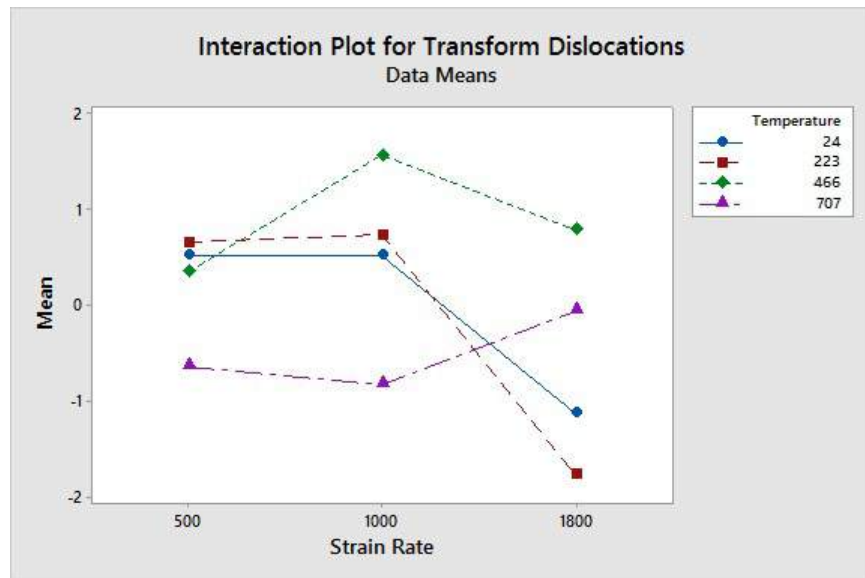


Figure 74. Main Effects plot for the dislocation density of the pre-necking region

Between 500 and 1000/s, temperature seems to be the driving factor that is changing the dislocation density with the exception of 466°C. After 1000/s, there seems to be strong interaction effects between 707°C and 466°C and 24°C.

The dislocation density in the fracture region is shown next. The ANOVA results are shown in Table 21.

Table 21. Dislocation Density ANOVA for the fracture region of dynamically-impacted 4130 steel

Source	DF	SS	MS	F	P
Temperature	3	16.985	5.6617	11.23	0.000
Strain Rate	2	2.063	1.0314	2.05	0.144
Interaction	6	7.352	1.2254	2.43	0.045
Error	36	18.143	0.5040		
Total	47	44.543			

For the dislocation density in the fracture region, the temperature and interaction effects are both significant. The main effects are plotted in Figure 75.

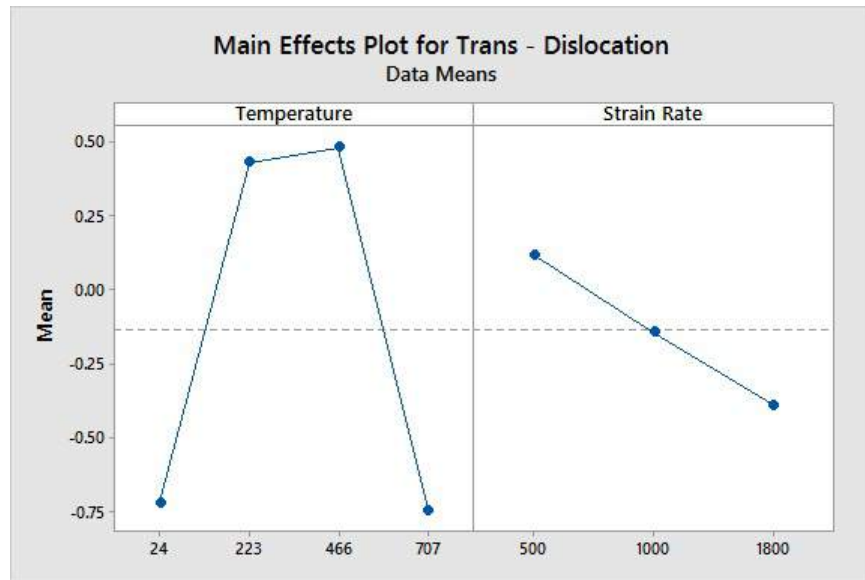


Figure 75. Main Effects plot for the dislocation density of the fracture region

For the temperature effects, there is an increase that peaks at 466°C, then drops back down at 707°C. The interaction effects are shown in Figure 76.

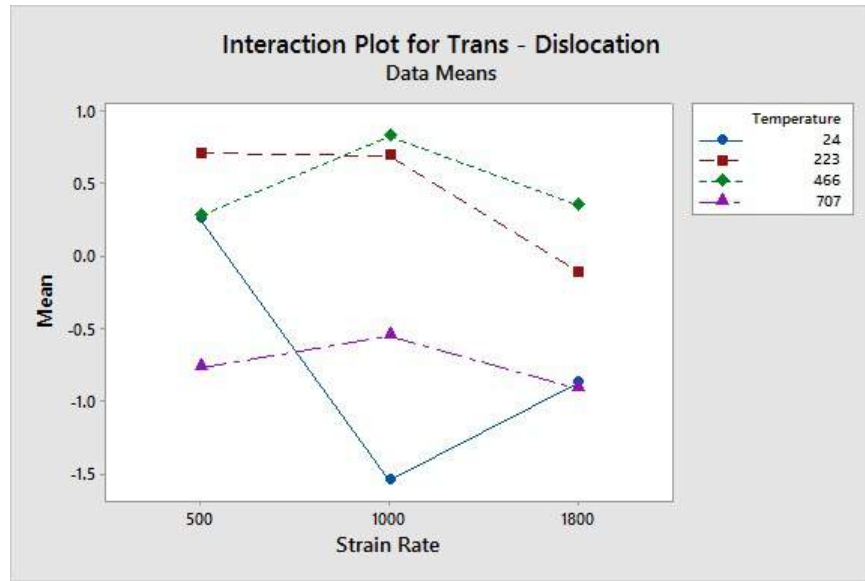


Figure 76. Interaction Effects plot for the dislocation density of the fracture region

At the interaction level, there is a "v" shape for the 24°C for the strain rate effect, which inverts for higher temperature. Overall the temperature and increases the dislocations until the highest temperature, 707°C.

The next observed variable is the elastic modulus, or measured stiffness in the pre-necked region. The ANOVA results are shown in Table 22.

Table 22. Stiffness (elastic modulus) ANOVA for the pre-necked region of dynamically-impacted 4130 steel

Source	DF	SS	MS	F	P
Temperature	3	39.263	13.0876	2.07	0.157
Strain Rate	2	1.666	0.8331	0.13	0.878
Interaction	6	62.921	10.4869	1.66	0.214
Error	12	75.75	6.3121		
Total	23	179.596			

Based on the p-values of 0.157 for temperature, 0.878 for strain rate, and 0.214 for the interaction effects, no factors are significant for the prediction of the elastic modulus in the pre-necked region.

Table 23. Stiffness (elastic modulus) ANOVA for the fracture region of dynamically-impacted 4130 steel

Source	DF	SS	MS	F	P
Temperature	3	109.74	36.58	2.04	0.127
Strain	2	29.02	14.51	0.81	0.454
Interaction	6	159.86	26.64	1.48	0.212
Error	34	610.14	17.95		
Total	45	909.32			

Again, there is no statistical significance for either the temperature, strain rate, or interaction effect.

The results of all of the ANOVA analyses are summarized in Tables ?? and ?? for the pre-necked and fracture region analyzes respectively. The tables note whether the factor was “significant,” or, whether the p-value was below 0.05, or if the factor did not have an impact (“No” in the table).

Table 24. Summary: Elastic Section ANOVA Results

Variable	Temperature	Strain Rate	Interaction
Grain Size	No	No	No
Misorientation	Significant	Significant	No
Dislocation Density	Significant	Significant	Significant
Stiffness	No	No	No

We can conclude that for the pre-necked region measurements, neither the grain

size nor the elastic modulus was impacted by the strain rate, temperature, or interaction effects. The misorientation was impacted by temperature and strain rate, but not the interaction effects, and misorientation angle was impacted by all of the factors.

The results of all of these ANOVA analyses are summarized in the following table:

Table 25. Summary: Fracture Section ANOVA Results

Variable	Temperature	Strain Rate	Interaction
Grain Size	Significant	Significant	No
Misorientation	Significant	Significant	Significant
Dislocation Density	Significant	No	Significant
Stiffness	No	No	No

We can conclude that for the fracture region measurements, the elastic modulus was not impacted by the strain rate, temperature, or interaction effects. Grain size was impacted by temperature and strain rate factors, the misorientation angle was impacted by temperature strain rate and interaction effects, and dislocation density was impacted by temperature and the interaction effects.

6.2 Discussion

In the prior section, the factors that impact micromechanical features were identified by their statistical significance. However, looking at the main effects and interaction plots, the effects from the factors are not as straightforward as “temperature always increases the result” or “strain rate always decreases the result.” The following discussion is an attempt to look at what is happening with each of the effects.

Grain size does not seem to be impacted by the experimental factors until it enters the failure zone, where the temperature and strain rate are significant, but

the interaction is not. The misorientation is affected by temperature and strain rate in both the pre-necked zones and the fracture zones, but in the fracture zone the interaction becomes important as well. The dislocation density is effected by all of the factors and interactions except for the strain rate in the failure region. While the stiffness is not affected by any factor in either the failure or the pre-necked regions.

For the grain size, usually at least temperature would have an impact on the size. However, this was a case where there were many outliers, so this result should be re-checked after taking additional readings. But in the fracture zone, grain size changes correlated to both strain rate and temperature, and not the interaction. Strain rate actually seemed to increase the size – perhaps as the pulse goes through, the grains fracture more at boundaries rather than shattering grains themselves. The temperature also shows a decreasing grain size, which is interesting. It might be a sign that dynamic recrystallization is allowing the formation of smaller grains along the grain boundaries, and it would appear the effect is maximized at higher temperatures.

For the main effects of the misorientation, the strain rate has an opposite effect at the pre-necked region than in the fracture region. For fracture, there must be a certain threshold of strain rates where the change in misorientation hits its maximum. For the temperature, at 223°C there is a feature of being in the failure zone that makes the misorientation decrease opposed to increase.

The pre-necked region has dislocation densities that are impacted by temperature, strain rate, and the interaction term. The main effects for temperature show an unusual spike at 466°C. For strain rate it peaks at 1000/s. The interaction terms show conflicting trends. 466°C is more sensitive to strain rate effects than the other temperatures, and again 707°C is behaving in the opposite way than the other trends. Strain rate does not affect the 24, 223, and 707°C between 500/s and 1000/s, but at 1800/s it does.

For the dislocation density in the fracture region, only the temperature and the interaction are statistically significant. There is a significant change in the trend at 466°C. In the interaction effects, it is the room temperature that behaves differently than the rest of the materials, but the generally the temperature seems to increase the dislocation density until 707°C, and then the dislocation density drops at 1800/s.

The elastic modulus appears to have no statistically significant features in either the pre-necked or the fracture region. This is an indication that the stiffness is not at all affected outside of the pre-necked region of strain and has no trends.

What is apparent about these results, it that it does show that there are competing material features within the flow regions and necking regions of failure that are more inter-related than can just be described by the assigned material parameters in the Johnson-Cook model. In the following chapter, we will attempt to correlate the macromechanical behavior seen in the experimental section with the material responses we have measured here.

VII. Structure-Mesoproperty Correlation

The previous chapters have discussed experimentation on 4130 steel to determine the dynamic behavior by obtaining true stress-strain curves, and then covered the characterization of the Johnson-Cook material parameters using those curves. Next, those responses were checked against an ABAQUS simulation to validate the response. Afterwards, we microstructural features of the material were measured using EBSD and checked the grain size, misorientation, dislocation density, and elastic modulus for statistical significance in the pre-necked and fracture regions of the sample. In this section, the significant factors are analyzed for any correlations that can be made for the material parameters in the Johnson-Cook equations. This was first done in the flow equation, using the statistically significant factors measured in the pre-necked region, and then second in the damage equation, using the statistically significant factors in the fracture region.

It is important to understand how these microstructural features are involved in the deformation and flow stress process. Recall in Chapter II that deformation is a process of shifting dislocations that are generated and destroyed as a result of applied forces. These dislocations are defects to a perfect crystal lattice structure, and are present within grains and in grain boundaries. They can be short obstacles, overcome by thermal energy, or grouped together in dislocation distributions, which must be overcome by reaching a critical shear stress. Misorientation, dislocation density, and grain size are all related to this process of moving dislocations, increasing or decreasing the ease with which they move.

One major component specific to dynamic stress is the mechanism of dynamic recrystallization, where high dislocation densities are eliminated by the nucleation and growth of new grains [92] [93]. There are two different mechanisms for recrystallizations, rotation recrystallization and migration recrystallization. In rotation

recrystallization, new HAGBs are formed from subgrain boundaries shifting, or new grains forming at HAGB. Thus, the overall misorientation distribution shifts towards higher grain angle boundaries at higher strain rates for rotation recrystallization. In migration recrystallization, existing grain boundaries are altered due to the evolution of the microstructure surrounding them (grain dissection, grain coalescence, and grain boundary bulges from new grains). At low strains, it is believed the number of intermediate strains is reduced at low strains, which, theoretically, would be the microstructure that was measured in the pre-necked region. With this knowledge, we would expect misorientation angle to be smaller in the pre-necked region, but larger in the fracture region where there has been more strain and the rotation dynamic recrystallization is more prevalent.

As dynamic recrystallization occurs, it is occurring continuously, resulting in oscillating stress-strain curves as dislocations pile up and there is strain hardening, and then strain softening as grains nucleate and grow and dislocations decrease. This process is aided by the adiabatic temperature rise in materials as they deform. The higher the strain rate, the more the adiabatic temperature rises and this process is increased. For dislocation density, the number will most likely be fluctuating through the curve as flaws are generated and destroyed throughout the deformation process. The grain size will also be fluctuating as smaller grains are continuously nucleating and then growing as a result of the raised temperatures.

Now that we see how the misorientation, grain size, and dislocation density relate to deformation, we can look at what happened in these specific cases and relate them to the Johnson-Cook flow and fracture equations in the following sections.

7.1 Correlation for the Johnson-Cook Flow Equation

For reference, the Johnson-Cook flow equation is repeated below:

$$\hat{\sigma}_y = (A + B\epsilon_p^n)(1 + C \ln \frac{\dot{\epsilon}_p}{\dot{\epsilon}_o})(1 - T^{*m}) \quad (88)$$

The significant factors measured in the pre-necked region and therefore relevant to the flow equation, are as follows: misorientation, which the temperature and strain rate both impacted, and the dislocation density, which was impacted by the strain rate, temperature, and interaction terms.

We can measure the extent to which these parameters are influencing the measurement by calculating the measure of association, ω^2 .

$$\omega^2 = \frac{SS_{effect} - df_{effect}(MS_{error})}{SS_{Total} + MS_{error}} \quad (89)$$

where ω^2 is the measure of association for an ANOVA fixed-effects model, SS_{effect} is the sum of squares for the treatment effect of interest, df_{effect} is the degrees of freedom for the treatment effect of interest, MS_{error} is the mean sum of the error term for the ANOVA analysis of interest, and SS_{Total} is the total sum of squares for the ANOVA analysis of interest.

This equation shows how much a treatment is affecting the results, or contributing to the variance of the overall calculation. A summary of the measures of association is shown for the statistically significant features for the pre-necked region in Table 26.

The changes in the misorientation angle are attributed to temperature by 48.4% and strain rate by 9.4%. The changes in dislocation density are attributed to temperature by 25.3%, strain rate by 18.3% and the interaction by 34.6%.

Based on the construction of the Johnson-Cook flow equation, where the first set of parenthesis is contributions from static stress, the second set is contributions

Table 26. Measure of association for the pre-necked region

	Misorientation	Dislocation Density
Effect	ω^2	ω^2
Temperature	48.4%	25.3%
Strain Rate	9.4%	18.3%
Interaction	-	34.6%

from strain rate, and the third set is contributions from thermal effects, we can immediately make an observation. There is an effect which is dependent on the interaction effect of strain rate and temperature. It verifies the suspicion that the structure of the Johnson-Cook equation, which divides the stress-strain behavior up into separate temperature and strain rate sections, is not supported by the measured microstructural evolution. That is, there is an additional interaction effect of the strain rate and temperature not being accounted for with the equation.

Of the material parameters involved, C and m are both impacted by the misorientation angle and the dislocation density. This follows because C is representative of strain rate changes, and strain rate was a statistically-significant factor for misorientation and dislocation density measurements. Similarly, m is representative of thermal changes, and temperature was a statistically-significant factor for misorientation and dislocation density measurements. The trend in the observations of the mean measurements of misorientation and dislocation density are shown in the main effects plots shown in Figure 70 and 73. Like the Johnson-Cook equation predicts, C does increase with strain rate. The thermal contributions, related to m from misorientation show that at the highest temperature, HAGB begin to dominate the structure, indicating a preference for rotational misorientation as opposed to mitigation recrystallization.

The effects on C from the dislocation density show that there is an increase of dislocation density at 1000/s, indicating an increase in large dislocation forest pile-ups at that particular strain rate. The thermal contributions for m show an increase

in dislocation density at 466°C, indicating that at that temperature, there is not enough thermal energy to absorb and reduce dislocations. This effect is seen more in the interaction effects, which the model is not taking into account. Interestingly enough, though the strain rate and thermal contributions lower the dislocation at the highest temperature and strain rate, the interaction shows an increase in dislocation density at the highest strain rate and temperature.

A, B and n are a little more challenging to link to our ANOVA results, but it is possible to make some observations based on taking a look at the experimental results. It was evident that the yield stress dropped with increasing temperature, so clearly A is dependent on temperature. It is less clear if strain rate impacts the yield stress, but there is some evidence that it may, depending on if it is currently in an FCC or BCC structure [94].

For B and n, generally it can be said that an increase in dislocation density should cause an increase in increased strain hardening. Thus, any factor which is causing that to increase, be it temperature or strain rate, should cause an increase in B and n.

This concludes the observations about the microstructural measurements and how they correlate to the Johnson-Cook flow equation as they vary with temperature and strain rate. Next, the same process is applied to the Johnson-Cook damage criterion.

7.2 Correlation for the Johnson-Cook Damage Equation

For reference, the Johnson-Cook damage equation is repeated below.

$$D = \sum \frac{\Delta\epsilon^p}{\epsilon_f} \quad (90)$$

$$\epsilon_f = [D_1 + D_2 e^{-D_3 Q}][1 + D_4 \ln \frac{\dot{\epsilon}_p}{\dot{\epsilon}_0}][1 + D_5 T^*] \quad (91)$$

Recall that for the formation of ϵ_f , the first set of brackets refers to void formation characteristics, the second set applies to strain rate characteristics, and the third set applies to thermal characteristics.

For the fracture region, the grain size was affected by the main effects of temperature and strain rate, the misorientation was impacted by the main effects and the interaction effects, and the dislocation density was impacted by the temperature and the interaction of temperature and strain rate, but not the strain rate by itself. The results and their impact on the microstructural feature is shown as the measures of association, as calculated for the pre-necked features, is shown for the statistically significant features of the fracture region in Table 27.

D_4 and D_5 , as the temperature and strain rate terms, are now directly tied to the grain size, misorientation, and dislocation density via ANOVA results. Again, the fact that misorientation and the dislocation density are impacted by the interaction effects shows that this model is not matching what is happening within the microstructure.

The changes in the grain size are attributed to temperature by 26.7%, strain rate by 17.2%, and the interaction by 18.1%. The changes in the misorientation angle are attributed to temperature by 57.1%, strain rate by 17.2%, and the interaction by 18.6%. The changes in the dislocation density are attributed to temperature by

Table 27. Measure of association for the failure region

	Grain Size	Misorientation	Dislocation Density
Effect	ω^2	ω^2	ω^2
Temperature	26.7%	57.1%	34.3%
Strain Rate	17.2%	17.2%	-
Interaction	18.1%	18.6%	9.6%

34.2% and the interaction by 9.6%.

D_4 can be directly correlated with grain size and misorientation, and indirectly with dislocation density because of the interaction with temperature. The strain rate relationship for D_4 actually seems to be backwards. The grain size increases with increasing strain rate, which theoretically should mean fewer boundaries to impede the deformation process. The effects from misorientation are confusing as well. Though there is an increase in overall misorientation from 500/s to 1000/s, there is a reduction in misorientation at 1800/s, indicating fewer rotational boundaries and more mitigation boundaries. This generally matches with the dislocation density interaction effect, which shows a reduction in dislocation density for all temperatures except room temperature at 1800/s. The peaking behavior at 1000/s though may indicate that viscous effects are dominating at that strain rate, but then drop off after at 1800/s and switch to other motions.

D_5 is related to the grain size main effects, misorientation main effect and interaction effects, and the dislocation main effect and interaction effects. Grain size, though typically thought of as increasing with temperature, is actually being reduced at the temperature increases. This is most likely due to the fact that dynamic recrystallization is being aided by the temperature increase, resulting in more nucleation of smaller grains. The misorientation decreases with increasing temperature, but jumps at the highest temperature, indicating that until that highest temperature, thermal energy is aiding in creating mitigation boundaries. At the highest temperature however, there is are more HAGB rotational grain boundaries being created.

D_1 , D_2 , and D_3 are all based on a failure criterion developed by Hancock and Mackenzie, that holds that failure strain is proportional to the stress triaxiality [95]:

$$\epsilon_f \propto \exp\left(\alpha \frac{\sigma_m}{\bar{\sigma}}\right) \quad (92)$$

Their equation is formulated [96]:

$$\epsilon_f = \epsilon_n + \alpha \exp\left(\frac{-3}{2} \frac{\sigma_m}{\bar{\sigma}}\right) \quad (93)$$

The criterion Mackenzie and Hancock developed adds an intercept, ϵ_n which physically represents the nucleation strain needed to initiate void formation. Johnson and Cook wrap up the nucleation strains and material constants in D_1 , D_2 , and D_3 . As we saw earlier, these constants are acquired from curve fitting notched sample failure data, fitting against failure strains and triaxiality values. By analyzing what effects the constants have on the failure strains for a range of triaxialities, we can make some judgments on how the microstructure might impact the constants.

The first and easiest constant to observe is the nucleation strain constant D_1 . It is an intercept in the failure criterion, so its effect on the failure curve is to simply raise or lower the curve with increasing/decreasing value. Thus, a higher nucleation constant increases the failure strain, increasing the ductility and toughness of the overall material. So the question becomes, would grain size or dislocation density have an impact on the nucleation strain? Smaller grains and high dislocation densities create opportunities for motion to occur, so the author believes that when grain size is small and/or dislocation density is high, the nucleation strain required to initiate void growth drops, which would drop the value of D_1 .

D_2 and D_3 are more unspecific values, as they are experimentally-based consequences of curve fits. Increasing values of D_2 raise the failure predicted strain, but the effect is more pronounced for smaller triaxialities and drops off as the triaxiality increases. Increasing D_3 , on the other hand, reduces the predicted failure strain. Again the effect is more prevalent with smaller triaxialities and drops off with increasing triaxiality, especially as the value of D_3 increases. How to predict these coefficients will fluctuate is trickier to predict, as their effects are somewhat dependent on the

triaxiality. During dynamic impact, triaxiality is not constant. Generally though, the dislocation principles can be applied to the coefficients, where higher misorientation and dislocation should drive up the D_2 and reduce D_3 , or lower dislocation densities and misorientations should lower D_2 and raise D_3 .

VIII. Conclusion

This dissertation has shown the methodology used in determining the parameters of a plastic strain rate formulation (Johnson-Cook Constitutive and Damage models). Results from the coefficient-solving are then used in a finite element model and compared directly against experimental data. The tested and untested materials were analyzed for microstructural features using EBSD, and then statistically-analyzed via ANOVA to determine their impact on the flow stress and fracture behavior.

This study has accomplished a number of things of significance. First and foremost, it has identified shortcomings in the Johnson-Cook model. By running an experimental program, it has been revealed that for heat-treated 4130 steel, the thermal behavior seen in the material does not match the linear fitting method the Johnson-Cook method uses for either the flow equation or the damage criterion. Practically, this indicates that the Johnson-Cook model is not the best choice in modeling dynamically-impacted heat-treated 4130 steel for the temperature and strain rate ranges explored in this study.

Looking at how the material is behaving with temperature changes raises some additional questions. Based on the dramatic change in behavior at the highest temperature, it is believed that there is a phase change occurring at 707°C . If this is true, this study is also showing the difference in dynamic behavior for ferritic (BCC) and austenitic (FCC) steel structures. This could have further implications for how steels should be modeled, where a piecewise function should be used to model behavior for each different structure's regime.

The statistical investigation of the microstructural features supports the idea that the Johnson-Cook model is not taking all dynamic contributions into account in two ways. One, it shows how the interaction effects of temperature and strain rate are statistically-significant, not independent of each other as both equations are formu-

lated. To be able to model the interaction effect, another materials coefficient needs to be added.

Moving forward, as AFIT is continuing to work on modeling dynamic events, a different model should be considered that takes structure into account. Alternatively, the Johnson-Cook model could be altered to better fit the experimental data, but in this case it would be prudent to obtain data in at a higher temperature to solidify the trends that occur beyond 707°C.

The summary of conclusions drawn from this study are listed below:

8.1 Conclusions

- For 4130 steel, temperature reduces the flow stress, while strain rate increases the flow stress
- 4130 Steel has reduced ductility from 24°C to 466°C
- The Johnson Cook flow parameters were found to be $A = 673$ MPa, $B = 190$ GPa, $n = 0.1538$, $C = 0.017$, $m = 1.07$
- the Johnson-Cook Damage parameters were found to be $D1 = -0.1895$, $D2 = 0.7324$, $D3 = 0.6633$, $D4 = 0.0291$, $D5 = 0.7162$
- The ABAQUS simulation shows good agreement for the Johnson Cook flow stress
- The ABAQUS simulation does not show good agreement for the Johnson-Cook damage equation
- ABAQUS is a better method of simulation as opposed to our numerical MATLAB simulation because of its ability to include three-dimensional effects and track the evolving triaxiality

- The ANOVA analysis of the post-yield, pre-necking microstructure of 4130 shows that misorientation main effects and interaction and dislocation main effects and interactions are statistically significant
- The ANOVA analysis of the fracture microstructure of 4130 shows that grain size main effects, misorientation main effects and interaction and dislocation main effects and interactions are statistically significant
- The pre-necked region shows that grain size is not statistically significant (temperature p-value = 0.106, strain rate p-value = 0.054)
- The pre-necked region shows that for misorientation, the temperature and strain rate are significant (p-values of 0 and 0.0026) but not the interaction (p value = 0.052)
- The measure of association for misorientation in the pre-necked region is 48.4% for temperature and 9.4% for strain rate
- The pre-necked measurements show that the dislocation density is affected by the temperature, strain rate, and interaction effects (p-values = 0.001, 0.002, and 0.002 respectively)
- The measure of association for the dislocation density in the pre-necking region are 25.3% for temperature, 18.3% for strain rate, and 34.6% for interaction effects
- The pre-necked region shows that the elastic modulus is not statistically-significantly affected by the temperature, strain rate, or interaction (p-values = 0.157, 0.878, 0.214).
- The failed region shows that grain size the temperature, strain rate, and interaction effects are significant (p-values = 0.000, 0.000, and 0.002)

- The measure of association for the grain size in the failed region is 26.7% for temperature, 17.2% for strain rate, and 18.1% for the interaction effects
- The failed region shows that for misorientation, the temperature, strain rate, and interaction effects are significant (p-values = 0.000, 0.000, and 0.000)
- The measure of association for the misorientation in the fracture region is 57.1% for temperature, 17.2% for strain rate, and 18.6% for the interaction effect
- The failed region measurements show that the dislocation density is affected by the temperature, and interaction effects (p-values = 0.000, 0.045), but not the strain rate (p-value = 0.144)
- The measure of association for the dislocation density in the fracture region is 34.3% for temperature and 9.6% for the interaction effects
- The failed region shows that the elastic modulus is not statistically-significantly affected by the temperature, strain rate, or interaction (p-values = 0.127, 0.454, 0.212).
- The Johnson-Cook flow stress is unable to account for the dislocation density interaction effects
- The Johnson-Cook Damage equation is unable to account for the misorientation and dislocation density interaction effects

8.2 Recommendations

- Obtain dynamic data with reduced dynamic ringing effects in the results
- Employ digital image correlation to obtain true stress-strain curves without having to make area approximations

- Take more microstructural scans to reduce variance in results
- Consider using the Zerelli-Armstrong model to model plastic strain if material is being used at a high temperature and is subject to phase changes
- Consider using a damage criterion that takes structure into account, such as one being developed by George Voyiadjis [94].

IX. Appendix

9.1 Appendix A: Materials-based Derivation of Elastic Modulus

The deformation response of a material is based on how the atoms within the structure are moving around. With the knowledge of the energy associated with keeping atoms a certain distance apart in equilibrium, and then subsequently how it changes when they are pushed closer together or farther apart, it is possible to build an equation that outputs the amount of energy generated from an applied force. This can be used as a basis for predicting macroproperties of materials or even constitutive models. The following section is an example of one such instance, where the elastic modulus is derived using materials science principals taken from a textbook Elastic and Inelastic Stress Analysis [30].

Derivation of the Materials/physics-based relationship for the Elastic Modulus.

We will start with a material with a hexagonal close-packed lattice structure. A force is applied on the x-crystallographic axis that is less than the elastic limit of this material. This will allow the atoms to shift, but not reach the critical bonding force needed to break the bonds. After the force is removed, the atoms would shift back to their original position. The following equation is a balance of repulsion and attraction forces experienced by atoms within the crystal lattice with a force applied.

$$F = -\frac{m\beta}{(a + \Delta x)^{m+1}} + \frac{n\alpha}{(a + \Delta x)^{n+1}} \quad (94)$$

Where F is an applied force, “a” is the packing factor for HPC structure ($a = \sqrt{2}D$, where D is the diameter of the atom), β and m are repulsion-associated constants, and α and n are attraction-related constants.

Apply a binomial expansion:

$$F = \left[-\frac{m\beta}{a^{m+1}} + \frac{n\alpha}{a^{n+1}}\right] + \left[\frac{m(m+1)\beta}{a^{m+2}} - \frac{n(n+1)\alpha}{a^{n+2}}\right]\Delta x + \dots \quad (95)$$

By calculating an equilibrium state by differentiating and setting the equation equal to 0, we drop the first bracketed constant term and lose β from the second bracketed expression. By assuming small deflections ignore higher order Δx terms, our equation reduces to:

$$F = \frac{n(m-n)\alpha}{a^{n+2}}\Delta x \quad (96)$$

From this expression, we can begin to formulate a relationship for Young's Modulus. The force applied can be described using the applied stress τ_{xx} and the geometric packing properties of the HCP structure. Prior to load application, the perpendicular spacing between rows was $a\sqrt{3}/s$, and the perpendicular distance between planes is given by $c/2 = a\sqrt{6}/3$. Thus the projected area of the applied stress per row of atoms is $A = (a\sqrt{3}/2)(a\sqrt{6}/3) = a^2\sqrt{2}/2$. Thus F can be expressed as the product of the stress and the area:

$$F = \tau_{xx} \frac{\sqrt{2}}{2} a^2 \quad (97)$$

This expression is substituted back into Equation 96 along with the axial strain expression $\epsilon_{xx} = \frac{\Delta x}{a}$ yields:

$$\tau_{xx} = \frac{\sqrt{2}n(m-n)\alpha}{a^{n+3}\epsilon_{xx}} \quad (98)$$

Finally using the relationship $E = \frac{\tau_{xx}}{\epsilon_{xx}}$, we get a one-dimensional microstructural relationship for Young's Modulus for a HCP arrangement:

$$E = \frac{\sqrt{2}n(m-n)\alpha}{a^{n+3}} \quad (99)$$

This is only a simple derivation and to be more accurate requires taking other factors into account such as anisotropy, temperature effects, etc. But it does show how microstructural features such as atomic arrangement can be used and extrapolated to explain microstructural behavior.

9.2 Appendix B: UDRI Experiment Engineering Stress-Strain Results

In June of 2014, an experimental program was carried out at UDRI utilizing split-Hopkinson bar experiments to get dynamic responses of 4130 steel at a variety of strain rates and temperatures. The strain rates tested were approximately 500, 1000, and 1800/s, and the temperatures were room (24°C), 223, 466, and 707°C. Three samples were run for each test condition. The results from these experiments are shown in the following tables, grouped by temperature of the run.

Engineering Stress-Strain AFIT 4130 Treated Steel

Room Temperature Data @ ~500/s, ~1000/s, and ~1800/s

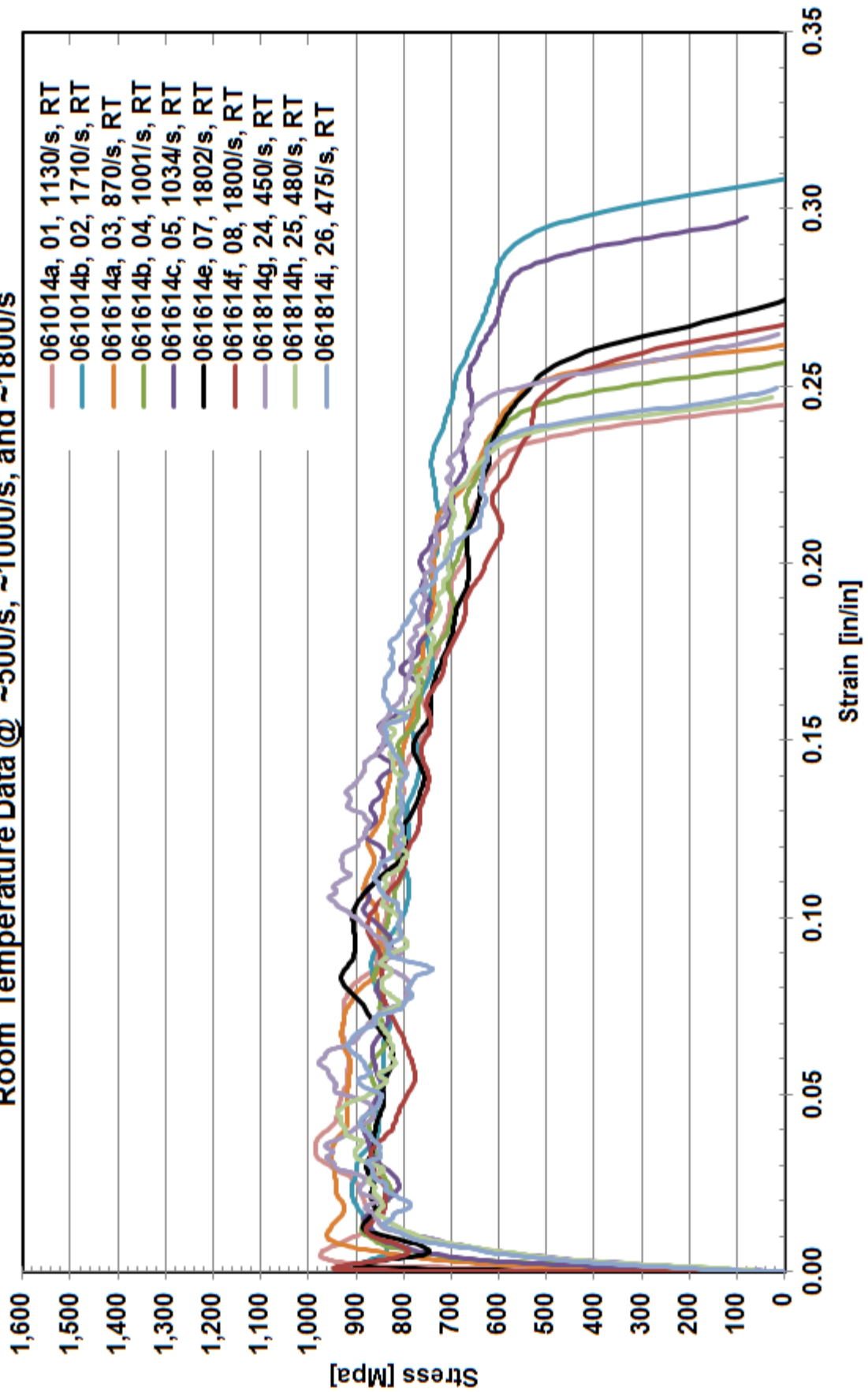


Figure 77. Engineering stress-strain curves for room temperature high strain rate runs

Engineering Stress-Strain AFIT 4130 Treated Steel

435°F (223°C) Data @ ~500/s, ~1000/s, and ~1800/s

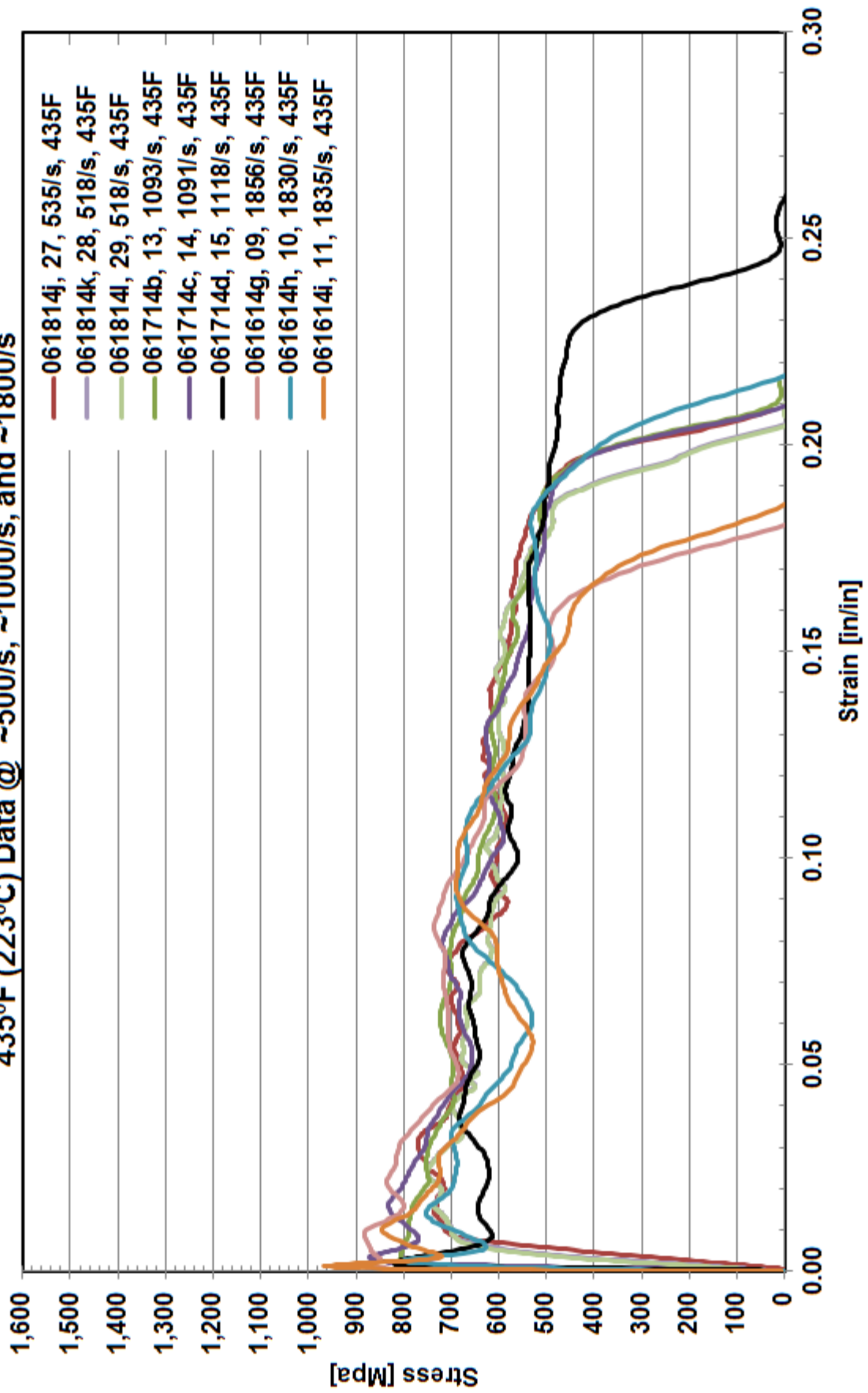


Figure 78. Engineering stress-strain curves for 1/6 melt temperature (223°C) high strain rate runs

Engineering Stress-Strain AFIT 4130 Treated Steel

870°F (466°C) Data @ ~500/s, ~1000/s, and ~1800/s

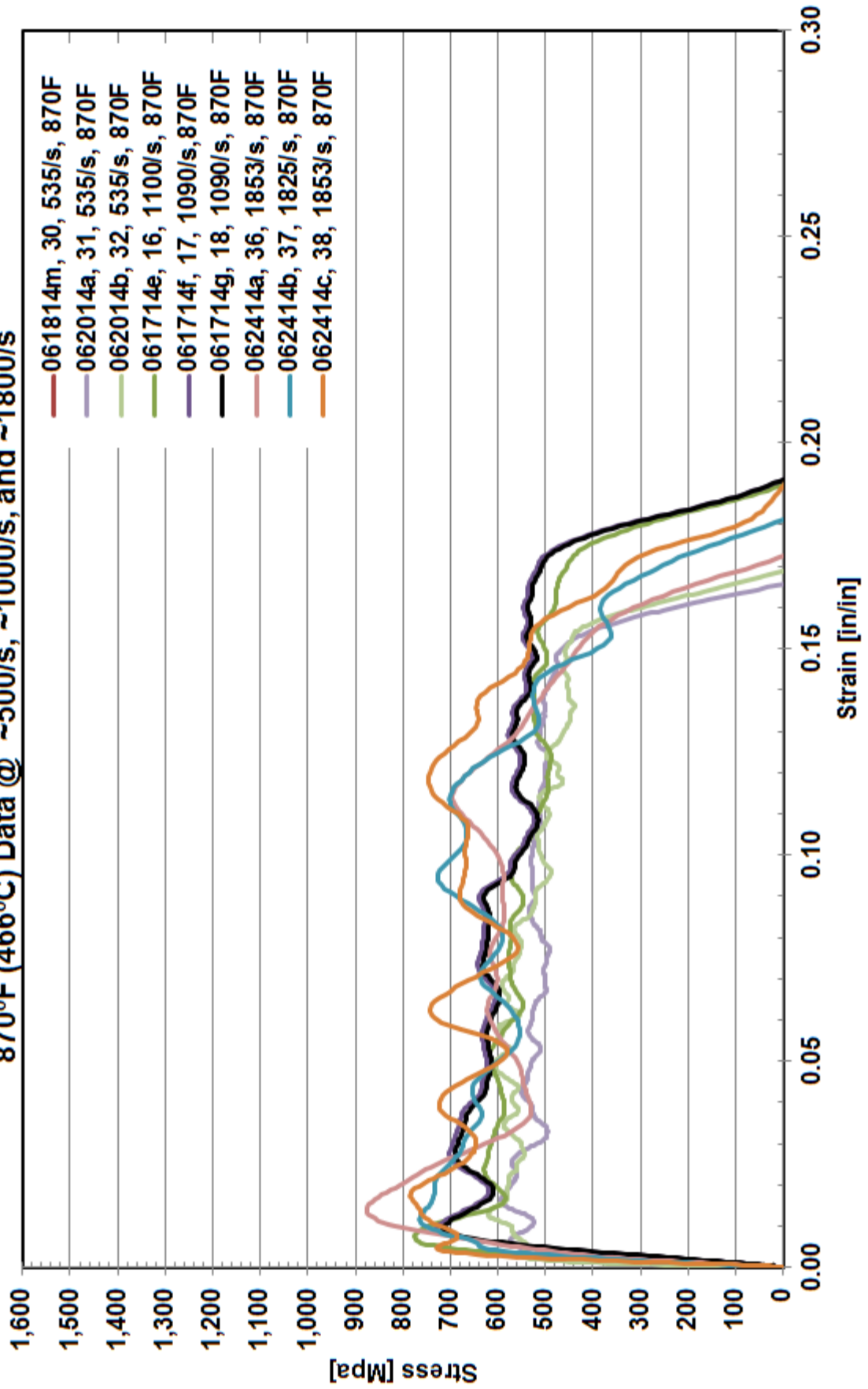


Figure 79. Engineering stress-strain curves for 1/3 melt temperature (466°C) temperature high strain rate runs

Engineering Stress-Strain AFIT 4130 Treated Steel

1305°F (707°C) Data @ ~500/s, ~1000/s, and ~1800/s

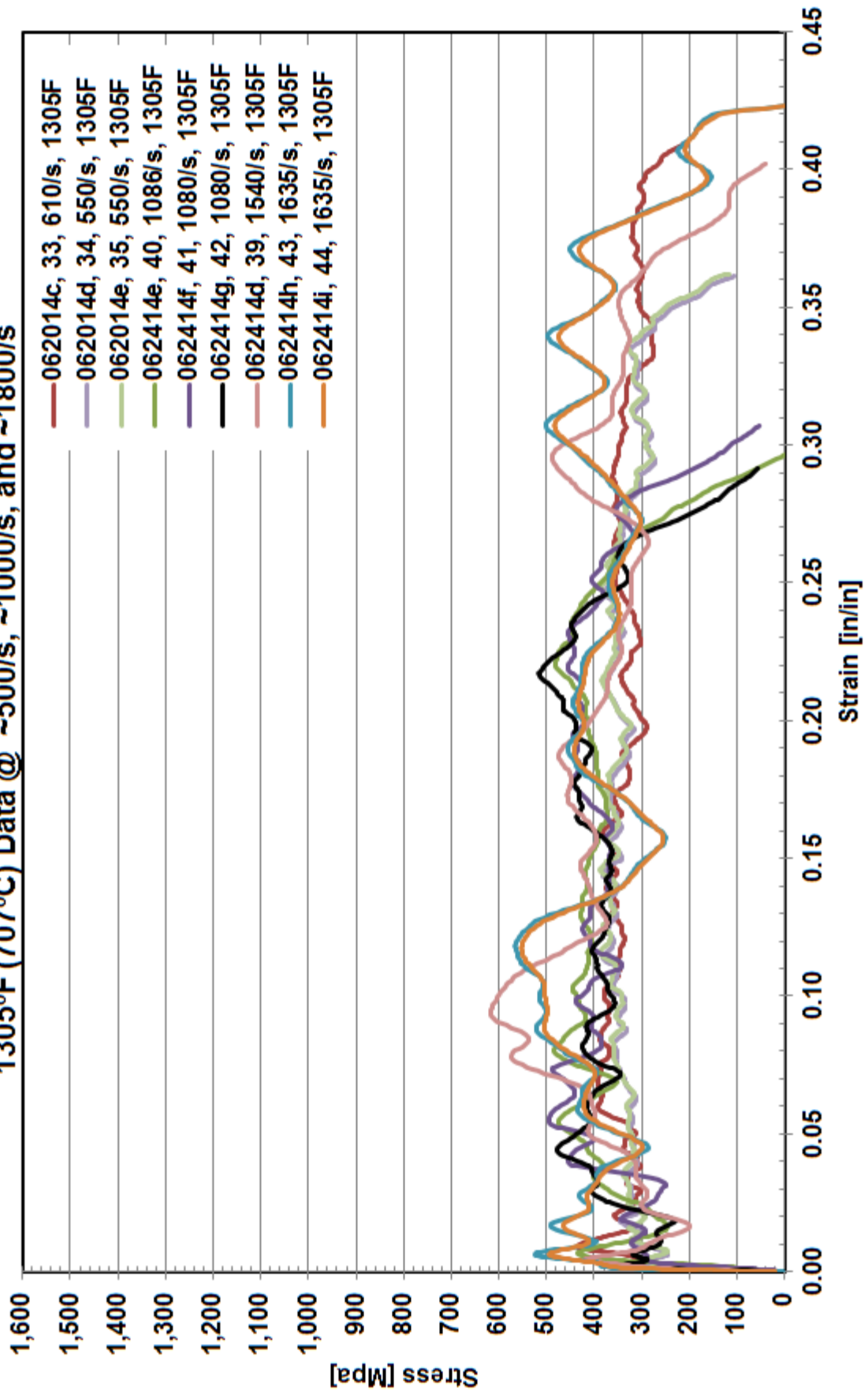


Figure 80. Engineering stress-strain curves for 1/2 melt temperature (707°C) temperature high strain rate runs

9.3 Appendix C: ABAQUS Process

This section is an overview of a flowchart that illustrates the process ABAQUS uses when solving a viscoplastic finite element problem with the Johnson-Cook model, mostly modeled after similar work done by Rodolfo Buentello in his dissertation [?]. The flowchart is shown in Figure 81, and has numbers labeling each station where calculations are made. The following numbers correlate with those on the graph, and explain what is going on at each point in the process.

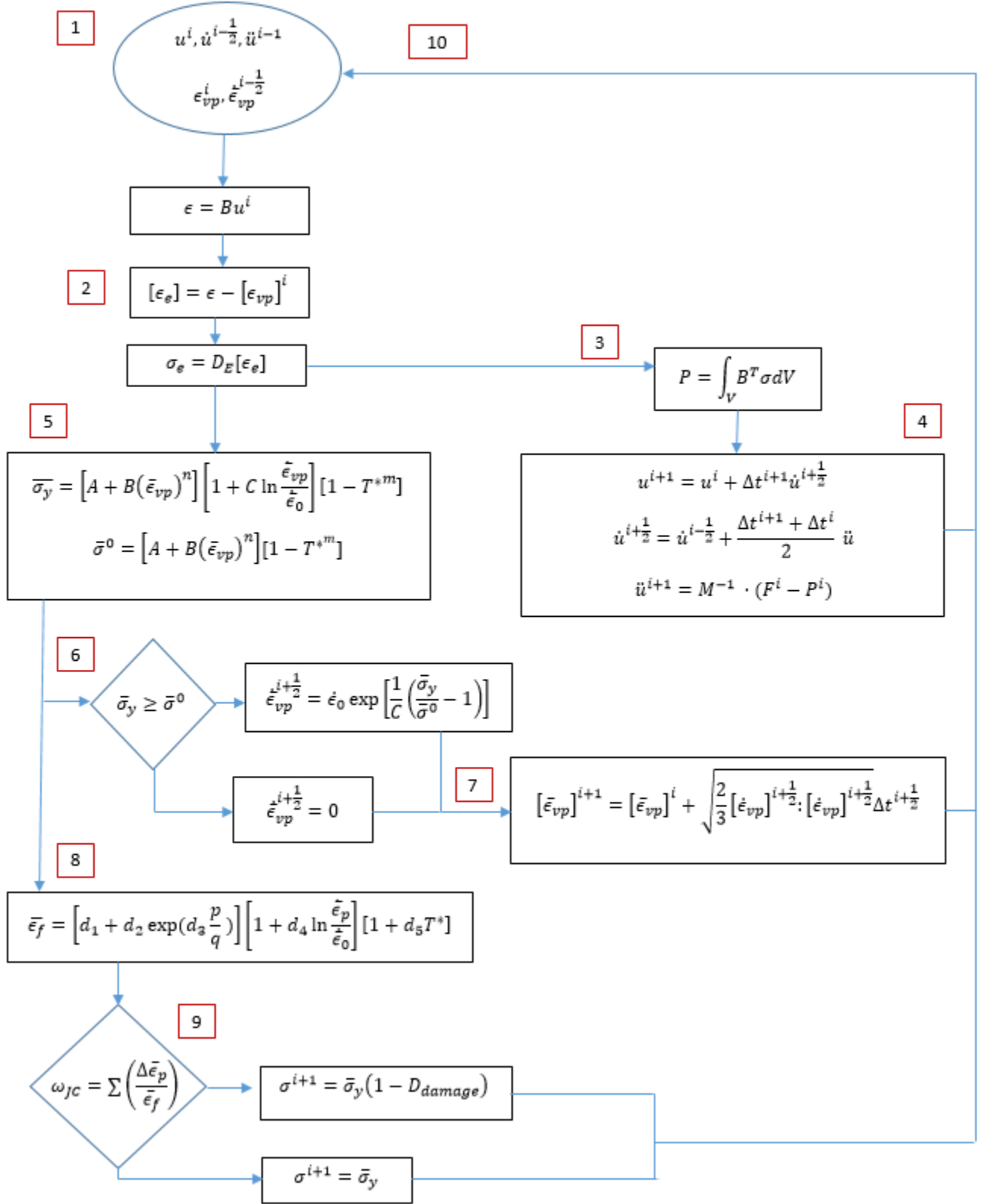


Figure 81. Average normalized stiffness in the elastic zone for all strain rates and temperature conditions, where each point is the average of four difference EBSD scans

1. Starting Off

We start off our calculations with known, either from the initial conditions placed on the scenario, or calculated from the previous time step. We are starting with the displacement (u_i), velocity(\dot{u}), and acceleration(\ddot{u}), viscoplastic strain(ε_{vp}), and viscoplastic strain rate ($\dot{\varepsilon}$). We also have a value for the next time step (t_i)

2. Initial Calculations

We now move into calculating values needed for the equations of motion. First, the individual strain element is calculated .

$$\varepsilon = \mathbf{B}u^i \quad (100)$$

where \mathbf{B} is the strain-displacement matrix Then the elastic portion is separated out

$$[\varepsilon_e] = \varepsilon - [\varepsilon_{vp}^i] \quad (101)$$

Finally the elastic stress is calculated:

$$\sigma_e = \mathbf{D}_E [\varepsilon_e] \quad (102)$$

where \mathbf{D}_E is the elasticity matrix

$$\mathbf{P} = \int_V \mathbf{B}^T : \boldsymbol{\sigma} dV \quad (103)$$

where \mathbf{B} is a strain-displacement and V is the volume of the material at the current point in time.

3. Internal Force Vector \mathbf{P} , the is the internal force vector, is calculated by:

$$\mathbf{P} = \int_V \mathbf{B}^T : \boldsymbol{\sigma} dV \quad (104)$$

where \mathbf{B} is a strain-displacement and V is the volume of the material at the current point in time.

4. Explicit Dynamic Analysis

Next the equation of motion are solved (displacement, velocity, and acceleration), which are solved using a time step and integration schemes. They are integrated using the explicit central difference integration rule.

$$u^{(i+1)} = u^i + \Delta t^{(i+1)} \dot{u}^{(i+1/2)} \quad (105)$$

where u is the displacement, Δt is a time step, and \dot{u} is the derivative of displacement, velocity.

$$\dot{u}^{(i+1/2)} = \dot{u}^{i-1/2} + \frac{\Delta t^{(i+1)} + \Delta t^{(i)}}{2} \ddot{u} \quad (106)$$

where \ddot{u} is the derivative of velocity, acceleration

$$\ddot{u}^{(i)} = \mathbf{M}^{-1} \cdot (\mathbf{F}^{(i)} - \mathbf{P}^{(i)}) \quad (107)$$

where \mathbf{M} is the diagonal mass matrix, \mathbf{F} is the applied force, and \mathbf{P} is the internal force vector

You may be wondering where the half-values are coming from. They are based on numbers from the previous time step. It is defined by:

$$\dot{u}^{(-1/2)} = \dot{u}^{(0)} + \frac{\Delta t^{(0)}}{2} \ddot{u}^{(0)} \quad (108)$$

The numbers calculated in this step are then recorded and used for the next time-step.

5. JC Flow and static stresses

The flow stress and static stresses are calculated using the Johnson-Cook flow equations below.

Flow stress:

$$\bar{\sigma}_y = [A + B(\varepsilon_{vp})^n] \left[1 + C \ln \left(\frac{\dot{\varepsilon}_{vp}}{\dot{\varepsilon}_0} \right) \right] [1 - (T^*)^m] \quad (109)$$

Static Stress:

$$\bar{\sigma}^0 = [A + B(\varepsilon_{vp})^n] [1 - (T^*)^m] \quad (110)$$

6. Flow Rule Condition

The process now checks to see if yield has occurred yet and if damage has occurred. We will first look at the flow rule condition. It's checking to see whether the flow stress is greater than the yield stress we just calculated in the step before.

$$\bar{\sigma}_y \geq \bar{\sigma}^0 \quad (111)$$

If so, yield has occurred. The equivalent plastic strain rate is calculated as:

$$\dot{\varepsilon}^{i+1/2} = \dot{\varepsilon}_0 \exp \left[\frac{1}{C} \left(\frac{\bar{\sigma}_y}{\bar{\sigma}^0} - 1 \right) \right] \quad (112)$$

Otherwise, there is no viscoplastic strain rate developed, and is set to zero.

$$\dot{\bar{\epsilon}}^{i+1/2} = 0 \quad (113)$$

The equivalent plastic strain is then calculated in the next step.

7. Calculating Equivalent Plastic Strain

Using the results from the previous step, the equivalent plastic strain is calculated using the following equation:

$$[\bar{\epsilon}_{vp}]^{1+1/2} = [\bar{\epsilon}_{vp}]^i + \sqrt{\frac{2}{3} [\dot{\epsilon}_{vp}]^{i+1/2} : [\dot{\epsilon}_{vp}]^{i+1/2} \Delta t^{i+1/2}} \quad (114)$$

The equivalent plastic strain is sent along to the next time step calculation.

8. Checking the Damage Criterion

The final leg of this journey is calculating the stress in the material. First we start with checking the damage criterion, starting with calculating the Johnson-Cook critical strain for this time step.

$$\bar{\epsilon}_f = [D1 + D2 \exp^{-D3\sigma^*}] \left[1 + D4 \ln \frac{\dot{\bar{\epsilon}}_p}{\dot{\bar{\epsilon}}_0} \right] [1 + D5(T^*)] \quad (115)$$

where σ^*

Once this has been calculated, we can check the damage criterion:

$$\omega_{JC} = \sum \frac{\Delta \bar{\epsilon}_p}{\bar{\epsilon}_f} \quad (116)$$

If $\omega_{JC} \geq 1$, damage has occurred and the stress is calculated according to the

damage evolution equation used in ABAQUS:

$$\sigma^{i+1} = \bar{\sigma}_y(1 - D_{damage}) \quad (117)$$

where $\bar{\sigma}_y$ is the flow stress and D_{damage} is the damage evolution criterion variable.

If not, the stress is simply equal to the previously calculated flow stress:

$$\sigma^{i+1} = \bar{\sigma}_y \quad (118)$$

The stress from calculated is sent on to the next time step

9. Repeat

We're done! We have the displacement, velocity, and acceleration calculated, the equivalent plastic strain and strain rate, and the flow stress calculated. We can now move on to the next time increment and repeat the process.

9.4 Appendix D: ANOVA Example

The following is a simplified example of the calculations required to carry out a 2-factor fixed-effects ANOVA analysis. We will be testing the null hypothesis, that is, that the variation of the treatment and interaction factors is equal to zero. We will check this by calculating our test statistic, the F-number, and comparing it against the F-distribution table. Should the calculated F statistic be greater than the one found in the F-distribution table, the null hypothesis is rejected.

We will start with some example data of grain sizes:

Our two factors are strain rate (A) and temperature (B). There are two replicates of each condition (n=2), three levels of strain rates(b=3), and 4 levels of temperatures (a=4).

Table 28. Example Grain Size Data for ANOVA 2-Way Fixed Effects Model

	Low Strain Rate	Mid Strain Rate	High Strain Rate
Low Temp	8.5, 8.9	8.3, 8.7	16.3, 16.4
Mid Low Temp	8.5, 8.9	7.8, 8.4	14.7, 16.9
Mid High Temp	9.3, 9.2	7.8, 8.4	9.5, 9.2
High Temp	6.5, 6.9	8.8, 8.9	7.1, 6.9

We can start by calculating $y_{i..}$, $y_{.j.}$, and $y_{...}$ by summing the columns and rows, as shown in the Table 29.

So, the relevant take-away from the table is:

$$\begin{aligned}
 y_{...} &= \sum_{i=1}^a \sum_{j=1}^b \sum_{k=1}^n y_{ijk} \\
 &= 230.8
 \end{aligned} \tag{119}$$

$$\begin{aligned}
 y_{i..} &= \sum_{j=1}^b \sum_{k=1}^n y_{ijk} \\
 &= [67.1, 65.2, 53.4, 45.1]
 \end{aligned} \tag{120}$$

Table 29. Grain size data column and row summations

	Low Strain Rate	Mid Strain Rate	High Strain Rate	$y_{i..}$ = sum of rows
Low Temp	8.5, 8.9	8.3, 9.7	16.3, 16.4	67.1
Mid Low Temp	8.5, 8.9	7.8, 8.4	14.7, 16.9	65.2
Mid High Temp	9.3, 9.2	7.8, 8.4	9.5, 9.2	53.4
High Temp	6.5, 6.9	8.8, 8.9	7.1, 6.9	45.1
$y_{.j.}$ = sum of column	66.7	67.1	97	230.8

$$\begin{aligned}
y_{.j} &= \sum_{i=1}^a \sum_{k=1}^n y_{ijk} \\
&= [66.7, 67.1, 97]
\end{aligned} \tag{121}$$

We can also calculate y_{ij} which will be important for the calculating the interaction terms.

$$\begin{aligned}
y_{ij} &= \sum_{k=1}^n y_{ijk} \\
y_{ij} &= (8.5 + 8.9), (8.3 + 8.7), (16.3 + 16.4), (8.5 + 8.9), (7.8 + 8.4), (14.7 + 16.9), \\
&\quad (9.3 + 9.2), (7.8 + 8.4), (9.5 + 9.2), (6.5 + 6.9), (8.8 + 8.9), (7.1 + 6.9) \\
y_{ij} &= [17.4, 17, 32.7, 17.4, 16.2, 31.6, 18.5, 16.2, 18.7, 13.4, 17.7, 14]
\end{aligned} \tag{122}$$

Next we can move into calculating the sum of squares. We will start with the total sum of squares.

$$\begin{aligned}
SS_T &= \sum_{i=1}^a \sum_{j=1}^b \sum_{k=1}^n y_{ijk}^2 - \frac{y_{...}^2}{abn} \\
&= 8.5^2 + 8.3^2 + 16.3^2 + 8.9^2 + \dots + 7.1^2 + 6.9^2 + 8.9^2 + 6.9^2 - \frac{230.8^2}{24} \\
&= 2437.2 - 2219.53
\end{aligned} \tag{123}$$

$$SS_T = 217.673$$

Next we can move on to calculating the sum of squares for Treatment A (temper-

ature).

$$\begin{aligned}
SS_A &= \frac{1}{bn} \sum_{i=1}^a y_{i..}^2 - \frac{y_{...}^2}{abn} \\
&= \frac{67.1^2}{6} + \frac{65.2^2}{6} + \frac{53.4^2}{6} + \frac{45.1^2}{6} - \frac{230.8^2}{24} \\
&= 2273.17 - 2219.5 \\
&= 53.7
\end{aligned} \tag{124}$$

Repeating for Treatment B (strain rate):

$$\begin{aligned}
SS_B &= \frac{1}{an} \sum_{j=1}^b y_{.j.}^2 - \frac{y_{...}^2}{abn} \\
&= \frac{66.7^2}{8} + \frac{67.1^2}{8} + \frac{97^2}{8} - \frac{230.8^2}{24} \\
&= 2295.0 - 2219.5 \\
&= 75.5
\end{aligned} \tag{125}$$

The interaction term sum of squares is as follows:

$$\begin{aligned}
SS_{AB} &= \frac{1}{n} \sum_{i=1}^a \sum_{j=1}^b y_{ij.}^2 - \frac{y_{...}^2}{abn} - SS_A - SS_B \\
&= \frac{17.4^2}{2} + \frac{17^2}{2} + \frac{32.7^2}{2} + \frac{17.4^2}{2} + \frac{16.2^2}{2} + \frac{31.6^2}{2} \\
&\quad + \frac{18.5^2}{2} + \frac{16.2^2}{2} + \frac{18.7^2}{2} + \frac{13.4^2}{2} + \frac{17.7^2}{2} + \frac{14^2}{2} - \frac{230.8^2}{24} - \\
&= 2434.0 - 2219.5 - 53.7 - 75.5
\end{aligned} \tag{126}$$

$$SS_{AB} = 85.3$$

And the last sum of squares term we need to calculate is the error.

$$\begin{aligned}SS_{error} &= SS_T - SS_A - SS_B - SS_{AB} \\&= 217.7 - 53.7 - 75.5 - 85.3 \\&= 3.2\end{aligned}\tag{127}$$

Next we can calculate the degrees of freedom for each of the effects.

The degrees of freedom for the temperature are:

$$df_a = a - 1 = 4 - 1 = 3\tag{128}$$

The degrees of freedom for the strain rate are

$$df_b = b - 1 = 3 - 1 = 2\tag{129}$$

The degrees of freedom for the interaction term are:

$$\begin{aligned}df_{AB} &= (a - 1) \times (b - 1) \\&= (4 - 1)(3 - 1) \\&= (3)(2) \\&= 6\end{aligned}\tag{130}$$

The degrees of freedom for the error are shown below.

$$\begin{aligned}df_{error} &= (r - 1) \times a \times b \\&= (2 - 1) \times 4 \times 3 \\&= 12\end{aligned}\tag{131}$$

Moving on, we calculate the mean square of each of the effects. The mean square is the ratio of the sum of squares to the degrees of freedom.

The Mean Square for temperature:

$$\begin{aligned} MS_A &= \frac{SS_A}{df_A} \\ &= \frac{54.9}{3} \\ &= 18.3 \end{aligned} \tag{132}$$

The Mean square for strain rate:

$$\begin{aligned} MS_B &= \frac{SS_B}{df_B} \\ &= \frac{74.8}{2} \\ &= 37.5 \end{aligned} \tag{133}$$

The mean square for the interaction:

$$\begin{aligned} MS_{AB} &= \frac{SS_{AB}}{df_{AB}} \\ &= \frac{86}{6} \\ &= 14.3 \end{aligned} \tag{134}$$

And the mean square for error:

$$\begin{aligned} MS_{error} &= \frac{SS_{error}}{df_{error}} \\ &= \frac{3.2}{12} \\ &= 0.3 \end{aligned} \tag{135}$$

Finally, we can calculate the F-test figure and look up the comparative F-distribution

number to compare against

$$\begin{aligned}
 F_A &= MS_A/MS_{Error} & F_A &\sim F(df_A, df_{error}) \\
 &= 17.9/0.27 & F_A &\sim F(3, 12) \\
 &= 66.3 & F_A &\sim 3.49
 \end{aligned} \tag{136}$$

$$\begin{aligned}
 F_B &= MS_B/MS_{Error} & F_B &\sim F(df_B, df_{error}) \\
 &= 37.8/0.27 & F_B &\sim F(2, 12) \\
 &= 140.0 & F_B &\sim 3.89
 \end{aligned} \tag{137}$$

$$\begin{aligned}
 F_{AB} &= MS_{AB}/MS_{Error} & F_{AB} &\sim F(df_{AB}, df_{error}) \\
 &= 14.2/0.27 & F_{AB} &\sim F(6, 12) \\
 &= 52.6 & F_{AB} &\sim 3.00
 \end{aligned} \tag{138}$$

The ANOVA statistics are summarized in Table 30:

Table 30. Calculated Results for Example Problem

Source	DF	SS	MS	F	F_{table}
Temperature	3	53.7	17.9	66.3	3.49
Strain	2	75.5	37.8	140.0	3.89
Interaction	6	85.3	14.2	52.6	3.00
Error	12	3.2	0.27		
Total	23	217.7			

Comparing the calculated F values to those found from the F-distribution, we can conclude that the null hypotheses is rejected for all of the factors and the temperature,

strain rate, and interaction all cause variation to the mean. As a check, we can run the ANOVA analysis in both Minitab and Excel to verify the numbers. The results are shown below in Tables 31 and 32

Table 31. Minitab Results for Example Problem

Source	DF	SS	MS	F	P
Temperature	3	53.646	17.8811	67.48	0.0
Strain	2	75.511	37.7554	142.47	0.0
Interaction	6	85.339	14.2232	53.67	0.0
Error	12	3.180	0.2650		
Total	23	217.673			

Table 32. Minitab Results for Example Problem

Source	DF	SS	MS	F	P
Temperature	3	53.646	17.8811	67.48	0.0
Strain	2	75.511	37.7554	142.47	0.0
Interaction	6	85.339	14.2232	53.67	0.0
Error	12	3.180	0.2650		
Total	23	217.673			

$$\sigma \propto \ln \dot{\epsilon} \quad (139)$$

sigma is flow stress

$$\dot{\epsilon} \propto \frac{1}{M} \rho b \nu \quad (140)$$

M is a material parameter b is the burger's vector ρ is the dislocation density ν is the velocity

Both programs are in agreement, and match with the hand-calculated results within rounding error. Since the p-values are below 0.05, they also show the same conclusion: that each factor is statistically significant and the null hypothesis for each must be rejected.

Bibliography

1. R. G. Buentello Hernandez. *3D Finite Element Modeling of Sliding Wear AFIT-ENY-D-06 (Ph.D. Dissertation)*, publisher = "Wright Patterson Air Force Base. 2013.
2. C. S. Hale. Consideration of wear rates at high velocity afit/ds/eny/10-08 (ph.d. dissertation). Report, Wright Patterson Air Force Base, 2010.
3. Z. Kennan. *Determination of the Constitutive Equations for 1080 Steel and Vascamax 300 AFIT/GAE/ENY/05-J05 (Master's Thesis)*. Wright Patterson Air Force Base, 2005.
4. S. P. Meador. *Consideration of Wear at High Velocities AFIT/DS/ENY/10M-16 (Master's Thesis)*. Wright Patterson Air Force Base, Dayton, 2010.
5. F. P. Gerstle. *The Sandia Rocket Sled and Slipper Study*. 1968.
6. D. J. Laird. *The Investigation of Hypervelocity Gauging AFIT/DS/ENY 02-01 (Ph.D. Dissertation)*. Wright Patterson Air Force Base, 2002.
7. A. G. Szmerekovsky. *The Physical Understanding of the Use of Coatings to Mitigate Hypervelocity Gouging Considering Real Test Sled Dimensions AFIT/DS/ENY 04-06*. Wright Patterson Air Force Base, 2004.
8. R. H. Korkegi and R. A. Briggs. *Aerodynamics of the Hypersonic Slipper Bearing*. Aerospace Research Labs Wright-Patterson Air Force Base, 1968.
9. J. D. Cinnamon. *Analysis and Simulation of Hypervelocity Gouging Impacts AFIT DS/ENY/06-01 (Ph.D. Dissertation)*, publisher =.
10. J. Cinnamon. *Hypervelocity Gouging Impacts (Progress in Astronautics and Aeronautics)*. American Institution of Aeronautics and Astronautics, 2009.
11. G. R. Johnson and W. H. Cook. A constitutive model and data for metals subjected to large strains, high strain rates and high temperatures. In *Proceedings of the 7th International Symposium on Ballistics*. 1983.
12. J. Cruthirds. *Steady State Stress in a Coated Infinite Half-Space Subjected to a Moving Load AFIT/GCS/ENC/05-01 (Master's Thesis)*. Wright Patterson Air Force Base, 2005.
13. M. Blomer. *Cost Comparison of Existing Coatings for a Hypervelocity Test Rail AFIT/GAE/ENY05-J01 (Master's Thesis)*. Wright Patterson Air Force Base, 2005.

14. R. J. Pendleton. *Validation of a Sealed Plane Strain Hypervelocity Gouging Model AFIT/GAE/ENY/06-M26 (Master's Thesis)*. Wright Patterson Air Force Base, 2006.
15. G. J. Cameron. *An Evaluation of High Velocity Wear AFIT/GAE/ENY/07-M06 (Master's Thesis)*. Wright Patterson Air Force Base, 2007.
16. Palazotto A. Cameron, G. An evaluation of high velocity wear. *Wear*, 265:1066–1075.
17. M. F. Ashby and S. C. Lim. Wear-mechanism maps. *Scripta Metallurgica et Materialia*, 25(5):805–810, 1990.
18. A. Chmiel. *Finite Element Simulation Methods for Dry Sliding Wear AFIT/GAE/ENY/08-Mo3 (Master's Thesis)*. Wright Patterson Air Force Base, Dayton, 2008.
19. J. F. Archard. Contact and rubbing of flat surface. *Journal of Applied Physics*, 24(8):981–988, 1953.
20. H. Hooputra, H. Gese, H. Dell, and H. Werner. A comprehensive failure model for crashworthiness simulation of aluminum extrusions. *International Journal of Crashworthiness*, 9(5):449–463, 2004.
21. D. A. Huber. *The Use of Various Failure Criteria as Applied to High Speed Wear*. Wright Patterson Air Force Base, Dayton, 2011.
22. L. B. Wuertemberger. *Predicting the Wear of High Speed Rocket Sleds*. Wright Patterson Air Force Base, Dayton, 2012.
23. G. Paek-Spiel. *Analysis of Heat Partitioning During Sliding Contact at High Speed and Pressure AFIT-ENC-DS-M-02 (Ph.D. Dissertation)*. Wright Patterson Air Force Base, 2014.
24. K. H. Le. *A Study of the Thermal Environment Developed by a Traveling Slipper at High Velocity AFIT-ENY-13-M-20 (Master's Thesis)*. Wright Patterson Air Force Base, 2013.
25. C. J. Alban. *Thermal and Melt Wear Characterization of Materials in Sliding Contact at High Speed AFIT-ENY-14-M-04 (Master's Thesis)*. Wright Patterson Air Force Base, 2014.
26. G. Cavallaro. *A Study of Slipper and Wear Interaction at Low Speed AFIT-ENY-T-14-J-31 (Master's Thesis)*. Wright Patterson Air Force Base, 2014.
27. M. Meyers. *Dynamic Behavior of Materials*. New York: John Wiley and Sons, 1994.

28. R. LeSar. Introduction to computational materials science. Aug 2013. Available at <http://www.icmr.ucsb.edu/programs/summer-school-2013/LeSar%20UCSB%20Summer%20School.pdf>.
29. M. F. Ashby. Physical modelling of materials problems. *Materials Science and Technology*, 8(2):102111, 1992.
30. I. H. Shames and F. A. Cozzarelli. *Elastic and inelastic stress analysis*. Taylor and Francis, 1997.
31. J. W. Morris. Dislocation plasticity: an overview. *Encyclopedia of Materials Science and Technology*, 2001.
32. Crystal structures of austenite, ferrite and cementite, and the fe-c equilibrium phase diagram. World Wide Web Page. Available at http://cml.postech.ac.kr/2008/Steel_Microstructure/SM2.html.
33. Parr J. G. Hanson, A. *Engineering Properties of Steel*. Addison Wesley Publishing Company, Inc., United States of America, 1965.
34. Examples of lattice planes, 2014.
35. G. Krauss. *Steels*. ASM International, Materials Park, OH, 2005.
36. J. D. Campbell and W. G. Ferguson. The temperature and strain-rate dependence of the shear strength of mild steel. *Philosophical Magazine*, 21(169):63–82, 1970.
37. R. J. Clifton. Dynamic plasticity. *Journal of Applied Mechanics J. Appl. Mech.*, 50(4b):941, 1983.
38. M. A. Meyers and K. K. Chawla. *Mechanical Metallurgy: Principals and Applications*. Prentice Hall, 1984.
39. J. D. Eshelby. Proc. phys soc. *Proc. Phys Soc.*, A12:307, 1949.
40. P Ludwik. Uber den einfluss der deformationsgeschwindigkeit bie bleibenden deformationen mit besonderer beruecksichtigung der nachwirkungserscheinungen. *Phys. Zeit*, 10:41–417, 1909.
41. Y. Berstrom. The holloman n-value, and the strain to necking in steel. pages 1–10, 2011.
42. U. S. Lindholm. Some experiments with the split hopkinson pressure bar. *J. Mech. Phys. Sol.*, 12:317–335, 1964.
43. J. T. Hammer. *Plastic Deformation and Ductile Fracture of Ti-6Al-4V Under Various Loading Conditions (Master's Thesis)*. Columbus, 2012.

44. J. A. Zukas. *High Velocity Impact Dynamics*. John Wiley and Sons, New York, 1990.
45. G. R. Johnson and W. H. Cook. Fracture characteristics of three metals subjected to various strains, strain rates, temperatures, and pressures. *Engineering Fracture Mechanics*, 21(1):31–48, 1985.
46. W. Jong, I. Springer. *GC 2009-267: Teaching von mises stress: from principal axes to nonprincipal axes*.
47. J. W. Hancock and A. C. Mackenzie. On the mechanisms of ductile failure in high-strength steels subjected to multi-axial stress-states. *Journal of the Mechanics and Physics of Solids*, 24(23):147 – 160, 1976.
48. D. L. Zou, L. Zhen, Y. Zhu, C. Y. Xu, W. Z. Shao, and P. J. Pang. Deformed microstructure and mechanical properties of am60b magnesium alloy under hypervelocity impact at a velocity of 4km/s,. *Materials Science and Engineering A*, 527:3323–3328, 2010.
49. G. Dirras, H. Couque, J. Gubicza, A. Ourem, T. Chauveau, and P. Jenei. Fine-grained nickel deformed by direct impact at different velocities: Microstructure and mechanical properties. *Materials Science and Engineering A*, 527:4128–4135, 2010.
50. J. Gubiczaa, N. Chinha, J. Labaras, S. Dobatkinc, Z. Hegedusa, and T. Langdond. Correlation between microstructure and mechanical properties of severely deformed materials. *Journal of Alloys and Compounds*, 483:271–274, 2009.
51. K. Qin, L. Yang, and S. Hu. Mechanism of strain rate effect based on dislocation theory. *Chin. Phys. Lett.*, 26(3):036103–1–4, 2009.
52. H. Couque and R. Boulanger. Efp simulations with Johnson-Cook Models. In *23rd International Symposium on Ballistics, Tarragona*. 2007.
53. L. Wuertemberger and A. N. Palazotto. Evaluation of flow and failure properties of treated 4130 steel. *J. dynamic behavior mater. Journal of Dynamic Behavior of Materials*, 2(2):207222, 2016.
54. *ASM Material Data Sheet*. ASM Aerospace Specification Metals Inc., [Online], June 2014.
55. Astm e8 / e8m-15a, standard test methods for tension testing of metallic materials. World Wide Web Page. Available at www.astm.org.
56. Model 3442 miniature extensometers. Technical report, Air Force Institute of Technology, 2015. Available at <http://www.epsilontech.com/3442.htm>.

57. W. Chen and B. Song. *Split Hopkinson (Kolsky) bar: design, testing and applications*. Springer, Berlin, 2011.
58. T. Nicholas. Tensile testing of materials at high rates of strain. *Experimental Mechanics*, 21(5):177–185, may 1981.
59. Special metals inconel alloy 718.
60. N. Dowling. *Mechanical Behavior of Materials*. Pearson Prentice Hall, Upper Saddle River, New Jersey 07458, 2007.
61. M. Sasso, M. Costanzi, G. Newaz, and D. Amodio. Determining true stress-strain curve by dynamic tensile tests. In *SEM X International Conference and Exposition*.
62. P. W. Bridgman. *Studies in large plastic flow and fracture: with special emphasis on the effects of hydrostatic pressure*. McGraw, 1952.
63. G. E. Dieter, H. A. Kuhn, and S. L. Semiatin. *Handbook of Workability and Process Design*. ASM International, 2003.
64. X. Yang, L. G. Hactor, and J. Wang. A combined theoretical/experimental approach for reducing ringing artifacts in low dynamic testing with servo-hydraulic load frames. *Experimental Mechanics*, 2014.
65. X. Xiao. *Proceedings of the XIth International Congress and Exposition*. Society for Experimental Mechanics Inc., 2008.
66. M. Borsutzki, D. Cornette, Y. Kuriyama, A. Uenishi, B. Yang, and E. Opbroek. Recommendations for dynamic testing of sheet steels. Report, International Iron and Steel Institute, 2005.
67. P. W. Bridgman. Effects of high hydrostatic pressure on the plastic properties of metals. *Reviews of Modern Physics*, 17(1), 1945.
68. O. Hopperstad, T. Borvik, M. Langseth, K. Labibes, and C. Albertini.
69. T. Borvik, O. S. Hopperstad, and T. Berstad. On the influence of stress triaxiality and strain rate on the behavior of structural steel: Part ii. *European Journal of Mechanics A/Solids*, 22:15–32, 2003.
70. Hancock J.W. Brown D.K.e Mackenzie, A.C. On the influence of state of stress on ductile failure initiation in high strength steels. *Engineering Fracture Mechanics*, 9:167–188, 1977.
71. H. P. Gavin. The levenberg-marquardt method for nonlinear least squares curve-fitting problems. Article, Duke University, Oct 2013.

72. Dassault Systme. Abaqus analysis user's manual. 2011.
73. Abaqus v6.11.1 analysis user's manual documentation. Technical report, 2011.
74. J. K. Lee. Analysis of multi-layered materials under high velocity impact using cth afit/gae/eny/08-m19. Master's thesis, Air Force Institute of Technology, Wright-Patterson Air Force Base, Ohio, mar 2008.
75. C. Z. Duan, T. Dou, Y. J. Cai, and Y. Y. Li. Finite element simulation and experiment of chip formation process during high speed machining of aisi 1045 hardened steel. *International Journal of Recent Trends in Engineering*, 1(5):46–50, may 2009.
76. *Military Handbook - MIL-HDBK5H: Metallic Materials and Elements for Aerospace Vehicle Structures*. US Department of Defense, 1998.
77. EDAX TSL Solutions. Oim analysis 5.3 manual. Available at [http://www.material.ntnu.no/ebsd/ebsd/oim analysis 5_3 manual.pdf](http://www.material.ntnu.no/ebsd/ebsd/oim%20analysis%205_3%20manual.pdf). Accessed 1 June 2016.
78. EDAX. *OIM 5.3 Analysis*. TexSEM Labrotories, Inc, 1997.
79. Buehler. *Application Guide Polishing*. Illinois Tool Works, Inc, 2012.
80. V. Randle and O. Engler. *Introduction to texture analysis: macrotexture, microtexture and orientation mapping*. Gordon and Breach science publishers, 2000.
81. EBSD Oxford Instruments. Interpreting the diffraction pattern. Technical report, Oxford Instruments Plc, 2016. Available at <http://www.ebsd.com/ebsd-explained/basics-of-ebsd/interpreting-the-diffraction-pattern>.
82. O. Engler and V. Randle. *Introduction to texture analysis: macrotexture, microtexture and orientation mapping*. Taylor and Francis, 2nd edition, 2010.
83. A. Hald. *A history of mathematical statistics from 1750 to 1930*. Wiley, 1998.
84. wikieducator.org. Stats 11: Anova analysis of variance chapter 16. Available at http://wikieducator.org/images/f/fb/stats_11_anova.pdf, Dec 2009.
85. P. R. Earl. Ra fisher and statistics. Technical report, Universidad Autnoma de Nuevo Len, San Nicols, Dec 2015. Available at www.pitt.edu/~super7/28011-29001/28741.ppt.
86. D. C. Montgomery. *Design and analysis of experiments*. John Wiley & Sons, Inc., 2013.
87. A. Gelman. Analysis of variance - why it is more imporatnt than ever. *The Annals of Statistics*, 33(1):153, 2005.

88. Statistics and probability dictionary, 2016.
89. Minitab Inc. Minitab 17 software suite. 2016.
90. D. L. Jones. *Johnson Curve Toolbox for Matlab: analysis of non-normal data using the Johnson family of distributions*. University of South Florida, 2014.
91. R. S. Witte and J. S. Witte. *Statistics*. Harcourt Brace College Publishers, 1997.
92. F. M. J. Thijssen. Effect of strain on microstructural evolution during dynamic recrystallization: Experiments on tin. *Utrecht University*, Jan 2004.
93. B. Derby and M. F. Ashby. On dynamic recrystallization. *Scripta Metallurgica*, 21:879884, 1990.
94. G. Z. Voyiadjis and F. H. Abed. Microstructural Based Models for bcc and fcc Metals with Temperature and Strain Rate Dependency. *Mechanics of Materials*, 37:355–378, 2005.
95. Chang-Sik Oh, Nak-Hyun Kim, Yun-Jae Kim, Jong-Hyun Baek, Young-Pyo Kim, and Woo-Sik Kim. A finite element ductile failure simulation method using stress-modified fracture strain model. *Engineering Fracture Mechanics*, 78(1):124137, 2011.
96. T Borvik, O. S. Hopperstad, T. Berstad, S. Dey, and M. Langseth. *3th European LSDYNA User's Conference*, page 111. 2011.

REPORT DOCUMENTATION PAGE					Form Approved OMB No. 0704-0188	
<p>The public reporting burden for this collection of information is estimated to average 1 hour per response, including the time for reviewing instructions, searching existing data sources, gathering and maintaining the data needed, and completing and reviewing the collection of information. Send comments regarding this burden estimate or any other aspect of this collection of information, including suggestions for reducing this burden to Department of Defense, Washington Headquarters Services, Directorate for Information Operations and Reports (0704-0188), 1215 Jefferson Davis Highway, Suite 1204, Arlington, VA 22202-4302. Respondents should be aware that notwithstanding any other provision of law, no person shall be subject to any penalty for failing to comply with a collection of information if it does not display a currently valid OMB control number. PLEASE DO NOT RETURN YOUR FORM TO THE ABOVE ADDRESS.</p>						
1. REPORT DATE (DD-MM-YYYY)		2. REPORT TYPE		3. DATES COVERED (From — To)		
08-12-2016		Ph.D. Dissertation		Dec 2012 — Aug 2016		
4. TITLE AND SUBTITLE Evaluation and correlation of dynamic flow, failure, and microstructural properties of heat-treated 4130 steel				5a. CONTRACT NUMBER		
				5b. GRANT NUMBER		
				5c. PROGRAM ELEMENT NUMBER		
6. AUTHOR(S) Luke Atticus Wuertemberger				5d. PROJECT NUMBER		
				5e. TASK NUMBER		
				5f. WORK UNIT NUMBER		
7. PERFORMING ORGANIZATION NAME(S) AND ADDRESS(ES) Air Force Institute of Technology Graduate School of Engineering and Management (AFIT/EN) 2950 Hobson Way WPAFB OH 45433-7765				8. PERFORMING ORGANIZATION REPORT NUMBER AFIT-ENY-DS-16-S-068		
9. SPONSORING / MONITORING AGENCY NAME(S) AND ADDRESS(ES) Department of Engineering Aeronautical and Astronautical Engineering 2950 Hobson Way WPAFB OH 45433-7765 DSN 785-6184, COMM 937-255-3636 Email: luke.wuertemberger@afit.edu				10. SPONSOR/MONITOR'S ACRONYM(S) AFOSR		
				11. SPONSOR/MONITOR'S REPORT NUMBER(S)		
12. DISTRIBUTION / AVAILABILITY STATEMENT DISTRIBUTION STATEMENT A: APPROVED FOR PUBLIC RELEASE; DISTRIBUTION UNLIMITED.						
13. SUPPLEMENTARY NOTES						
14. ABSTRACT An experimental program has been carried out in conjunction with the University of Dayton Research Institute to characterize the material constants of the Johnson-Cook constitutive and damage models, and additionally, the microstructure of the failed specimen has been investigated to observe any association of deformation micromechanics to the phenomenological development of the Johnson-Cook expression. An Analysis of Variance (ANOVA) statistical analysis was carried out to identify whether temperature or strain rate were significant factors in causing changes to micromechanical features, and if so, whether the micromechanical properties were related to the Johnson-Cook parameters.						
15. SUBJECT TERMS Dynamic impact, constitutive modeling, damage criteria, Johnson-Cook						
16. SECURITY CLASSIFICATION OF:			17. LIMITATION OF ABSTRACT	18. NUMBER OF PAGES	19a. NAME OF RESPONSIBLE PERSON	
a. REPORT	b. ABSTRACT	c. THIS PAGE			Dr. Anthony Palazotto, AFIT/ENY	
U	U	U	U	209	19b. TELEPHONE NUMBER (include area code) (937) 255-3636, x4599; anthony.palazotto@afit.edu	